Wave-type Based Real-Time Prediction of Strong Ground Motion

Echtzeit-Wellenbasierte Modelle für die Vorhersage der Erdbebenbeschleunigung

Amin Zahedi Khameneh

Berichte des Instituts für Bauinformatik, Heft 10

Schriftenreihe des Instituts für Bauinformatik
Herausgeber: Univ.-Prof. Dr.-Ing. R. J. Scherer

© Institut für Bauinformatik,
Fakultät Bauingenieurwesen, TU Dresden, 2012

1. Auflage, Dezember 2012
ISBN: 978-3-86780-311-3

Institut für Bauinformatik, TU Dresden

Postanschrift
Technische Universität Dresden
01062 Dresden

Besucheranschrift
Nürnberger Str. 31a
2. OG, Raum Nr. 204
01187 Dresden

Tel.: +49 351/463-32966
Fax: +49 351/463-33975
E-Mail: Raimar.Scherer@tu-dresden.de
www: http://tu-dresden.de/biw/cib

Diese Arbeit wurde unter dem Titel

Wave-type based Real-Time Prediction of Strong Ground Motion

Echtzeit-Wellenbasierte Modelle für die Vorhersage der Erdbebenbeschleunigung

an der Fakultät Bauingenieurwesen der Technischen Universität Dresden als

DISSERTATION

von

Amin Zahedi Khameneh

geboren am 15. April 1978 im Iran

zur Erlangung des akademischen Grades eines Doktor-Ingenieurs (Dr.-Ing.) genehmigt.

Gutachter:

Prof. Dr.-Ing. Raimar J. Scherer, Technische Universität Dresden

Prof. Dr.-Ing. habil. Carsten Könke, Bauhaus-Universität Weimar

Tag der öffentlichen Verteidigung: 10. July 2012

Preface

This work was completed during my Ph.D. study and scientific research at the Institute of Construction Informatics, Technical University of Dresden, from April 2006 to October 2011.

Foremost, I would like to express my sincere gratitude to my advisor professor Raimar Scherer for the continuous support and his professional encouragement. His guidance helped me in all the time of research and writing of this thesis. Besides my advisor, I would like to thank my thesis reviewer professor Carsten Könke from Bauhaus-Universität Weimar and the thesis committee: professor Ivo Herle, professor Kai-Uwe Graw, professor Peer Haller and professor Bernd W. Zastrau for their encouragement and insightful comments.

Thanks also to my colleagues of the Institute of Construction Informatics for helping me during my study.

I wish to thank Dr. Mehdi Zare from International Institute of Earthquake Engineering & Seismology (IIEES) for his continuous guidance and kindly supports.

I am thankful to my family for their patient support during all these years. For their understanding, continuous support, and motivation during the last years, I would like to express my special sincere thanks to my father and my mother.

Dresden, December 2012

Amin Zahedi Khameneh

For Firoozeh

thank you for your accompany.

Abstract

Several wave type based methods for real-time prediction of strong ground motion (SGM) accelerogram are developed. Real-time prediction of SGM is requested in building control systems to trigger and control actuator systems achieving the goal of reduction of structural deformations. It is well known that SGM is a classic example of non-stationary stochastic process with temporal variation of both amplitude and frequency characteristics.

In the suggested real-time predictors the main non-stationarity of the SGM process is considered by splitting the process in its dominant seismic phases, namely P phase from the combined S and coda phase. Therefore, the prediction is performed according to a two-step approach. At the first step by the use of a real-time seismic phase detector, the dominant seismic wave phases are discriminated. In the second step, the wave-type based strong ground motion accelerogram is predicted for the each of the two seismic phases. In this thesis to perform the real-time prediction in each seismic phase two different model approaches are developed; the first is a group of Non-parametric soft-computing based prediction models and the other model is a stochastic parametric model. While the non-parametric soft-computing based model is built based on the training and learning paradigm in which the training dataset plays a very important role, the spectral modeling in the stochastic parametric model is performed only based on the measured data without any external learning memory.

The developed wave type based non-parametric models (NP) are built based on the non-homogeneity of the SGM process. Learning capability of Artificial Neural Networks is used to establish the real-time non-parametric prediction models. During the non-parametric modeling of SGM two distinguish approaches are followed; namely Phase-entire and Evolutionary prediction approaches.

The Phase-entire non-parametric model (NP1) is developed to perform the real-time prediction of the entire seismic phase; i.e. the early signals of the on-going seismic phase is used to predict the entire phase signals. Here by the use of the early signals collected of a wide number of SGM accelerograms two Neural Network predictors are trained; namely duration estimator and signal generator. The duration estimator is designed to estimate the length of the dominant seismic phase. To investigate the effectiveness of the networks four different neural networks structures are developed (Feedforward Backpropagation Neural Networks). It is expected that the non-parametric phase-entire model (NP1) can satisfy the non-homogeneity of the SGM process.

The evolutionary non-parametric model (NP2) is suggested to satisfy specially the non-stationary nature of the SGM process in real-time modeling. Through this modeling approach, prediction of seismic signal is performed by shifting a moving window segment by segment during the specified wave phase, which leads to predict the on-coming signals in time window $t+\tau$ based on the measured signal in time window t. Three different windowing approaches are deployed; namely constant windowing (NP2.1), semi-adaptive (NP2.2) and adaptive windowing (NP2.3). During constant windowing approach (NP2.1), length of the sampling windows remains constant during the seismic phases. In contrast, lengths of the sampling windows are adjusted based on

the frequency content of the signal in semi-adaptive (NP2.2) and adaptive windowing (NP2.3). Therefore one important part of the evolutionary non-parametric model is determining the length of the frequency-content based time-window. In evolutionary model (NP2) it is expected that the model can consider very well the non-homogeneity as well as non-stationarity of the SGM signal, especially by the use of frequency content corresponding windowing approaches.

In the stochastic parametric model (SP) the non-homogeneity of the SGM process is achieved similar to the developed non-parametric model by splitting the process in its dominant phases, i.e., P, S-Coda. Since separating of the temporal amplitude and spectral non-stationary characteristics of SGM process increases the flexibility and ease in modeling and parameters estimation, two distinguish models for amplitude envelope and spectral content of SGM are developed. In order to model the spectral amplification of several layers and modes of resonance, multi Kanai-Tajimi filter (multi-KTF) is applied, which is the extended KTF by superposing multiple KTF according to the number of observed resonances to multi-KTF. The temporal stochastic evolutionary process of amplitude is modeled by using the relevant wave type based envelope functions. Parameters of the real-time predictor model are identified and estimated by continuously matching the model to the target accelerograms. The parameters of the amplitude envelope function are estimated by using the rising envelope curve of the measured data. It is expected that the stochastic parametric model can model very well the amplitude envelope function in evolutionary manner (amplitude non-stationarity). In frequency domain, the developed model is able to extract the parameters of multiple resonances and model the frequency content of on-coming signal using the extracted values.

Kurzfassung

Zur Echtzeitvorhersage der Erdbebenbeschleunigung wurden mehrere wellenbasierte Modelle entwickelt. Die Echtzeitvorhersage ist beim Einsatz von Steuerungssystemen von Gebäuden erforderlich, um Aktuatoren zur aktiven Bauwerkssteuerung rechtzeitlich auslösen und ansteuern zu können. Es ist bekannt, dass Starkbodenbewegungen (Strong Ground Motion) bei Erdbebenereignissen ein klassisches Beispiel nicht-stationärer stochastischer Prozesse mit zeitlicher Variation der Amplitude und der Frequenz sind.

Bei dem entwickelten Echtzeitvorhersagemodell wird die Instationarität des Prozesses durch Dekomposition des Prozesses in seine dominanten Wellenphasen, nämlich P-Phase aus der kombinierten S und Coda-Phase erreicht. Deshalb wird die Vorhersage durch einem zweistufigen Ansatz durchgeführt. Im ersten Schritt durch den Einsatz eines Echtzeit-seismische Phasen-detektor, sind die dominierenden seismischen Wellen-Phasen unterschieden. Auf der zweiten Stufe wird die wellen-basierten Bodenbeschleunigung für die jeder der beiden seismischen Phasen vorhergesagt. Um die Echtzeitvorhersage der Erdbebenbeschleunigung durchzuführen, werden zwei unterschiedliche Modelle entwickelt: Eine Gruppe von nicht-parametrischen soft-computing basierten Vorhersagemodellen und ein stochastisches Modell. Während die nicht-parametrische Soft-Computing-Modell auf dem Training- und Lernen-Paradigma basiert, in dem die Trainings-Daten eine sehr wichtige Rolle spielt, wird die spektrale Modellierung in der stochastischen parametrischen Modell nur auf den gemessenen Daten ohne externe Lernens durchgeführt.

Die entwickelten Wellentyp-basierten nicht-parametrischen Modelle (NP Modelle), werden auf der Basis der Inhomogenität des SGM-Prozesses aufgebaut. Die Lernfähigkeit von Neuronalen Netzen wird verwendet, um die nicht-parametrischen Echtzeitvorhersage-Modelle abzubilden. Zur nicht-parametrischen Modellierung von SGM wurde zwei unterschiedliche Ansätze verfolgt, nämlich phasenübergreifende und evolutionäre Vorhersage.

Das phasenübergreifende nicht-parametrische Modell (NP1) wurde entwickelt, um die Echtzeit-Vorhersage der ganzen seismischen Phase durchzuführen, d.h. die Anfangssignale der laufenden seismischen Phase dienen dazu, den Beschleunigungszeitverlauf der gesamten Phase vorherzusagen. Durch die Nutzung der Anfangssignale einer großen Anzahl von SGM Zeitverläufen werden mittels zweier neuronaler Netze Prädiktoren trainiert: ein Schätzer der Dauer und der Signalerzeuger. Der Dauer-Schätzer ermöglicht es, die Länge der dominierenden seismischen Phase zu schätzen. Zur Untersuchung der Wirksamkeit des Modells werden vier verschiedene Strukturen von neuronalen Netzen entwickelt (Feed-Forward Backpropagation neuronale Netze). Es wird erwartet, dass das nicht-parametrische phasenübergreifende Modell (NP1) die Inhomogenität des SGM-Prozess abbilden kann.

Das evolutionäre nicht-parametrische Vorhersagemodell (NP2) wird vorgeschlagen, um speziell der nicht-stationären Eigenschaften des SGM-Prozesses in Echtzeit zu modellieren. Durch diese Modellierung wird die Vorhersage des seismischen Signals mittels Verschiebung eines beweglichen Fensters während der angegebenen Wellen-

Phase durchgeführt. Folglich wird das Signal im Zeitfenster $t+\tau$ auf das gemessene Signal in Zeitfenster t vorhergesagt. Hierzu werden drei verschiedene Fenstertechnik-Ansätze entwickelt, nämlich die konstante Fenstertechnik (NP2.1), die semi-adaptive (NP2.2) und die adaptive Fenstertechnik (NP2.3). Bei der konstanten Fenstertechnik (NP2.1), bleibt die Länge des Probenahme-Fensters während der gesamter seismischen Phasen konstant. Im Gegensatz dazu sind die Längen der Probenahme-Fenster bei der semi-adaptiven (NP2.2) und adaptiven Fenstertechnik (NP2.3) auf den Frequenzinhalt des Signals abgestimmt. Ein wichtiger Teil des evolutionären nicht-parametrischen Vorhersagemodells ist die Bestimmung der Länge der frequenzbezogenen Zeitfenster. Beim evolutionären Modell wird erwartet, dass die Inhomogenität sowie Nicht-Stationarität des SGM-Signals sehr gut, vor allem durch den Einsatz des frequenzbezogenen Fenstertechnik-Ansatzes erfasst wird.

Im stochastischen parametrischen Modell (SP Modell) wird die Inhomogenität des SGM-Prozesses ähnlich wie beim nicht-parametrischen Modell erfasst, indem der Prozess in seine dominanten Phasen (P, S-Coda) aufgeteilt wird. Die Trennung der zeitabhängigen Amplitude von den nicht-stationären spektralen Eigenschaften des Prozesses erhöht die Flexibilität und Leichtigkeit bei der Modellierung und Parameterschätzung. Um die spektrale Verstärkung aus mehreren Schichten bzw. den Normalmoden des Resonanz-Modells zu berücksichtigen, wird der Multi-Kanai-Tajimi Filter (Multi-KTF) angewendet, der durch die Überlagerung mehrerer KTF Abhängigkeit der Zahl der beobachteten Resonanzen erweitert wird. Der evolutionäre zeitliche stochastische Prozess der Amplitude wird entsprechend der seismischen Wellenphasen durch die wahlweise Verwendung einer Normalverteilung und einer exponentiellen Formfunktion, entsprechend des Vorschlags von Shinozuka und Sato modelliert. Die Parameter des Echtzeitvorhersagemodells werden durch eine kontinuierliche Anpassung des Echtzeitvorhersagemodells an den Ziel-Beschleunigungszeitverlauf bstimmt. Es wird erwartet, dass das stochastische parametrische Modell die Amplitudeneinhüllende in evolutionärer Weise (die Amplituden-Nicht-Stationarität) sehr gut modellieren kann. Im Frequenzbereich ist das entwickelte Modell in der Lage, die Parameter für mehrere Resonanzen zu extrahieren und anhand der extrahierten Werte der Frequenzinhalt des nachfolgenden Signals zu modellieren.

TABLE OF CONTENTS

LIST OF FIGURES ..... **XVI**
LIST OF TABLES ..... **XIX**
ABBREVIATIONS ..... **XX**
INTRODUCTION **1**
1.1 MOTIVATION 1
1.1.1. Building Active Control Systems 1
1.1.2. Time delay Effect in Active Control Systems 2
1.2 GOAL STATEMENT 4
1.3 HYPOTHESIS 5
1.4 THESIS OUTLINES 7
THE NON-STATIONARY STRONG GROUND MOTION **9**
2.1 STRONG GROUND MOTION PROCESS 10
2.1.1. Origination and Propagation of Seismic Waves 10
2.1.2. Local Site Effects 12
2.2 STRONG GROUND MOTION PARAMETERS 14
2.2.1. Strong Ground Motion Parameters in Time-Domain 14
2.2.2. Strong Ground Motion Parameters in Frequency-Domain 15
2.3 TIME-DEPENDENT ANALYSIS OF STRONG GROUND MOTION 16
2.3.1. Evolutionary Power Spectral Analysis 17
2.3.2. Time-Dependent Principal Correlation Axes Analysis 17
2.3.3. Time-Dependent Analysis of Bam 2003 Main Shock 18
2.4 CONCLUSIONS 25
SITE-DEPENDENT SIMULATION OF STRONG GROUND MOTION **27**
3.1 SIMULATION OF STRONG GROUND MOTION 28
3.2 STOCHASTIC SIMULATION OF STRONG GROUND MOTION 29
3.2.1. Stationary Stochastic Strong Ground Motion Simulation 30
3.2.2. Non-Stationary Stochastic Strong Ground Motion Simulation 31
3.2.3. Amplitude Envelope Functions 34
3.3 ARTIFICIAL NEURAL NETWORK BASED MODELS 37
3.3.1. Parametric ANNs Model of Strong Ground Motion 38
3.3.2. Non-Parametric ANNs Model of Strong Ground Motion 39
3.4 REAL-TIME PREDICTION OF STRONG GROUND MOTION 41
3.4.1. Time-Series based Prediction Model 41
3.4.2. Prediction Model based on Conditioned Fuzzy Classifier 42
3.4.3. Hybrid Prediction Model 45
3.5 CONCLUSIONS 46

SOFT-COMPUTING BASED REAL-TIME PREDICTION MODEL 47
4.1 ARTIFICIAL NEURAL NETWORKS 48
4.1.1. Components of Artificial Neural Networks Model 48
4.1.2. Learning Paradigms of Neural Networks 49
4.1.3. Application of Artificial Neural Networks in Engineering Seismology 51
4.2 NON-PARAMETRIC (NP) REAL-TIME MODELING OF STRONG GROUND MOTION 53
4.2.1. Pre-Processing of the Accelerogram Signal 54
4.3 PHASE-ENTIRE PREDICTION MODEL (NP1) 55
4.3.1. Phase-Duration Estimator 56
4.3.2. Signal Generator Artificial Neural Networks (S-ANNs) 57
4.4 EVOLUTIONARY PREDICTION MODEL (NP2) 58
4.4.1. Dominant Seismic Phase Detector (DSPD) 59
4.4.2. Dominant Frequency Estimator (DFE) 60
4.4.3. Wave type Relevant Signal Generator (WRSG) 62
4.5 CONCLUSIONS 64
STOCHASTIC REAL-TIME PREDICTION MODEL 65
5.1 STOCHASTIC REAL-TIME MODELING OF STRONG GROUND MOTION 66
5.1.1. Model Construction 67
5.1.2. Modeling of Frequency Content of Strong Ground Motion 69
5.1.3. Modeling of Amplitude Envelope of Strong Ground Motion 72
5.2 DEVELOPING THE REAL-TIME POWER SPECTRAL MODEL 75
5.2.1. Estimation of PSD parameters 76
5.2.2. Applying the PSD model 77
5.3 DEVELOPING REAL-TIME EVOLUTIONARY AMPLITUDE MODEL 78
5.3.1. Establishing of the Evolutionary Amplitude Envelope Model 78
5.3.2. Applying the Evolutionary Amplitude Envelope Model 80
5.3.3. Correction of the Energy Content 81
5.4 CONCLUTIONS 81
APPLICATION AND VERIFICATION OF THE REAL-TIME PREDICTION MODELS 83
6.1 APPLICATION OF the SOFT-COMPUTING BASED REAL-TIME MODEL 84
6.1.1. Database 84
6.1.2. Verification of the Entire-Phase Real-Time Prediction Model (NP1) 85
6.1.3. Verification of the Evolutionary Real-Time Prediction Model (NP2) 90
6.2 APPLICATION OF THE STOCHASTIC REAL-TIME MODEL 105
6.2.1. Database 105
6.2.2. Verification of the Stochastic Real-Time Prediction Model 105
SUMMARY AND OUTLOOKS 121

APPENDIX A **125**
APPENDIX B **133**
REFERENCES **141**

LIST OF FIGURES

Fig. 1. 1 The essential components of the building control system 2
Fig. 1. 2 Displacement and velocity feedback vectors in phase space 3
Fig. 1. 3 The major parts of the suggested wave-type based real-time 5

Fig. 2. 1 Schematic ground motion near the ground surface 11
Fig. 2. 2 Arrival times at a given distance from the epicenter for several 12
Fig. 2. 3 Scheme of local site-effects and the role of soil layer 13
Fig. 2. 4 Relationship between maximum acceleration on rock and soft soil 13
Fig. 2. 5 a) Satellite image of 2003 Bam Earthquake b) Aftershock locations 19
Fig. 2. 6 Acceleration components of the BAM 2003 main shock 20
Fig. 2. 7 Normalized logarithmic contour plots of the evolutionary spectra 22
Fig. 2. 8 Elevation and strike angles φ and θ of the principal axes T_1 23
Fig. 2. 9 Development of the strike angle θ in time intervals 24

Fig. 3. 1 Site-dependent simulation methods generally categorized in 30
Fig. 3. 2 Scaled recorded Fourier amplitude versus normalized frequency 33
Fig. 3. 3 Variation of standard deviation and zero-crossing with time and 34
Fig. 3. 4 Different envelope functions 35
Fig. 3. 5 Fitting the lognormal PDF/CDF envelope model to the observed 37
Fig. 3. 6 ANNs based parametric simulation model of SGM and spectra 38
Fig. 3. 7 Response spectrum compatible accelerogram simulator 39
Fig. 3. 8 Accelerogram generator Neural Network 40
Fig. 3. 9 Flow chart of fuzzy optimum control 43
Fig. 3. 10 Piecewise SGM model 43
Fig. 3. 11 Fuzzy rules for the prediction of the next earthquake motions 44
Fig. 3. 12 Linear interpolation method of conditioned fuzzy set rules 44

Fig. 4. 1 Artificial neural network model. 48
Fig. 4. 2 Schematic of the supervised learning approach. 49
Fig. 4. 3 Schematic of the unsupervised learning approach. 50
Fig. 4. 4 Training and validation error curves. 51
Fig. 4. 5 Phase-entire real-time SGM predictor. 55
Fig. 4. 6 Schematic of the Artificial Neural Networks based prediction model. 55
Fig. 4. 7 Logistic sigmoid Linear and transfer functions. 56
Fig. 4. 8 Structures of the duration-estimator models 57
Fig. 4. 9 Structure of the signal generator artificial neural networks 58
Fig. 4. 10 Evolutionary real-time SGM predictor 58
Fig. 4. 11 Components of the evolutionary real-time prediction model 59

Fig. 4. 12 Three orthogonal components of earthquake Northridge. 60
Fig. 4. 13 Adaptive windowing approach.....61
Fig. 4. 14 Gaussian radial basis transfer function. 63
Fig. 4. 15 The developed RBF neural network signal generator.....64

Fig. 5. 1 Schematic of the real-time stochastic prediction model 68
Fig. 5. 2 The effect of changing of the predominant frequency on KT-PSD for 70
Fig. 5. 3 The effect of changing of the damping ratio on KT-PSD for.....70
Fig. 5. 4 Multi Kanai-Tajimi Power Spectrum for three resonance modes 71
Fig. 5. 5 Simplified pattern of seismic acceleration in time and frequency 72
Fig. 5. 6 a) Amplitude envelope of P b) Amplitude envelope of S-Coda.....74
Fig. 5. 7 Gaussian envelope function for b=10 and various c.....74
Fig. 5. 8 Shinozuka-Sato envelope function for various b_1 and b_2.....75
Fig. 5. 9 Real-time power spectral model.....76
Fig. 5. 10 Distinction of the close resonance frequencies 77
Fig. 5. 11 Training process of the evolutionary envelope model 79
Fig. 5. 12 Fitting the envelope functions to the time-varying envelope 79
Fig. 5. 13 The architecture of amplitude evolutionary artificial neural networks 80
Fig. 5. 14 Applying the evolutionary amplitude envelope in real-time model. 81

Fig. 6. 1 Estimation of the length of the dominant P-wave phase for 15 86
Fig. 6. 2 Estimation of the length of the dominant P-wave phase for 5 testing.....86
Fig. 6. 3 Evaluating the performance of the S-ANNS for validation dataset. 87
Fig. 6. 4 Normalized cumulative Arias intensity of validation dataset.....87
Fig. 6. 5 Power spectra of the predicted and observed validation dataset 88
Fig. 6. 6 Evaluating the performance of the S-ANNS for test dataset.....88
Fig. 6. 7 Normalized cumulative Arias intensity of validation dataset.....89
Fig. 6. 8 Power spectra of the predicted and observed test dataset 89
Fig. 6. 9 Training epochs of the RBF neural network 90
Fig. 6. 10 Observed and predicted accelerogram for validation accelerogram 91
Fig. 6. 11 Observed and predicted response spectrum for validation.....91
Fig. 6. 12 Spectrograms of the Observed and predicted accelerogram.....92
Fig. 6. 13 Observed and predicted accelerogram for validation accelerogram 95
Fig. 6. 14 Observed and predicted response spectrum for validation.....96
Fig. 6. 15 Observed and predicted spectrogram for testing accelerogram 97
Fig. 6. 16 Observed and predicted accelerograms by applying the adaptive 101
Fig. 6. 17 Response spectra of observed and predicted accelerograms 102

Fig. 6. 18 Observed and predicted spectrogram for testing accelerogram 103
Fig. 6. 19 Evolutionary envelope function for dominant P wave 106
Fig. 6. 20 Evolutionary envelope function for dominant S-Coda wave 108
Fig. 6. 21 Observed strong ground motion accelerogram 111
Fig. 6. 22 Prediction #1 strong ground motion accelerogram 112
Fig. 6. 23 Prediction #2 strong ground motion accelerogram 113
Fig. 6. 24Prediction #3 strong ground motion accelerogram 113
Fig. 6. 25 Prediction #4 strong ground motion accelerogram 114
Fig. 6. 26 Prediction #4 strong ground motion accelerogram 115
Fig. 6. 27 Prediction #1 strong ground motion accelerogram 115
Fig. 6. 28 Prediction #2 strong ground motion accelerogram 116
Fig. 6. 29 Prediction #3 strong ground motion accelerogram 116
Fig. 6. 30 Prediction #4 strong ground motion accelerogram 117
Fig. 6. 31 Scaled cumulative Arias intensity of dominant P-wave 118
Fig. 6. 32 Scaled cumulative Arias intensity of dominant S-Coda wave.....119

LIST OF TABLES

Table 6. 1 Vs_{30} values for main site classes according to EC8 85
Table 6. 2 Average error value of the predicted accelerogram and.....93
Table 6. 3 Average error value of predicted accelerograms and 93

Table A. 1 Information about the using data set in Entire-Phase 125
Table A. 2 Information about the using database in non-parametric.....126
Table A. 3 Information about the using data set in Stochastic prediction 129

ABBREVIATIONS

AE-ANNs	Amplitude Envelope Artificial Neural Network
ANNs	Artificial Neural Networks
ARMA	Auto Regressive Moving Average
ARS	Acceleration Response Spectra
BHRC	Building and Housing Research Center
CAV	Cumulative Absolute Velocity
CDF	Cumulative Distribution Function
D-ANNs	Duration Estimator Artificial Neural Networks
DFE	Dominant Frequency Estimator
DSPD	Dominant Seismic Phase Detector
EPS	Evolutionary Power Spectrum
FAS	Fourier Amplitude Spectrum
FFBP	Feed-Forward Back-Propagation Neural Network
FFT	Fast Fourier Transformation
GPS	Global Positioning System
KTF	Kanai-Tajimi Filter
NEHRP	National Earthquake Hazards Reduction Program
NGA	New Generation Attenuation
NP	Non-Parametric Models
NP1	Phase-Entire Non-Parametric Model
NP2	Evolutionary Non-Parametric Models
NP2.1	Constant Evolutionary Non-Parametric Model
NP2.2	Semi-Adaptive Evolutionary Non-Parametric Model
NP2.3	Adaptive Evolutionary Non-Parametric Model
PCG	Preconditioned Conjugate Gradients
PDF	Probability Distribution Function
PGA	Peak Ground Acceleration
PGD	Peak Ground Displacement
PGV	Peak Ground Velocity
PSD	Power Spectral Density
PSHA	Probabilistic Seismic Hazard Analysis
RBNN	Radial Basis Neural Networks
S-ANNs	Signal Generator Artificial Neural Networks
SAPCA	Spectrally Adaptive Principal Correlation Axes
SGM	Strong Ground Motion
SP	Stochastic Parametric Model
TPCA	Time-Dependent Principal Correlation Axes
UBC	Uniform Building Code

Chapter 1
Introduction

1.1 MOTIVATION

This dissertation is motivated by a desire to develop the real-time Strong Ground Motion (SGM) prediction methods, which are requested in active and semi-active building control systems. Following, the functionality and essential components of the building active control systems are explained briefly and the desire to develop real-time SGM prediction methods in order to compensate the time delay effect are discussed.

1.1.1. Building Active Control Systems

Buildings have traditionally been built as passive structures with no adaptability to unknown dynamic loads. The concept of *active control* is defined as system that calculates and applies the controlling forces to modify the stiffness and the damping of structures in real-time for better safety and to reduce the damage. The basic task is to determine a control strategy that uses the measured structural responses or the SGM excitation or both of them to calculate an appropriate control signal to send to the actuator that will enhance structural safety and serviceability. Hence, the active control systems normally consist of the three basic elements:

- Sensors; which are applied to measure the external forces and structural response (according to the controlling approach the structural response can be measured or eliminated).
- Processing unit; which computes the control forces based on the measured external forces and/or structural response.
- Actuators; which provides the control forces.

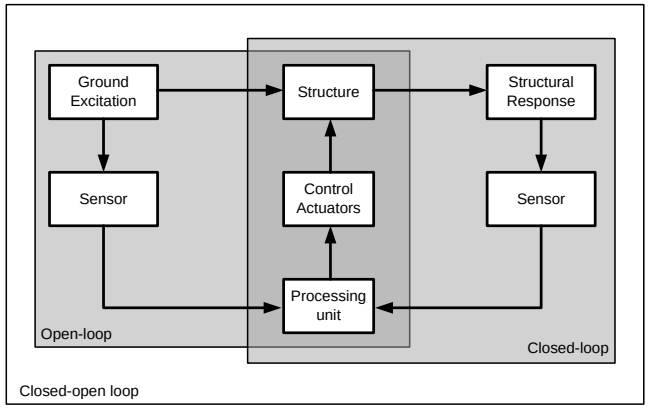

Fig. 1. 1 The essential components of the building control system and the three common open-loop, closed-loop and closed-open loop control algorithms.

Determination of the active control force is performed based on the minimization of a given performance index. Using different combinations of the response feedback such as velocity and displacement and acceleration several performance indexes have been defined (Chang and Yang ,1994; Joghataie and Mohebbi, 2008). As it is illustrated in Figure 1.1 the existing controlling algorithms can be classified into the closed-loop, open-loop and closed-open loop. In closed-loop control, active control force is regulated by the state vector, which is the response of the structure. On the contrary, if the computation of the active control force requires only the ground excitation information, then this control algorithm is considered as open-loop and if in the computation of the active control force both response of the structure and the ground excitation are used, then this control algorithm called closed-open loop.

In spite of the effectiveness of the control-systems to reduce the structural response, a number of problems are encountered in the practical implementation of the active control scheme. The most important real-time application problems can be listed as: modeling error, limited sensor and controller, parameter uncertainties and system identification, cost-effectiveness and hardware requirement and time delay (Datta, 2003). The effect of the time delay in vibration control is one of these problems that need serious attention. The time delay problem that is caused by the time lag between sensing the response and applying the control force will be discussed in the next section.

1.1.2. Time delay Effect in Active Control Systems

In treating ideal systems, it is assumed that the mentioned operations can be performed instantaneously. In reality, however, time has to be consumed in online data acquisition from the sensors at deferent locations of the system and filtering and processing of the measured information, and calculation of the control force and the transmission of the control force to the actuator. Thus, the time delay causes unsynchronized application of the control forces and this unsynchronization can not only render the control ineffective,

but may also cause instability in the system (Basharkhah and Yao, 1984; Pu, 1989). Consider the linear control law

$$F_c(t) = k_c x(t) + c_c \dot{x}(t) \tag{1.1}$$

Where k_c *and* c_c are respectively control stiffness and damping and x and $\dot{x}$ denote the displacement and velocity. Due to the time delay, the displacement feedback control and the velocity feedback control can be resolved into displacement and velocity components taking the phase delay into account as shown in Figure 1.2, where $\omega\tau_x$ and $\omega\tau_{\dot{x}}$ are the phase lags for displacement delay time τ_x and and velocity delay time $\tau_{\dot{x}}$, respectively, ω beeing the dominant system frequency

$$F_{c-delayed}(t) = \omega(k_c \tau_x(t) + c_c \tau_{\dot{x}}(t)) \tag{1.2}$$

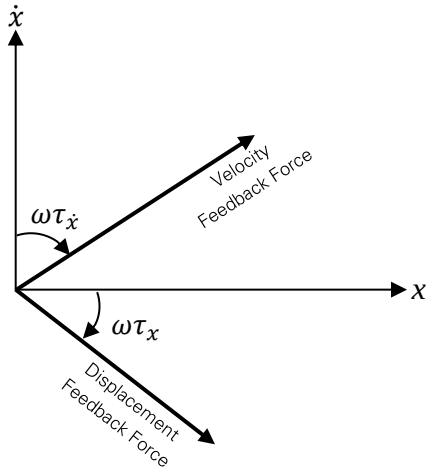

Fig. 1. 2 Displacement and velocity feedback vectors in phase space (Soong 1990).

In fact, the time delay will cause instability when the resultant damping force is negative. Since phase lag ($\omega\tau_x$ and $\omega\tau_{\dot{x}}$), are proportional to the delay time and dominant frequency, the effect of time delay might be serious for higher modes (higher frequencies) even with small amounts of time delay (Basharkhah and Yao, 1984; Soong, 1990; Yang *et al.*, 1990). The importance of time delay compensation in structural control has been studied by many researchers such as Chung *et al.*, 1988, 1995 and McGreevy *et al.*, 1988, and several compensation methods have been developed (Hammerstrom and Gros, 1980; Rodellar, 1987; Soliman and Roy, 1992). One of the most effective solutions is predictive control approach (Rodellar, 1987). This solution is very useful when the evolution of the external excitation can be precisely identified or predicted for a finite future interval Δt. Accordingly, to realize an optimum and adaptive control of structures subjected to earthquake loading, simulation of uncertain input waves is necessary. Existing methodologies to simulate the SGM excitation used in predictive active control systems can be categorized in the following sub-classes

- Pre-established earthquake spectrum compatible model
- Real-time time-series predictors

- Predictor Model based on conditioned Fuzzy classifier

The pre-established spectrum compatible model and the existing real-time SGM models are failed in many cases to establish a realistic real-time prediction of the on-going SGM. Mismatching of the prescribed spectral models and lack of the physical background of the process during the modeling, which caused by neglecting of the non-homogeneity and non-stationarity characteristics of the SGM process, are the most significant drawbacks of the existing simulation models. Therefore, that needs to establish real-time predictor models, which are able to satisfy efficiently the fundamental features of the SGM process.

1.2 GOAL STATEMENT

The goal of this dissertation is to provide a methodology to perform real-time prediction of the SGM in order to satisfy the following requirements

- Non-homogeneity, wave type based modeling; as SGM process is a non-homogenous process consisted of different wave types and different propagation features, to consider the non-homogeneity the prediction approach must be performed for every wave phase separately (P, S and Coda waves).
- Spectral non-stationarity; according to the non-stationarity of the SGM process in frequency domain, the developing real-time model must be able to reflect properly the variance of frequency content of the process during the time.
- Amplitude non-stationarity; to consider the amplitude non-stationarity the SGM simulation models apply the time-varying amplitude (variance) models which called envelope or modulating functions. The form of the envelope function is about arrived at through consideration of the manner in which energy is temporally distributed throughout an accelerogram.
- Local site-effects; ground resonance including several resonance modes/layers which appear in power spectrum as several peaks should be considered during the modeling process.
- Universality; it is necessary to develop the models, which can be applied in similar cases without any modification in the architecture of the models. In other words, by the use of several categorizations for several local conditions and using of the training databases which cover all the possible conditions, the efficiency of the model will be assured.
- Single record; the real-time predictor uses only the SGM accelerogram measured by a single accelerometer (three components), i.e. separation of the wave phases and generation of the predictor model and the prediction process.
- Independency from control equations; the real-time predictor is established independently from the control equations, which allows us to develop and use the real-time predictor for other application such as early warning systems, too.

1.3 HYPOTHESIS

Generally, the SGM prediction models belong to the *Site-based* models. The Site-based models do not require detailed seismological information from the seismic source and are therefore more readily applicable to regions where few instrumental recordings (either seismograms or accelerograms) have been measured. In this dissertation we are going to develop site-based prediction models which can fulfill the stated goal criteria based on the real-time recorded strong ground accelerogram.

The most fundamental criteria as it was mentioned in the previous section are the Non-homogeneity and Non-stationarity of SGM process. In order to consider the Non-homogeneity of the SGM process, development of the prediction models are performed for every dominant seismic phases separately. Accordingly, it is very important to detect the dominant seismic phase in real-time manner. To discriminate the seismic phases a method based on the Time-Dependent Principal Correlation Axes (TPCA) analysis (Scherer & Bretschneider 2000) has been applied. The other important criterion which should be necessarily fulfill in the real-time SGM model is the non-stationarity in both time and frequency domains. By developing the methods based on the evolutionary analysis of the SGM process the non-stationarity in both time and frequency domain can be reflected in the real-time models.

It is approved that there is a significant correlation between the first signals of SGM and its magnitude, duration and PGA (Scrivner and Helmberger 1995 and Allen 2006). Accordingly, in the current study real-time prediction models are developed to perform the prediction based on the real-time measured three orthogonal components of the SGM accelerogram. To refine the prediction results categorization of the modeling events based on the local site properties, epicentral distance, focal mechanism and moment magnitude is undertaken. As it is illustrated in Figure 1.3 the real-time prediction models extract the essential parameters or patterns from the measured signals to predict the oncoming signals. By defining the prediction parameters and patterns the dominancy and repeatability of them should be considered and above all they have to properly describe the physical characteristics of the process. To extract the dominant parameters and patterns it is necessary to apply some transformations or modifications or fitting approaches as it is discussed in the following chapters.

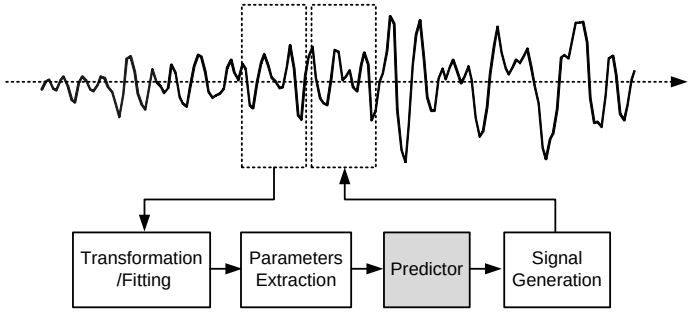

Fig. 1. 3 The major parts of the suggested wave-type based real-time SGM prediction models.

Next, the mechanisms which are able to perform the real-time prediction of the SGM process using the extracted parameters or patterns are established. In this thesis, several models are developed; the first is a group of Non-parametric soft-computing based prediction models and the other model is a stochastic parametric model.

The developed wave type based **non-parametric models (NP)** are built based on the non-homogeneity of the SGM process. Since the SGM process contains different wave types with the individual frequency domains and time-dependency amplitude shape pattern, an important part of the method is to detect dominant seismic wave phases. Learning capability of the Artificial Neural Networks is used to establish the real-time non-parametric prediction models. During the non-parametric modeling of SGM two distinguish approaches are followed; namely Phase-entire and Evolutionary prediction approaches.

The first non-parametric model (NP1) is developed to perform the real-time prediction of the seismic phase; i.e. the early signals of an on-going seismic phase is used to predict the entire phase signals. Here, by the use of the early signals collected of a wide number of SGM accelerograms two Neural Network predictors are trained; namely duration estimator and signal generator. The duration estimator is designed to estimate the length of the dominant seismic phase. To investigate the effectiveness of the networks four different neural networks structures are developed (Feedforward Backpropagation Neural Networks). On the other hand, the signal generator neural networks is trained to predict the SGM accelerogram in entire seismic phase. Using the Fast Fourier Transformation the input signals are divided into the real and imaginary parts of the Fourier Transform. The two parts of the transformed signal are applied to the neural networks as input vector and finally by the use of the Inverse Fourier Transformation the resulted output vector is transformed back to the acceleration vector. It is expected that the non-parametric phase-entire model (NP1) can satisfy the non-homogeneity of the SGM process. After the Fourier Transformation of the SGM signal, it is likely that NP1 can perform the prediction of the frequency content of seismic signal precisely.

The evolutionary non-parametric model (NP2) is suggested to satisfy specially the non-stationary nature of the SGM process in real-time modeling. Through this modeling approach, prediction of seismic signal is performed by shifting a moving window segment by segment during the specified wave phase, which leads to predict the on-coming signals in time window $t+\tau$ based on the measured signal in time window t. Three different windowing approaches are deployed; namely constant windowing (NP2.1), semi-adaptive (NP2.2) and adaptive windowing (NP2.3). During constant windowing approach (NP2.1), length of the sampling windows remains constant during the seismic phases. In contrast, lengths of the sampling windows are adjusted based on the frequency content of the signal in semi-adaptive (NP2.2) and adaptive windowing (NP2.3). Therefore, one important part of the NP2 model is determining the length of the time window based on the frequency content.

Basically, the evolutionary real-time predictor (NP2) is established based on the learning capability of Radial Basis Neural Networks (RBNN). Similar to NP1 model, the Fast Fourier Transformation is applied to emphasize and extract the most significant pattern and parameters from the acceleration signal. In evolutionary model (NP2) it is expected

that the model can consider very well the non-homogeneity as well as non-stationarity of the SGM signal, especially by the use of frequency content corresponding windowing approaches.

In the **stochastic parametric model (SP)** the non-homogeneity of the SGM process is achieved similar to the developed non-parametric model by splitting the process in its two dominant phases, i.e., P and S-Coda phases. Since separating of the temporal amplitude and spectral non-stationary characteristics of SGM process increases the flexibility and ease in modeling and parameters estimation, two distinguish models are for the amplitude envelope and one for the spectral content of SGM are developed. In order to model the spectral amplification of several layers and modes of resonance, multi Kanai-Tajimi filter (multi-KTF) is applied, which is the extended KTF by superposing multiple KTF according to the number of observed resonances to multi-KTF. The temporal stochastic evolutionary process of amplitude is modeled by using the relevant wave type based envelope functions. Parameters of the real-time predictor model are identified and estimated by continuously matching the model to the target accelerograms. Because of the temporal nature of the amplitude envelope function, non-deterministic pattern recognition methods are deployed to estimate the parameters of the amplitude envelope function. The suggested envelope functions are described through three parameters which are related to variables that directly present the physical properties of an accelerogram. The parameters of the amplitude envelope function are estimated by using the rising envelope curve of the measured data. It is expected that the stochastic parametric model (SP) can model very well the amplitude envelope function in evolutionary manner (amplitude non-stationarity). In frequency domain, the developed SP model is able to extract the parameters of multiple resonances and model the frequency content of on-coming signal using the extracted values.

1.4 THESIS OUTLINES

The following chapters outline the framework underlying the calculations on which the work in this thesis is based. Chapter 2 reviews the significant seismological parameters and transformations. In chapter 3 the state of the art of common SGM simulation methods are mentioned and discussed briefly. Chapter 4 and 5 focus on the methodologies, modeling approaches and the components of the developed models which are established in this study to perform real-time prediction of SGM. Finally, in chapter 6 the developed models are applied to perform real-time prediction of SGM and the obtained results are verified and discussed as well. In chapter 7 the contributions of the thesis are concluded and discussed.

The most distinguish seismic wave types and the corresponding features are discussed in chapter 2 briefly. Following, the important parameters and some basic transformations, which are applied in this thesis, are explained in this chapter. In addition, the Evolutionary Power Spectral analysis (EPS) and Time-Dependent Principal Correlation Axes Analysis (time-dependent PCA) as well as their application for the Bam earthquake, Iran (2003) are represented and the non-stationary characteristics and heterogeneity of the SGM signal are discussed.

Chapter 3 gives a short overview of the site-dependent SGM simulation methods. These methods are generally categorized into the stationary, filtered stationary, temporal non-stationary and non-stationary. The common stochastic simulation models and the frequently used amplitude envelope functions as well as the recent temporal formations are discussed in this chapter additionally. Beside the classic stochastic methods, the parametric and non-parametric Artificial Neural Networks based models are discussed. Finally, the state of the art of the real-time prediction models are represented and the methods based on the time-series and fuzzy classifiers are discussed as well.

Chapter 4 explains the proposed non-parametric soft-computing based real-time prediction model (NP). Since the non-parametric models in this chapter are established based on the learning capability of Artificial Neural Networks, the principles of Artificial Neural Networks are represented and the training process and several architecture of them are discussed briefly. Two general approaches which are followed in this study are discussed in this chapter subsequently; namely phase-entire (NP1) and evolutionary (NP2.1, NP2.2 and NP2.3) models. In the first approach the real-time prediction of the process is performed by the use of a phase-entire model (NP1) in which the early signals of an on-going seismic phase is applied to predict the entire phase signal. The other developed approach predicts the seismic signal by shifting a moving window point by point during the specified wave phase (NP2), which predicts the on-coming signal in time window $t+\tau$ based on the measured data in current time window t. Several windowing approaches which lead to three non-parametric models NP2.1, NP2.2 and NP2.3 are discussed.

In chapter 5 the real-time prediction of SGM signal by the use of the developed stochastic parametric model (SP) is represented. A real-time stochastic parametric model is developed in which the non-homogeneity of SGM process is achieved by splitting the process in its dominant phases, namely P and S-Coda phases. The components of the developed models both in the frequency- and the time-domains are elaborated in this chapter. Furthermore, the parameters of every models and how the model parameters affect the modeling process are discussed. In the following, estimation of every model parameters during real-time analysis and applying of the estimated parameters to every model in order to perform real-time prediction is discussed as well.

Chapter 6 represents the application of the developed real-time prediction models. The applying SGM databases are introduced in this chapter and the appropriate characteristics like magnitude, soil conditions and epicentral distance are expressed. The training process as well as the obtained results are discussed separately and the prediction models are verified.

Chapter 7 gives a summary of this thesis and the possible outlooks for further studies in real-time prediction are discussed.

Chapter 2
The Non-Stationary Strong Ground Motion

The recorded strong ground motion (SGM) signal is a function of time which reflects the characteristics of the waves caused during the rupturing process from the seismic source and the characteristics of the medium through which the waves are propagated to reach the bedrock, and finally the conditions of the local ground that amplify the signal. Accordingly the SGM record contains much information which can be interpreted by the use of several seismic quantities and transformations in both time and frequency domains. Reversely, based on the seismic quantities which characterize the SGM process, SGM can be generated artificially.

In this chapter essential features of the seismic waves and properties, which are applied in real-time prediction analysis, are discussed. At first, a short overview on origination and propagation of seismic waves as well as the definition of seismic wave types are given. The main seismic waves refer to those seismic waves which are significant from structural analysis point of view, i.e. those which are more destructive than the others. In addition, the important transformation and parameters which are used in the following chapters are explained. The non-stationary SGM signals are illustrated and discussed on the hand of the Bam 2003 earthquake analysed with the Evolutionary Power Spectral analysis (EPS) and the Time-Dependent Principal Correlation Axes Analysis (time-dependent PCA) method.

2.1 STRONG GROUND MOTION PROCESS

2.1.1. Origination and Propagation of Seismic Waves

For a long time it was assumed that earthquakes result from fractures, or faulting, of the earth's crust. The geological studies show that the seismic activities around the world are caused by moving tectonic plates. What are known as tectonic plates are several fairly rigid rock slabs placed on the outermost part of the earth (lithosphere). The basic concept embodied in plate tectonics was recognized several centuries ago by persons working with world maps that noted that the outline of the west coast of Africa is a good match for the east coast of South America and suggested that the two continents might at one time have been joined together. The geological structures of the earth show that numerous ruptures have occurred within the rock masses, most probably when they were strained beyond the deformational capacity of the type of material involved. When such ruptures occurred, relative sliding motions were developed between the opposite sides of the rupture surface creating what is called a geological fault. The important fact about any fault rupture is that the fracture occurs when the deformations and stresses in the rock reach the breaking strength of the material. Accordingly, it is associated with a sudden release of strain energy which then is transmitted through the earth in the form of vibratory elastic waves radiating outward in all directions from the rupture point.

The released energy travels through and around the earth as three basic types of elastic waves which make up the shaking that is felt and recorded. Of the three, only two propagate within the body of solid rock which are called body waves. The faster one of the body waves is the primary or *P wave*, in which the material particles move along the path of the wave propagation inducing an alternation between tension and compression deformations (see Figure 2.1 left side up). These P waves, just like sound waves, are able to travel through both solid rock, such as granite mountains, and liquid material, such as volcanic magma and the water of the oceans.

The second and slower body wave is called the secondary or *S wave*. As an S wave propagates, it shears the rocks sideways at right angles to the direction of travel (see Figure 2.1 right side up). Thus, at the ground surface S waves can produce both vertical and horizontal motions. The S waves cannot propagate in the liquid parts of the Earth, such as the oceans and their amplitude are significantly reduced in liquefied soil. It should be noted that S waves travel through the rocks and soils of the Earth with a rotational component. Torsional components of ground motion are thought to have important effects on the response of certain types of structures. Some building codes now contain material on practices that take rotational ground motion into consideration.

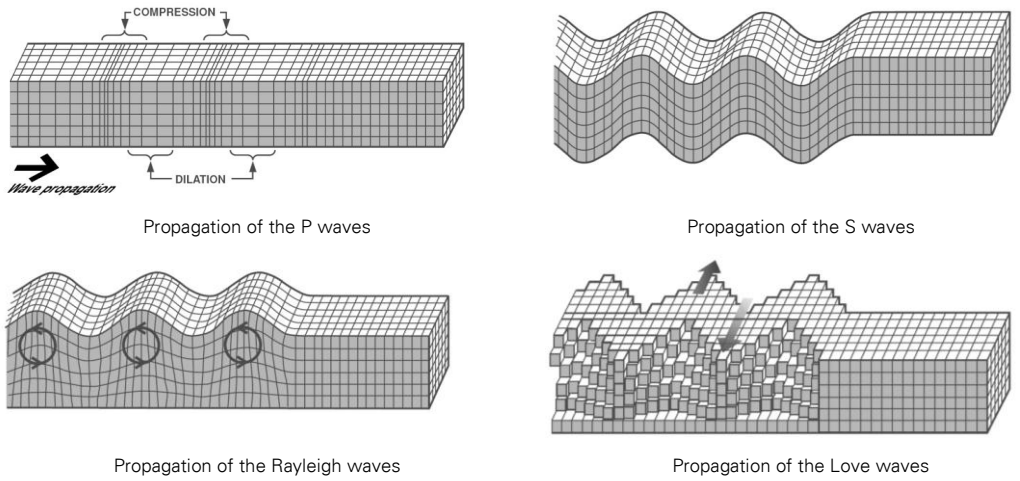

Fig. 2. 1 Schematic ground motion near the ground surface due to different body and surface waves (adopted from Bolt 1976).

The propagation velocity of P and S waves depends on the density and elastic properties of the rocks and soil through which they pass. This S wave motion is most effective in damaging structures. The speed of P and S waves are given in terms of the density of the elastic material and the elastic moduli

$$V_P = \sqrt{\frac{k+\frac{4\mu}{3}}{\rho}} \tag{2.1}$$

Where k is the modulus of incompressibility (bulk modulus) and μ is the modulus of rigidity and ρ is the density of the medium. Accordingly for S waves the propagation velocity is

$$V_S = \sqrt{\frac{\mu}{\rho}} \tag{2.2}$$

In fact, we know that K, μ, and ρ are not constant and change due to changing temperatures, pressures and compositions of material. For most consolidated rock,

$$V_P = \sqrt{3}\, V_S \tag{2.3}$$

Thus there is typically a one-second separation between the *P* and *S* waves for every 8 km traveled (Figure 2.2).

The third type of seismic wave is called *surface wave* because it travels along the surface of the earth. Surface waves in seismology can be divided into two types. The first is called a *Rayleigh wave*. Like rolling ocean waves, the pieces of rock disturbed by a Rayleigh wave move both vertically and horizontally in a vertical plane pointed in the direction in which the waves are travelling.

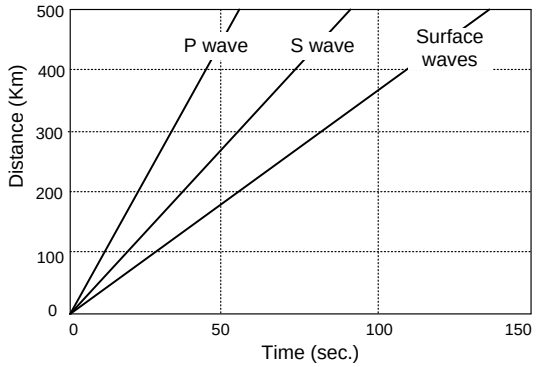

Fig. 2. 2 Arrival times at a given distance from the epicenter for several wave types.

The Rayleigh waves are tension-compression waves similar to the P waves except that their amplitude diminishes with distance below the surface of the ground. As shown by the arrows in Figure 2.1 left side down. Each piece of rock moves in an ellipse as the wave passes. The second type of surface wave is known as a *Love wave*. Its motion is similar to the S waves that have no vertical displacement; it moves the ground side to side in a horizontal plane parallel to the Earth's surface, but at right angles to the direction of propagation, as can be seen from the illustration in Figure 2.1 right side down.

Surface waves travel more slowly than body waves and of the two surface waves, Love waves generally travel faster than Rayleigh waves (Figure 2.2). Thus, as the waves radiate outwards from the earthquake source into the rocks of the Earth's crust, the different types of waves separate out from one another in a predictable pattern. Near a fault that is suddenly rupturing, the strong ground shaking in the associated earthquake consists of a mixture of various kinds of seismic waves that have not separated very distinctly. This complication makes identification of P, S and surface waves on strong motion records obtained near to the rupturing fault particularly difficult.

2.1.2. Local Site Effects

Site effects play a fundamental role in the observed ground motion, which are totally independent of the wave propagation medium, and are therefore usually separately treated from path effects. Site effects are mainly caused by shallow sediments of a few tens to hundreds of meters thickness, surface topology, and basins (Figure 2.3). The ground motion caused by the earthquake at bedrock level can be extremely modified in frequency contents as well as amplitude as it reaches the ground surface (Hwang *et al.* 1989 and Seed *et al.* 1987).

The most dominant site effect is modification of the amplitude of incoming seismic waves near the ground surface. Bouckovalas and Kouretzis (2001) have reported amplification about 40% for the horizontal component of Athens 1999 earthquake on the very stiff soils of the Athens basin, compared to the nearby outcropping soft rocks and almost 46% amplification of the response spectrum which has shifted elastic response spectra to higher periods. One of the reasons is the reflection of the P and S waves into

the crust when they reach surface of ground. So that the surface is affected almost simultaneously by upward and downward moving waves. Another reason for modification of the seismic wave near the ground surface is the effect of layers. When the elastic moduli have a mismatch from one layer to another, the layers act as wave filters amplifying the waves at some frequencies and deamplifying them at others. Resonance effects at certain frequencies occur.

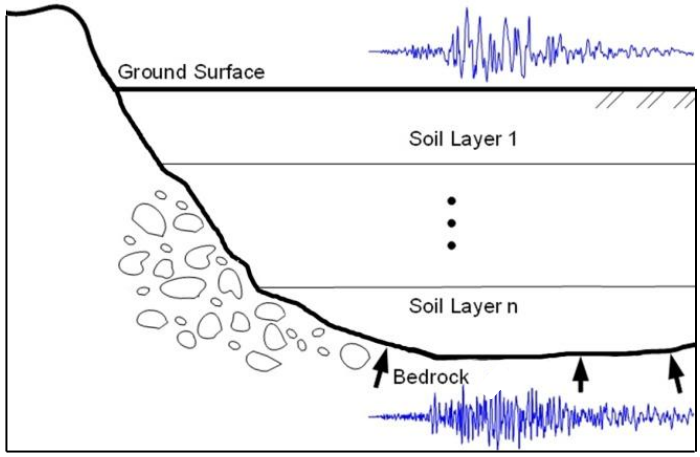

Fig. 2. 3 Scheme of local site-effects and the role of soil layer in filtering of motion signal.

Seismic waves of all types are progressively damped as they travel because of the non-elastic properties of rock and soil. One useful seismological quantity to measure damping is the parameter Q (for P and S waves in sediments, Q is about 500 and 200, respectively) such that the amplitude A at a distance d of a wave frequency f (Hz) and velocity V is given by

$$A = A_0\, e^{-(\pi f d/QV)} \tag{2.4}$$

The above physical description is approximate and while it has been verified closely for waves recorded by seismographs at a considerable distance from the wave source (the far-field), it is not adequate to explain important details of the heavy shaking near the center of a large earthquake (the near-field).

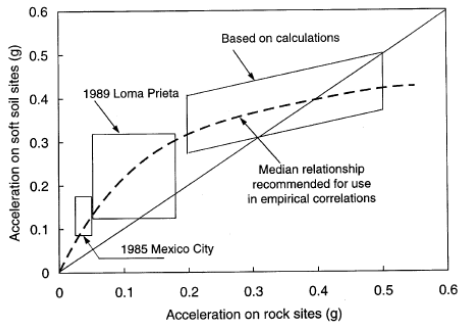

Fig. 2. 4 Relationship between maximum acceleration on rock and soft soil sites (adopted from Idriss 1990).

The amplification factor on acceleration response spectra strongly depends on the frequency of ground motion. Soft soil sites generally show higher amplification than rock sites by a factor of 2-3 for periods longer than about 0.2 seconds (frequency about 5.0 Hz). The independency of peak ground acceleration of the recording site situation (whether it is on rock or soil) was again confirmed for the near- and middle-field (epicentral distance shorter than 50 km) records of the Loma Prieta earthquake of 1989 (Boore *et al.*, 1989). For epicentral distances greater than about 50 km, however, peak acceleration was strongly influenced by surface geology; acceleration being lowest on rock sites, intermediate on alluvium sites and highest on artificial fill and bay mud. Idriss (1990) has drawn an exponential relationship between the acceleration on rock and soft soil sites by the use of Mexico City 1985, Loma Prieta 1989 and calculations (Figure 2.4).

2.2 STRONG GROUND MOTION PARAMETERS

Strong ground motion (SGM) which is sensed above the ground is a train of several seismic waves which reach the ground surface consecutive based on the wave type and distance from the seismic source. The seismic sensor measures the ground motion and translates it into a voltage. Ground motion can mathematically be described as displacement, velocity or acceleration. Since the measurement is done in a moving reference frame (the sensor is moving with the ground), the principle of inertia dictates that only motions that cause acceleration (change in velocity) can be measured. Thus, the principle of all sensors is that a mass must move relative to the reference in response to ground acceleration. Using broadband seismometers the motion over a wide range (or band) of frequencies and usually over a large range of amplitudes (the dynamic range) can be measured. Broadband sensors respond to most frequencies from 0.01 Hz to 50 Hz. For regional seismology, the frequency range of interest is from 0.05 to 20 Hz therefore; broadband sensors are most useful for recording regional earthquakes and teleseismic events.

This section gives an overview on commonly used ground motion parameters. The ground motion parameters characterize shaking by earthquakes either in the time or in the frequency domain; they favorably show a high correlation with damage by earthquakes which depends aside from mechanical characteristics and conditions of structures on amplitudes, duration and frequency content of ground shaking.

2.2.1. Strong Ground Motion Parameters in Time-Domain

There are several features and parameters which can be extracted and estimated from the SGM time-series. The most commonly used ground motion parameters in time domain are the peak values of acceleration *a*, velocity *v*, and displacement *u* denoted by PGA, PGV and PGD. Peak values give the largest absolute amplitudes of the respective time-series

$$PGA \equiv max\{|a|\} = max\{|\ddot{u}|\} \tag{2.5}$$

$$PGV \equiv max\{|v|\} = max\{|\dot{u}|\} \tag{2.6}$$

$$PGD \equiv max\{|u|\} \tag{2.7}$$

Typically, large peak values indicate destructive ground motions. If peak values, however, last only for a very short period of time, damage too many types of structures may be little. Peak values therefore should be combined with information on duration of ground motion. One of the most common measures of duration is the bracketed duration (Bolt, 1969), which is the time interval between the first and last exceedance of specified thresholds of ground shaking.

To consider the effect of duration which in combination with amplitude represents the energy content of the SGM, the cumulative intensity parameters are used. Integrative ground motion parameters, such as Arias intensity I_a (Arias, 1970) and the Cumulative Absolute Velocity (CAV), have the advantage that they do not only depend on single amplitudes but on the frequency content and/or duration of shaking. The Arias intensity I_a is the most frequent used intensity parameter which is calculated by the integrated squared acceleration *a(t)* of seismic ground motion over the time

$$I_a = \frac{\pi}{2g}\int_0^t a(t)^2\,dt \tag{2.8}$$

Where *g* is the acceleration of gravity. The Arias intensity quantifies the energy in the accelerogram in units of [m/s]. The CAV is defined by the integrated absolute value of acceleration over the time is the other significant duration based parameter which is defined as (EPRI, 1998)

$$CAV = \int_0^t |a(t)|\,dt \tag{2.9}$$

Based on the study of about 250 observed earthquakes of intensities between I and X Benjamin and Associates (1988) found that spectral accelerations and the cumulative absolute velocity are the two (out of ten) most reliable ground motion parameters to predict damage. Peak ground acceleration (PGA), on the other hand, has come off the worst.

2.2.2. Strong Ground Motion Parameters in Frequency-Domain

Frequency content of seismic ground motion is usually quantified through spectrum, such as the Fourier amplitude spectrum (FAS) or response spectrum commonly used in earthquake engineering. The Fourier transformation allows us to transform signals between the time and frequency domain, which makes it possible to choose either of them for a particular operation on the data. A brief overview of the theory will therefore be given. For a more complete overview, see e.g. Oppenheim *et al.* (1998). The seismic signal *x* is defined as a function of time t as *x(t)*. The complex Fourier spectrum *X(ω)* is then given as

$$X(\omega) = \int_{-\infty}^{+\infty} x(t)e^{-i\omega t}\,dt \tag{2.10}$$

Where $\omega = 2\pi f$. Note that the unit of spectral amplitudes is amplitude times second or amplitude/Hz and consequently it is called the amplitude density spectrum. Since the energy has been distributed over an infinite number of cycles with different frequencies, it is not possible to talk about the amplitude at a particular frequency, but rather about

the energy per cycle with unit of frequency. Similarly, we can define the power density spectrum *P(ω)* as

$$P(\omega) = |X(\omega)|^2 \tag{2.11}$$

The power spectrum is real and an expression for the power in the signal.

The other frequently used spectral parameter is the response spectrum. Response spectra describe the peak motion response of a single-degree of freedom elastic structure with a specified level of viscous damping towards a base acceleration *a(t)* that in case of earthquakes corresponds to seismic ground motion at the point of observation. The equation of motion of a simple harmonic oscillator is given by a second order, linear, inhomogeneous differential equation

$$\ddot{x} + 2\zeta\omega\dot{x} + \omega^2 x = -a(t) \tag{2.12}$$

Whereby ζ is the fraction of critical damping and ω is the natural frequency of the elastic structure. The desired response spectra are obtained from the maximum values of displacement, velocity and acceleration for a given excitation at each frequency ω

$$S_d(\omega, \zeta) \equiv max\{|x(\omega, \zeta)|\} \tag{2.13}$$

$$S_v(\omega, \zeta) \equiv max\{|\dot{x}(\omega, \zeta)|\} \tag{2.14}$$

$$S_a(\omega, \zeta) \equiv max\{|\ddot{x}(\omega, \zeta)|\} \tag{2.15}$$

Where S_d, S_v and S_a are the spectral values of displacement, velocity, and acceleration, respectively, given damping ζ and natural frequency ω.

2.3 TIME-DEPENDENT ANALYSIS OF STRONG GROUND MOTION

The SGM process is widely investigated by the parameters which are essentially capable to describe stationary processes, as peak values, power and Fourier or response spectra. In fact, the SGM is a non-stationary phenomenon, whose characteristics are strongly linked to a theoretically well understood, but practically poorly apprehensible physical background. Non-stationary analysis can reveal both dominant frequencies and certain temporal patterns in the seismic records, which are related to specific characteristics of the wave trains comprising the overall strong motion at the site and to general mechanics of an earthquake source. The patterns in turn allow us to identify the wave types of each wave train and to estimate seismological as well as engineering parameters. While non-stationary analysis has been focused onto mid-range strong motion records and has been used mostly to asses empirically parameters for seismic load models so far, it can also be applied to investigate strong motion records from the epicentral area of an earthquake in order to reconstruct the rupture process.

Based on these principles, Scherer (1993) has proposed a general non-stationary load modeling approach, consisting of a division of the ground motion process into sub-processes associated with major, load dominant wave trains, and based on the evolutionary spectrum both for the seismic load model itself and for the separation of the

sub-processes. Bretschneider & Scherer (2000a, 2000b, 2004 and 2006) have later suggested time-dependent principal correlation axes (TPCA) as the tool of choice to identify and distinguish the wave trains, and also a preliminary parametric load model for the transient sub-processes, based on the evolutionary spectrum of the first TPCA component.

In this section, the non-stationary properties of local SGM by means of Evolutionary Power Spectra (EPS) as well as by the Time-dependent Principal Correlation Axes (TPCA), similar to well-known Principal Component Analysis, were investigated. The time-dependent analyses were applied to the case study earthquake Bam. The catastrophic 2003 Bam, Iran, Earthquake has been analyzed by other researchers from seismological and engineering aspects, but frequency related parameters as well as non-stationary characteristics of this event have not been investigated so far. We have used these methods to identify major wave phases and estimate the directions of motion as well as other specific characteristics of the corresponding wave trains. The findings for the strong motion record at Bam are then discussed with respect to source dynamics.

2.3.1. Evolutionary Power Spectral Analysis

A common non-stationary strong ground motion model which incorporates both spectral characteristics and time dependence is the evolutionary power spectrum (EPS), theoretically introduced by Priestley (1965) as

$$S(f,t)df = E\{[A(t,f)dZ(f)]^2\} \tag{2.16}$$

Where *E{.}* denotes the expectation value and *A(t, f)* is the amplitude modulating function and *dZ(f)* is the differential of the orthogonal random process. In essence, the evolutionary spectrum describes energy (variance) distribution over the frequency and time domain of an ensemble of stochastic processes. Aim is to estimate the EPS directly from the accelerograms. Using the multi-filter technique the estimation is performed where a damped oscillator (single-degree-of freedom system) is used as the filter element. This method was changed by Scherer, Riera & Schueller (1982) to improve both the time and the frequency resolution of the EPS. Firstly, inverting the time leakage of the filter, e.g. the transient effect, in an approximate way; and secondly, using a constant half-power bandwidth have performed. The latter improvement has the consequence that the damping value frequency becomes dependent instead of being a fixed value.

Generally, evolutionary spectral analysis of strong motion accelerograms seems to be a difficult task, as these spectra usually do not have a smooth surface. However, important information about wave trains and their spectral characteristics can be derived from normalized power spectra.

2.3.2. Time-Dependent Principal Correlation Axes Analysis

Principal Correlation Axes were originally suggested by Penzien & Watabe (1975) for predictive load models as axes, where cross-correlation between the components of the 2D or 3D stationary stochastic process vanishes and hence these components could be treated independently in a statistical sense. A 3D stochastic process upon those axes is

completely described by three (auto-) covariances instead of six covariances of the symmetric Tensor in the general case. The idea has been picked up by Kubo & Penzien (1979) who described the properties of strong motion upon those axes. Bond (1980) was the first to apply TPCA to estimate those axes. His method has been improved by Scherer & Bretschneider (2000, 2004) and used for a comprehensive analysis of the 1994 Northridge Earthquake. Bretschneider (2006) has recently significantly improved and extended the estimator to all three principal axes, now called Spectrally Adaptive Principal Correlation Axes (SAPCA).

In short, the TPCA method can be described as an orthogonal, i.e. energy conserving, transformation $\mu^* = T^T \mu T$ of the coordinate system μ (e.g., μ = 0°, 90°, vertical axes) of the recorded data in a way which enables to inspect more clearly the dominant and sub-dominant oscillations of the strong motion. This means, the data itself, which can only be recorded as overlaid projections of the spatial oscillations upon unavoidably fixed axes of the recording device, remain unchanged, just the view onto the data is changed. It turns out that for an n-D stochastic stationary process, the transformation matrix T which fits best to this goal consists of the Eigenvectors (T_1, T_2, T_3) of the correlation matrix μ of its components. As strong ground motion is a process which is not stationary as a whole, all quantities in question are time-dependent with respect to limited stationary time intervals. After the transformation $A^* = T^T A$ of the data $A = (a_0; a_{90}; a_V)$, cross-correlation of the new acceleration components $A^* = (T_1; T_2; T_3)$ becomes zero, and the Eigenvalues λ of the diagonal matrix μ^*, which are indeed the variances of the components of A^*, exhibit a clear distribution to a maximal, intermediate and minimal value. The component T_1 corresponding to λ_{max} characterizes the direction of the energetically dominant acceleration oscillation in the time window where μ has been estimated. While TPCA works with fixed windows, the SAPCA method first applies a local spectral estimate to determine appropriate window length, which is crucial for optimal resolution without losing statistical significance.

As elaborated in Scherer & Bretschneider (2000), the course of the main principal axis T_1 reveals significant patterns, which can be analyzed by T_1's strike angle θ and elevation angle φ, defined similar to strike and rake of the slip vector in source mechanics. In a moderate distance to the rupture, high elevation indicates P-waves or Rayleigh waves, while low elevation corresponds to S waves and Love waves. Steep ascent or descent of elevation indicates a change of dominance from P to S waves and vice versa. The peaks of principal variance σ_1 within those P/S dominance intervals are useful to assess the intensity as well as the actual extension of the respective wave trains. Indeed, the principal variances are identical to the RMS functions of the principal axis components. θ is an indicator of the direction of transverse motion, most significant if elevation φ is low.

2.3.3. Time-Dependent Analysis of Bam 2003 Main Shock

During this section, application of the time-dependent analyses in processing of Bam 2003 earthqauek is represented. It is noteworthy that this section is provides based on the paper of Scherer, Zahedi Khameneh and Bretschneider (2008). The M_w 6.6 Bam earthquake occurred at 01:56:52 UTC on December 26, 2003 close to the town of Bam near Kerman in South-eastern Iran. The tectonics of the Bam region is dominated by the

convergence between the Arabian and Eurasian plates, trending N to NNE at velocity ranges from 25-35mm/yr as deduced from GPS measurements (e.g., McClusky *et al.*, 2003) and according to the NUVEL-1 model (DeMets *et al.*, 1990). To the west, the northwest-trending Zagros fold and thrust belt, which is an active continental collision zone, accommodates about 10mm/yr of NNE-trending shortening (Talebian and Jackson, 2002).

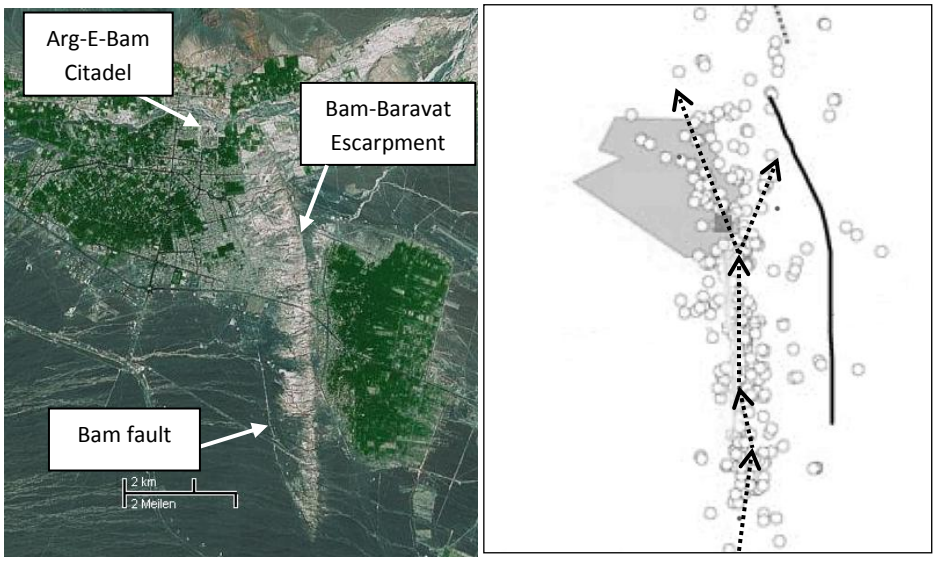

a) b)

Fig. 2. 5 a) Satellite image of the epicentral region of 2003 Bam Earthquake (© Google Maps). b) Aftershock locations and surface projection of the Arg-e-Bam fault proposed by Nakamura *et al.*.

The most obvious fault in the area is the escarpment running for ~12 km south from the Posht River, between Bam and Baravat. It is clearly visible in satellite imagery (Figure 2.5 a) and in the field, and is mentioned in several earlier publications on the area (e.g. Walker & Jackson 2002). Source mechanism solutions (Eshghi & Zaré, 2003; USGS, 2003) show that the earthquake was induced by strike-slip faulting 7 km south of Bam, at around 7 km depth. All studies agree that the bulk (>80%) of the moment was released by almost vertical, nearly pure strike-slip faulting beneath the surface ruptures observed south of Bam, with the main slip occurring over a distance of about 12 km running from the southern limit of the surface ruptures. In the supplementary on-line material of their initial report, Talebian *et al*. (2004) pointed out that the long-period P and SH waveforms of the main shock could not be explained by a single centroid source with a strike-slip mechanism.

Ground motion produced by the Bam earthquake was recorded in the centre of Bam city by a digital accelerometer operated by the Building and Housing Research Centre of Iran (http://www.bhrc.gov.ir/) (Figure 2.6). PGA of 0.98 g and 0.887 g were recorded in the

vertical and horizontal components at the site, which has been categorized by Zaré & Hamzehloo (2005) in UBC soil class 3 (average shear wave velocity in the first 30 meters 300 to 500 m/sec) due to the site fundamental frequency, which was found to be in the range of 2-5Hz.

A seismic network consisting of nine temporary stations had been installed to monitor aftershock activities in and around Bam from February 6 until March 7, 2004. Each station was equipped with a high sensitivity, velocity type, and three-component seismometer with a natural frequency of 1.0 Hz. A three-component strong motion accelerometer was also installed at the famous Arg-e-Bam citadel. The overall trend of the aftershock epicenter distribution is virtually linear along an approximately 20 km long axis in the N2°W–S2°E direction, parallel to a line about 3.5 km west of the geological Bam surface fault on the ground. Nakamura *et al*. (2005) propose a new "Arg-e-Bam fault" as the source fault to distinguish it from the Bam fault (Figure 2.5 b).

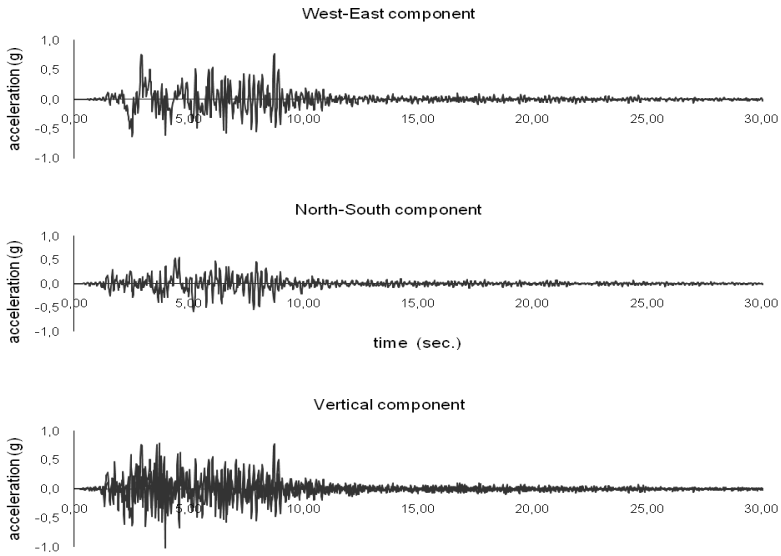

Fig. 2. 6 Acceleration components of the BAM 2003 main shock recorded at Bam station, first 30 seconds.

The Evolutionary Power Spectrum (EPS) of the vertical component (Figure 2.7) shows that the onset of the P-waves can be observed at around 1.2 sec in a broad frequency range. Furthermore, at least two pronounced peaks can be identified at 3.8 sec and 6.6 sec, most significant at frequencies of 9 Hz and 8.4 Hz, respectively. These peaks correspond to waves with vertical axis of motion; they may be interpreted as corresponding to new P-waves from a 2nd and 3rd rupture or from strong reflectors in the ground.

In the EPS of the horizontal components, onset of the first S-wave can be observed at the long peak beginning at 1.6 sec at a very low frequency of about 0.5 Hz, which clearly corresponds to the strong E-W pulse obvious in the accelerogram. A second strong peak occurs at (6.3 s, 7 Hz) in the E-W, but the strongest peak at 8 sec with a dominant

frequency of 4.5 Hz in both components. These peaks correspond to waves with predominant horizontal motion, i.e. S waves or Love surface waves. Again, it is possible to interpret this as indicating a second and third rupture segment producing S-waves of higher frequencies.

The right side of Figure 2.7 presents the EPS of the first time-dependent principal component T_1 determined by the TPCA method with a constant window length of 1.5 sec and 20% window overlap, which resides on a time-variable principal axis aligned with the course of the dominant direction of acceleration.

For the data of the Bam earthquake shown in Figure 2.2, strike and elevation of time-dependent principal correlation axes as well as principal variances have been estimated by the TPCA method for various window lengths. To investigate local non-stationary features in detail, we demonstrate them for a window length of 0.5 seconds with a window overlap of 20% in Figure 2.8. For proper interpretation of these graphs, one should understand that principal axes always form an orthogonal tripod; that each principal axis is associated with different wave trains over the course of the record or vice versa, that every wave train in the record is mapped onto different principal axes in a well defined manner, caused by its transient character and its relative rank in terms of energy. This is best observed at the principal variancesσ. It is essential to investigate angles and variances together and to take into account the cumulative effect of overlaid waves with resembling directions of motion, as well as geometrical attenuation and directivity effects.

In Figure 2.8, it can be seen from the σ diagram that the thick, thin and dotted curves refer to the principal axis with maximum, medium and minimum variance. Elevation φ_1 has three "hills", starting at 0.0 sec, until 7.2 sec, indicating dominance of P waves, and quite low φ_1 phases from 2.7-2.9 sec, 4.9-6.3 sec and 7.2-11sec, indicating dominance of waves with mostly transverse motion. The steep descents/ascents of φ_1 (and φ_2) mark the transition of dominance. Principal variance σ_1 has several pronounced peaks, each of which belongs to a transient wave train. The first peaks clearly belong to direct P waves, as elevation φ_1 is high. Peak at 2.6 sec belongs to direct S waves (see the SH pulse in Figure 2.8), its slope starts in σ_2 at about 2 sec, subdominant to earlier P waves, and is set forth in σ_2 at 3 sec. Likewise, the ascending and descending slopes of σ_1-peak at 3.7 sec are clearly visible in σ_2 from 2.5-3 sec and 4.2-4.8 sec. What follows are again two strongly dominant shear wave trains (φ_1 low) with σ_1-peaks at 7.8 and 8.8 sec.

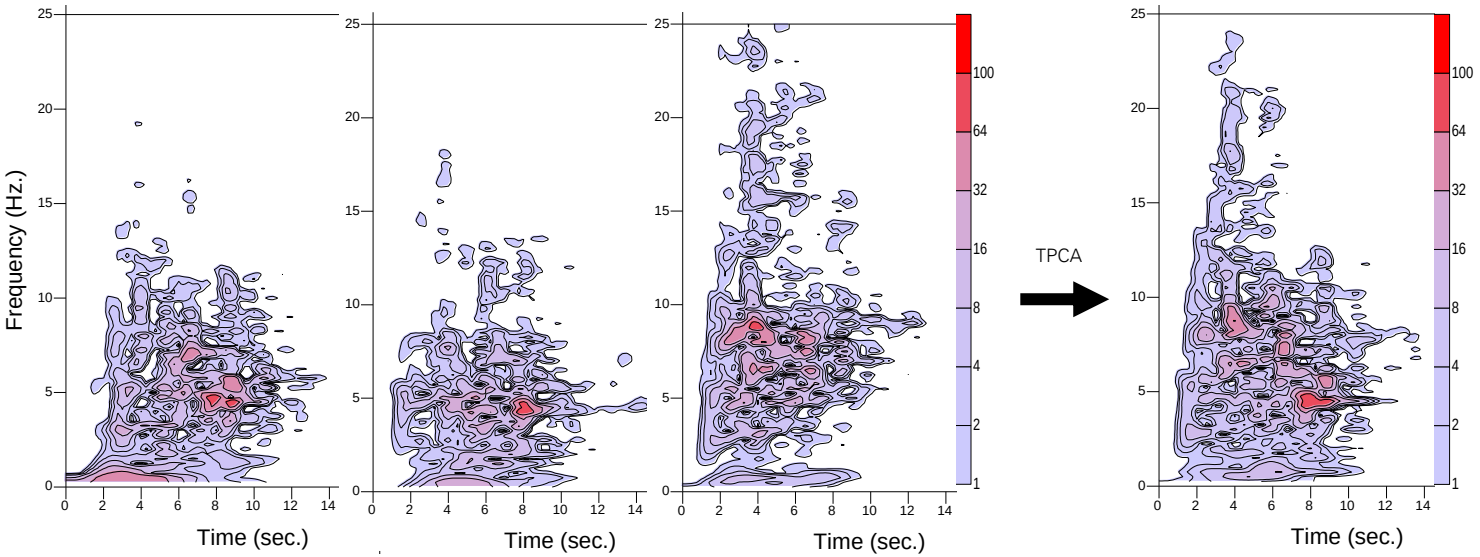

Fig. 2. 7 Normalized logarithmic contour plots of the evolutionary power spectra of the East-West, North-South & Vertical components and of the main principal axis component T_1 (right) of Bam record from Figure 2.6.

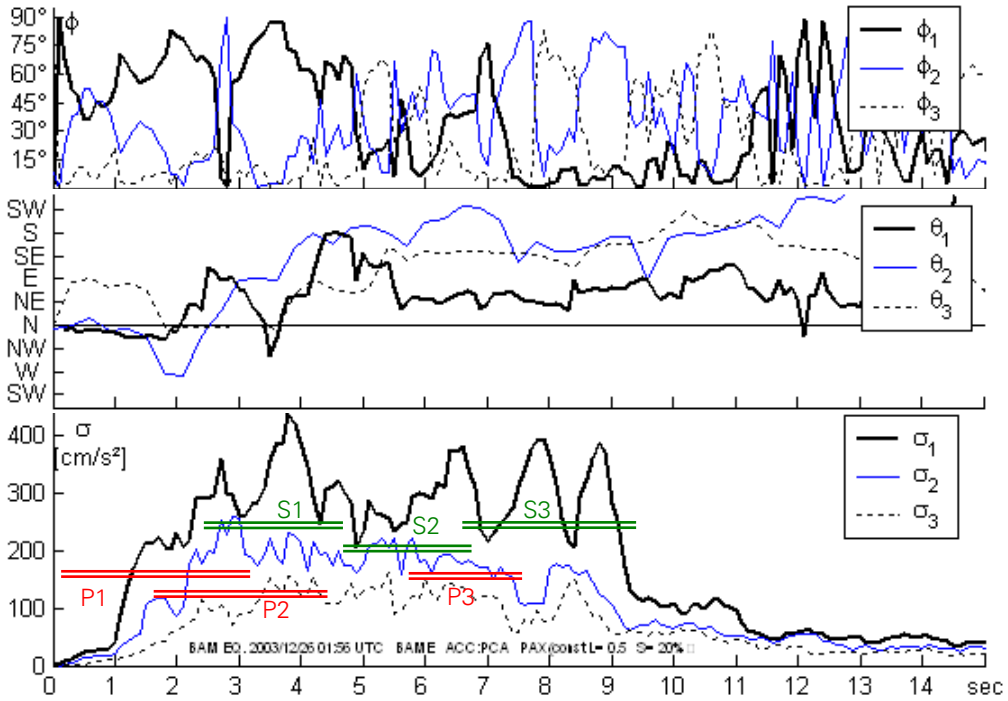

Fig. 2. 8 Elevation and strike angles φ and θ of the principal axes T_1 and the corresponding principal variances $\sigma_i = \sqrt{\lambda_i}$ for the Bam record in Figure 2.6, estimated by the TPCA method with a window length of 0.5 sec.

These three pairs of P-S phases, outlined in Figure 2.8 as P_1/S_1, P_2/S_2, P_3/S_3, do not belong to a single-phase source, but can be interpreted as stemming from three separate rupture phases. Inspecting strike angles θ (displayed in cardinal points) shall now reveal the orientation of the rupture segments. For S_1, θ_1 = east at 2.7s is continued sub-dominantly by θ_2 until 3.5 sec. For the ascending slope of S_1 at 2 sec, θ_2 = west is equivalent to E. As θ for S waves indicates the transverse axis of particle motion, we conclude that orientation of the first rupture segment is N-S. However, it is not safe to interpret θ_1 for P_2, between 3.0 and 4.9 sec, as the principal axis T_1 of the P_2 P waves is almost vertical, hence its minor projection into the horizontal plane maybe subject to noise and secondary effects. Nevertheless we can trust θ in the second phase S_2 of shear waves, and find that at the dominance transition point between its two peaks, marked by a dash-dot line, θ_1 switches from SE to almost NE. Taking into account that both P_2 and S_2 have two peaks in similar relation to each other, we conclude that the second rupture phase has two segments and that the rupture divided into two branches, one propagating NW (transverse to SE), towards the site, and another running NE, away from the site, hence its P and S waves arrive 1 sec later.

In the third phase of dominant P waves, from 6.2 to 7.2 sec, there is an interesting transition, apparently between two different P waves. Both φ_1, φ_2 initially show intermediate elevation, i.e. inclined incidence, and at 6.8 sec (dotted line), there is an immediate uprise of φ_1 to 90°, accompanied by a shift in strike θ_1. Typical for a

dominance transition was a changing intensity trend (a notch in σ), but σ_1 reveals that these shifts of the principal axis T_1 clearly occur in the midst of the slope of the σ_1-peak, i.e. within one and the same wave train.

Our interpretation of this is that a non-vertical (45°) strike-slip rupture has been passing by the site in very close distance, rising up the principal axis by P waves directly from beneath the site at the moment of crossing, which are immediately subdued by fellow S waves, but we can see them in. An explanation for the intensity of the S waves in the third phase, which are as strong as those of S_1, is that the generating rupture is now much closer to the site than the initial, more distant rupture phase; hence, the waves are only slightly attenuated. There are two distinguished peaks, whose strike θ_1 is stable NE with a sharp shift of 25° towards ENE at the transition point, which may again point to an asperity on the fault which caused the rupture to deviate. As θ shows the transverse of propagation, the third rupture segment points from SE to NE.

Note that there is another vertical motion in σ_2 which remains subdominant and whose corresponding high elevation ($\varphi_3|\varphi_2$ before/after the transition) continues as a plateau in $\varphi_2|\varphi_3$ and, from 11 sec, even in φ_1. It could be that these long enduring, combined horizontal and vertical motions are Rayleigh and/or Love waves generated e.g. by the surfacing rupture or at the Bam fault system. Our findings are in excellent agreement with results obtained by Nakamura (2005) from aftershock distributions. Figure 2.9 shows the strike angles σ_1 plotted into a map of the rupture zone, presentation is divided into four intervals for better readability. The solid line is the fault line identified by Nakamura, strike is drawn dashed at Bam site.

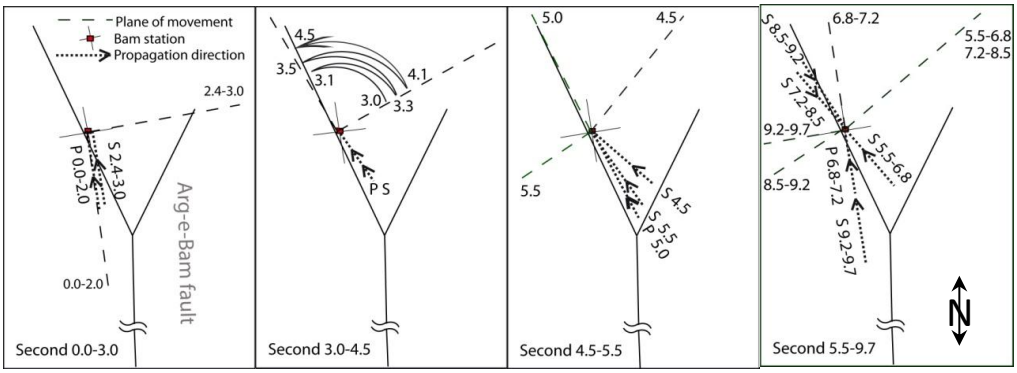

Fig. 2. 9 Development of the strike angle θ in time intervals (dashed lines, values in sec).

2.4 CONCLUSIONS

The most distinguish seismic waves and the corresponding features were discussed in this chapter. Namely, it was discussed; How the seismic waves are originated, how they are propagated through the earth and how the local site can affect the receiving waves. The amplification factor on acceleration response spectra strongly depends on the frequency of ground motion. Soft soil sites generally show higher amplification than rock sites for periods longer than about 0.2 seconds. The most important and frequently used parameters in both time and frequency domains that are developed to quantify the SGM process were reviewed as well in the following sections. The parameters like peak ground values and Arias intensity in time domain and Fourier amplitude spectrum and response spectrum in frequency domain.

The final part of the chapter has discussed the time-dependent analysis of SGM which leads to extract the non-stationary features of the process. The time-dependent analysis were explained during the analysis of the case study of Bam earthquake, Iran 2003. It turns out that the assembly of wave trains at the local site can be correctly decoupled and both the transient wave trains and significant parameters can be derived from patterns in the course of the time-dependent principal axes as well as the principal variances obtained by the TPCA method. Corresponding fundamental frequencies can be obtained from the evolutionary spectrum. The conclusions from the non-stationary TPCA analysis of the Bam record for the rupture movement earthquake Bam are in excellent agreement with results obtained from other methods accepted by seismologists, especially the fault lines obtained by Nakamura *et al.* (2005) from their analysis of aftershock distributions. The analysis does not validate the suitability of the TPCA method for analysis of rupture processes in general, as only one strong motion record was available. However, given more records from the rupture zone, it should be possible to reconstruct reliably the major fault lines, which is one of the targets of further research on application of TPCA in SGM analysis.

Chapter 3
Site-Dependent Simulation of Strong Ground Motion

Due to the complexity of the Strong Ground Motion (SGM) process, the site-dependent simulation models which do not require detailed seismological information and are therefore more readily applicable to regions where very few instrumental recordings have been made have a wide range of use. Consequently, several site-dependent SGM simulation approaches have been developed in the last 50 years.

This chapter provides a short overview of the common simulation methods. These methods are generally categorized into four groups: stationary, filtered stationary, temporal non-stationary and non-stationary. The frequently used amplitude envelope function as well as a recently developed temporal formation are discussed briefly. Beside the classic stochastic methods the soft computing based models especially the Artificial Neural Networks based simulation models, are presented in this chapter as well.

The final section of the chapter discusses the state of the art of the real-time prediction models. Evolutionary simulation of the SGM process during the occurrence is called real-time prediction. Since the real-time prediction of the SGM is mostly requested in building control systems to control the actuators force, the reaction time is limited to fractions of a second. The methods of time-series, fuzzy based and hybrid prediction are discussed in the section, too.

3.1 SIMULATION OF STRONG GROUND MOTION

For earthquake resistant design of critical structures, a dynamic analysis, either response spectrum or time history is frequently required. The major drawback of the response spectrum analysis in seismic design of structures lies in its inability to provide temporal information of the structural responses. Such information is sometimes necessary in achieving a satisfactory design. With increasing computing power and the advent of performance-based earthquake engineering different building codes, require in certain cases a dynamic analysis such as in the case of existence of irregular features in building floor cross section, non-uniform spatial distribution of mass or stiffness over the height of the buildings. Time-history dynamic analysis is more often employed by structural engineers, in recent years especially when nonlinear behavior is expected. In addition, in the design of critical facilities or major structures such as nuclear power plants, dams, or even high-rise buildings, the final design is usually based on a complete linear or nonlinear time-history analysis. Furthermore, reliable synthetic Strong Ground Motion (SGM) records are essential for seismic hazard and risk assessment and management purposes.

It is very unlikely, however, that recorded ground motions will be available for all sites and conditions of interest. To overcome this difficulty, many engineers select recorded motions from locations other than the project site and modify them by scaling or spectrum matching (Bommer & Acevedo, 2004; Hancock *et al.,* 2006; Watson-Lamprey, 2007), which are controversial methods (Naeim & Lew, 1995; Luco & Bazzurro, 2007) and may result in motions with unrealistic characteristics. It has long been established that due to parameters such as geological conditions of the site, distance from the source, fault mechanism, etc. different earthquake records show different characteristics. Hence, there is a great deal to develop efficient and accurate methods for the simulation of SGM that utilizes ground motions from previous events and recorded motions from the earthquake that has just occurred. The simulated SGM records must have realistic duration, frequency content, and intensity, representing the physical conditions of the site.

The scope of SGM accelerogram simulation models is broad by the real-time SGM simulation approaches. This so called real-time prediction models are applied in building predictive control systems. Since performing of the accurate real-time estimation of seismic source parameters is rather impossible, it is preferred to develope site-dependent real-time SGM prediction models. In the next paragraphs, the source- and site-dependent approaches in simulating of SGM will be discussed briefly. Generally, an earthquake is characterized in terms of the source, path, and site. Accordingly there are two types of SGM simulation models: models that describe the random occurrence of fault ruptures at the source and propagation of the resulting seismic waves through the ground medium (*source-dependent* models, see Zerva1988, for a review), and models that describe the ground motion for a specific site by fitting to a recorded motion with known earthquake and site characteristics ('site-dependent' models). Douglas & Aochi (2008) have described the source-dependent models as physically-based seismological models and site-dependent models as parameterized stochastic models fitted to

recorded ground motions. The methods which combine elements from both seismological and stochastic models are called hybrid models.

Source dependent models are conceptually attractive as they allow physical parameters obtained from seismological studies to be directly incorporated into the simulation process (Zerva, 1988; Quek *et al.,* 1990) and they can produce realistic accelerograms at low frequencies (<1Hz), but often need to be adjusted for high frequencies by combining with a stochastic or empirical component (hybrid model). These models require a thorough knowledge of the source, wave path, and site characteristics, which may not be available to the practicing engineer. Furthermore, as pointed out by Stafford *et al.,* (2009) and Chouet *et al.,* (1978), these models depend on physical parameters that vary significantly from region to region, thus limiting their use in regions where seismological data are lacking.

Site-dependent models on the other hand do not require detailed seismological information and are therefore more readily applicable to regions where very few instrumental recordings have been made. One disadvantage of this approach however is that specific characteristics of particular seismological scenario cannot always be accounted for the commonly adopted power spectral density function proposed by Kanai (1957) and Tajimi (1960) has a shape that is only dependent upon properties of the site but not of the source.

3.2 STOCHASTIC SIMULATION OF STRONG GROUND MOTION

Several site-dependent models have been developed in the last decades. Due to the complexity of the nature of the formation of seismic waves, so that they are initiated by irregular slipping along faults followed by several random reflections, refractions, and attenuations within the complex ground formations through which they pass, a stochastic approach may be most suitable solution to model the strong ground motion (SGM) process. In this regard, different stochastic models, both stationary and non-stationary have extensively been used in the literature to simulate earthquake ground motions (Figure 3.1). All these models assume the ground motion to be a zero-mean Gaussian process. An extensive review can be found in the studies of Liu (1970), Ahmadi (1979), Shinozuka & Deodatis (1988), Kozin (1988) and Conte & Peng (1997).

According to the advances in computing devices and reducing of the processing-cost in the recent years soft-computing based models have became very popular in different parts engineering seismology. These methods apply the learning concept during training process to produce specified outputs based on the specified input data. In this section, the most frequent using methods in simulation SGM will be discussed (Katayama, 1982; Ghaboussi & Lin, 1998; Lee & Han, 2002).

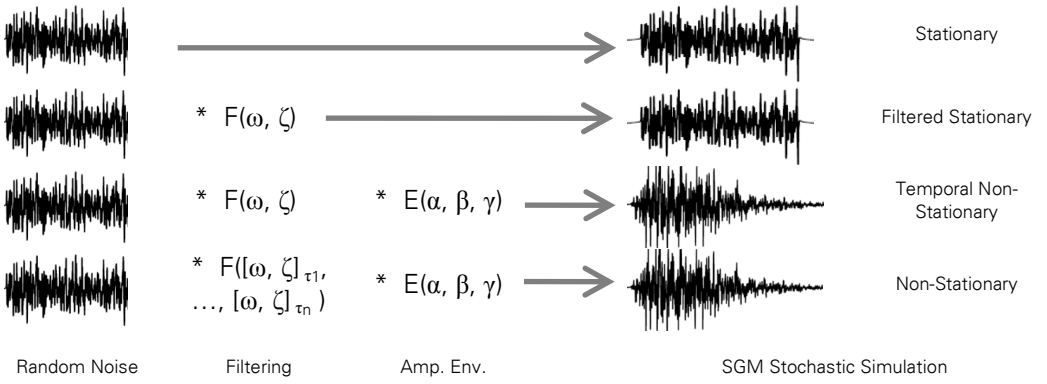

Fig. 3. 1 Site-dependent simulation methods generally categorized in four groups of stationary, filtered stationary, temporal non-stationary and non-stationary.

3.2.1. Stationary Stochastic Strong Ground Motion Simulation

The earliest attempts in stochastic modeling of earthquake ground motion were based on the interpretation of earthquake ground acceleration as a filtered white noise process or as a filtered Poisson process. More recently, models based on the spectral representation of stochastic processes, and auto-regressive moving average processes, have become more popular.

Stochastic models for characterization and simulation of earthquake ground motions have been of interest for a long time. Early efforts at such modeling were entirely based on stationary processes (e.g., Housner, 1947; Thomson, 1959; Kanai, 1957; Bycroft , 1960; Tajimi, 1960; Rosenblueth & Bustamante, 1962; Housner & Jennings, 1964; Housner, 1995). In view of the irregularity of the faulting process, SGM at some distance from the fault might be considered as the superposition of short-duration random pulses arriving randomly in time (Clough & Penzien, 1975). Therefore, since accelerograms usually have a phase of nearly constant intensity during the period of most severe one might consider modeling this phase with a white-noise process of limited duration.

It was shown that a stationary random process of finite duration could be used to model the high-intensity phase of SGM accelerogram (Liu, 1968). Since it has been assumed that the low-amplitude starting and ending portions of SGM accelerogram do not significantly affect the structural response, the stationary models have been used widely in the early years. The popularity of the stationary models refers to the fact that simulation of the stationary SGM process in the simplest form is conducted by the generation of sample functions which approach white noise. The primitive stationary models consisted of white noise process $x_1(t)$, defined as a stationary random signal having Gaussian probability distribution and constant spectral density (S_0) for all frequencies. Numerically it can be simulated by generating a sequence of Gaussian independent samples of Gaussian random process, spacing them at small time interval Δt, and assuming linear variation between amplitudes over each Δt.

Spectral analyses of existing ground motion accelerograms reveal that the Fourier amplitude spectra are not constant with frequency even over a limited band. They are somewhat oscillatory in character, may peak at one or several frequencies, and damp out with increasing frequency; all of which suggest that a stationary filtered white noise of limited duration could be more representative of actual SGMs provided the filter transfer characteristics be properly selected. The filtered white noise process $x_2(t)$ is defined as

$$x_2(t) = \int_{-\infty}^{\infty} h_0\,(t-\tau)x_1(\tau)d\tau \qquad (3.1)$$

Where $h_0(t)$ represents the transfer function in time domain. The process $x_2(t)$ is a Gaussian, covariance stationary, narrowband process. The frequency transfer function of the process in spectral domain denotes as $H_0(\omega)$

$$S_{x2}(\omega) = S_0|H_0(\omega)|^2 \qquad -\infty < \omega < \infty \qquad (3.2)$$

This equation shows that the filtered stationary process can be created from the random process $x_1(t)$ whose spectral density $S_0 \equiv 1$ by passing $x_1(t)$ trough a filter whose transfer function $H_0(\omega)$ satisfies $|H_0(\omega)|^2 = S_{x2}(\omega)$.

3.2.2. Non-Stationary Stochastic Strong Ground Motion Simulation

Although using of random process is unrealistic in describing the obvious non-stationarity of earthquake motions, such models were useful in introducing statistical concepts in earthquake engineering, and because of their simplicity were widely used. It is well known that earthquake motions are generally non-stationary with time-varying intensity and frequency content (temporal and spectral non-stationarity). Accordingly, several non-stationary stochastic models have been developed in the last years, which the most significant models can be classified into two major categories:

(a) The SGM process is modeled by passing a white noise through a filter (e.g. Bolotin, 1960; Bogdanoff *et al.,* 1961; Goldberg *et al.,* 1964, Amin & Ang, 1966; Shinozuka & Sato, 1967; Amin & Ang, 1968; Jennings, 1968; Iyengar & Iyengar, 1969), with subsequent modulation in time to achieve temporal non-stationarity. These processes have essentially time-invariant frequency content.

(b) The focus in these models is in developing a time-varying spectral representation (Housner & Jeeings, 1964; Saragoni & Hart; 1974; Levy & Wilkinson, 1976; Kaul, 1978; Wong & Trifunac, 1979; Polhemus & Cakmak, 1981; Khan, 1987; Kimura & Izumi, 1989; Collins, 1995; Haddon, 1996; Sabetta & Puliese, 1996).These models require extensive processing of the target recorded ground motion. The need for developing accelerograms from response spectra is increasing, as more non-linear dynamic analyses are being performed. Methods for generating realistic accelerograms are likely to become increasingly important, since the future design codes may require more non-linear dynamic analyses.

As mentioned before one class of SGM non-stationary simulation models is characterized by passing a white noise through a filter

$$a(t) = m(t)s(t) \qquad (3.3)$$

Where *a(t)* is the ground acceleration process, *s(t)* is a stationary process, and *m(t)* is the envelope function commonly known as the strength function. It is well known that this model is a special case of Priestley's evolutionary model (Priestly, 1965) defined by

$$a(t) = \int_{-\infty}^{\infty} m(t,\omega) e^{i\omega t}\, dz(\omega) \tag{3.4}$$

in which *m(t, ω)* is an envelope function (generally complex valued) and *dz(w)* is an orthogonal-increment process. The model in eqn. (3-4) results when *m(t, ω)* is taken to be a function of *t* only. One could easily show that the spectral decomposition of the mean-square of the process defined by eqn. (3-4) is in the form

$$E[a^2(t)] = \int_{-\infty}^{\infty} |m(t,\omega)|^2\ \phi(\omega) d\omega \tag{3.5}$$

Where *(ω)* is a spectral density function. This leads to the definition of the evolutionary PSD as the product $|m(t,\omega)|^2\phi(\omega)$, which is a function of both time and frequency. Recorded SGM usually exhibit non-stationarity in their frequency content as well as their intensity.

Several models have been introduced to account the non-stationarity in the frequency content of ground motions. Saragoni & Hart (1974) suggested using different PSD functions for different segments of the motion along the time axis. Kameda (1975) employed Priestley's evolutionary spectrum idea and obtained the ground motion through multiple filtering. Lin & Yong (1987) developed an evolutionary model based on a filtered pulse train process, where random pulses represent intermittent ruptures at the earthquake source and the filter represents the ground medium. Kiureghian & Crempien (1989) have developed a model by composing of individually modulated component stationary processes, each component representing the energy in the process in a narrow band of frequencies. Their proposed model in a sense is the complement of the model by Saragoni & Hart (1974). Whereas in Saragoni and Hart model the frequency content of the process was changed at discrete points in time, in the Kiureghian and Crempien model the strength function of the process is changed at discrete points along the frequency axis. This is accomplished by defining the process as a superposition of individually modulated stationary component processes, each representing the content in the motion in a distinct frequency band.

Recently, Thrainsson & Kiremidjian (2002) have considered the spectral non-stationarity of SGM by developing a simulation model using the inverse discrete Fourier transform. Acceleration time histories of horizontal earthquake ground motion are obtained by inverting the discrete Fourier transform, which is defined by modeling the probability distribution of the Fourier phase differences conditional on the Fourier amplitude. Accordingly, the modeling of SGM is conducted separately for Fourier amplitude and Fourier phase angle. The focus of this study is on the non-stationary energy release in time, through modeling of the Fourier phase angle differences. However, for the sake of completeness, a simple approach for the modeling of Fourier amplitude spectra is also included (Figure 3.2).

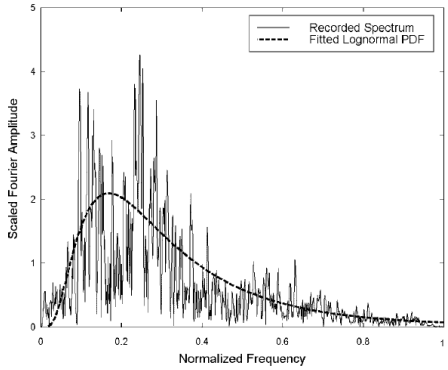

Fig. 3. 2 Scaled recorded Fourier amplitude (solid thin line) versus normalized frequency and the fitted truncated lognormal probability density function (dashed thick line) (Thrainsson & Kiremidjian, 2002).

Thrainsson & Kiremidjian (2002) have shown that the mean of the phase angle differences is independent of the Fourier amplitude, but the dispersion of the phase angle differences is dependent on the amplitudes. A lognormal and a standardized beta functions are used to describe respectively the Fourier amplitude and phase angle difference variations with frequency. Furthermore, they have developed Fourier amplitude and phase angle difference attenuation functions as a function of the magnitude, source to site distance, and local site conditions of the earthquake. Using these Fourier transform attenuation functions, ensembles of earthquake time histories can be generated for a specific site and a given magnitude–distance pair by taking the inverse Fourier transform.

Rofooei *et al.,* (2001) have used the generalized non-stationary Kanai–Tajimi model to describe and simulate the SGM time histories. They have applied the moving time-window technique to evaluate the time varying parameters of the model using actual earthquake records. The application of the model for several Iranian earthquakes Naghan (1977), Tabas (1978) and Manjil (1990) has shown that the model and identification algorithms are able to capture the non-stationary features of earthquake accelerograms. In this approach, time-varying parameters for a so called dynamic version of the Kanai–Tajimi model are considered. In order to estimate the time-dependency of the filter parameters, the 'Moving-Time-Window' technique is used. Statistical methods are then used to evaluate the time dependent amplitude envelope and the evolutionary ground frequency (Figure 3.3).

The estimated parameters corresponding to a certain window temporal position is assigned to the center point of that window. This parameter estimation process is then repeated for successive window positions. In this study $\zeta_g(t)$ is assumed to be a constant, and the time-evolution of $\omega_g(t)$ and $e(t)$ are determined in every time step. Measurement of frequency content is conducted by the use of zero-crossing method, only one dominant frequency.

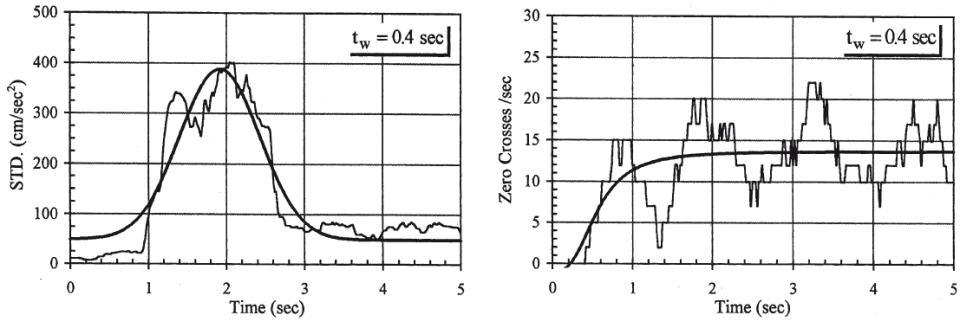

Fig. 3. 3 Variation of standard deviation and zero-crossing with time and smooth curves for Naghan 1977 earthquake (Rofooei *et al.*, 2001).

Most recently, Rezaeian & Kiureghian (2010) suggested a method for generating non-stationary synthetic SGM for specified earthquake and site characteristics defining a design scenario. The method employs a previously developed stochastic model that is based on a modulated, filtered white-noise process and incorporates both temporal and spectral non-stationarities. The model is defined in terms of a set of parameters that characterize the evolving intensity, predominant frequency, and bandwidth of the ground acceleration process. The model parameters are assigned probability distributions based on empirical data obtained from fitting the stochastic model to a subset of the New Generation Attenuation (NGA) strong motion database. They have shown that the simulated SGM acceleration as well as corresponding velocity and displacement time-histories capture the features of real earthquake ground motions, including the intensity, duration, spectral content, and peak values. Furthermore, comparison of synthetic with real elastic response spectra for a specific earthquake shows that the spectra of recorded motions are well within the range of variability of the spectra of synthetic motions.

3.2.3. Amplitude Envelope Functions

To consider the temporal non-stationarity generally the SGM simulation models applying the time-varying amplitude models which called envelope or modulating functions. The form of the envelope function is arrived at through consideration of the manner in which energy is temporally distributed throughout an accelerogram. The energy content, *I*, of the envelope function is given by

$$I = \int_0^\infty A(t)^2 \, dt \tag{3.6}$$

The energy content is an important parameter of the modulating function. Response of the structure is primarily influenced by the energy content of the envelope function rather than its shape. Several envelope functions have been suggested to model the amplitude shape function of SGM. In this following, the most significant envelope models are listed.

Exponential type

This modulating function, as shown in Figure 3.4(a), has been proposed by Shinozuka & Sato (1967) and is expressed by

$$A(t) = A_0(e^{-b_1 t} - e^{-b_2 t}) \tag{3.7}$$

Where b_1 and b_2 are the parameters which control the shape of the modulating function ($b_2 > b_1$); and A_0 is the scaling factor.

The various parameters of the modulating function are evaluated with the help of specified strong motion duration, T_0, and fraction of rise time ε. These parameters have been defined by Trifunac and Brady (Trifunac & Brady, 1975) and are expressed as

$$T_0 = t_{95} - t_5 \tag{3.8}$$

$$\epsilon = \frac{t_m}{t_{95}} \tag{3.9}$$

Where t_{95} and t_5 are the times at which the energy content of the modulating function is 95% and 5%, respectively, of the total energy content; and tm is the time at which A(t) attains the maximum value.

Box-car type

The box-car type modulating function (refer to Figure 3.4(b)) has been proposed by Tajimi (1960) and is expressed as

$$A(t) = \begin{cases} A_0 & 0 \le t \le T_0 \\ 0 & t > T_0 \end{cases} \tag{3.10}$$

Where A_0 is the scaling factor; and T_0 is the strong motion duration.

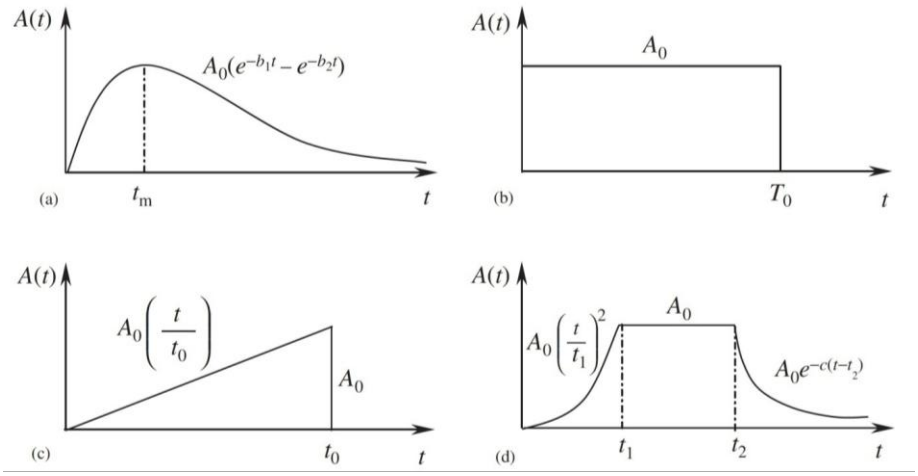

Fig. 3. 4 Different envelope functions: (a) exponential; (b) box-car; (c) triangular; (d) Amin and Ang type.

Triangular type

This modulating function, as shown in Figure 3.4(c), is defined by

$$A(t) = \begin{cases} A_0(\frac{t}{t_0}) & 0 \le t \le t_0 \\ 0 & t > t_0 \end{cases} \quad (3.11)$$

Where A_0 is the scaling factor and t0 is the duration of the modulating function.

Amin and Ang type

This modulating function initially increases parabolically (up to time t1), remains constant between times t1 and t2, and then decreases exponentially as shown in Figure 3.4(d). This is proposed by Amin & Ang (1968) and expressed by

$$\begin{cases} A_0(\frac{t}{t_0})^2 & 0 \le t \le t_0 \\ A_0 & t_1 \le t \le t_2 \\ A_0 e^{-c(t-t_2)} & t_2 \le t \end{cases} \quad (3.12)$$

Where A_0 is the scaling factor; and c is the constant.

Lognormal distribution envelope function

Unlike many of the envelopes that have previously been proposed, Stafford *et al.*, (2009) have presented a lognormal distribution based envelope function. They have presented alternative procedures that may be implemented when different analyses are required, i.e., either deterministic scenario-based analyses or analyses following on from Probabilistic Seismic Hazard Analysis (PSHA). The developed envelope function is tied directly to the expected Arias intensity (Arias, 1970) of the accelerogram given some seismological scenario as well as to two shape parameters that are in turn related to seismological parameters. The information that is required in order to derive the envelope therefore consists of information regarding the scenario, i.e., magnitude, distance, average shear-wave velocity, etc., as well as an estimate of the Arias intensity associated with this particular combination of seismological parameters. The proposed probabilistic envelope function *E(t)* is

$$E(t) = \sqrt{\frac{4gI_a}{\pi} h(t)} \quad (3.13)$$

Where I_a is the Arias intensity which is the normalized form of the energy equation 3-7 by multiplying the factor of $\frac{\pi}{2g}$, which *g* is the gravity acceleration. *h(t)* denotes the Husid probability distribution function (PDF) is assumed to be modeled by the PDF of a lognormal distribution which leads to the final expression for the envelope function (refer to Figure 3.5)

$$E(t) = \sqrt{\frac{4gI_a}{\pi} exp\left[-\frac{(\ln(t)-\mu)^2}{2\sigma^2}\right]} \quad (3.14)$$

The parameters σ and μ are formed the PDF and estimated by the use of regression empirical models which is derived by the fitting of the model to SGM data base.

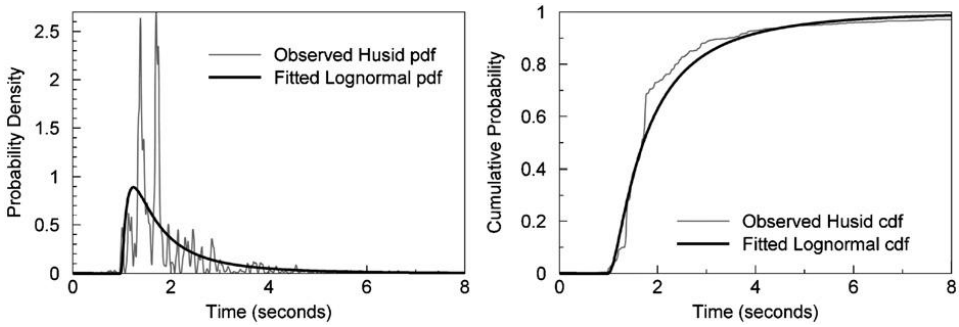

Fig. 3. 5 Fitting the lognormal PDF/CDF (left/right) envelope model to the observed Husid PDF/CDF (left/right) (Stafford *et al.*, 2009).

3.3 ARTIFICIAL NEURAL NETWORK BASED MODELS

Most conventional stochastic models for simulation of SGM are usually referred to as empirical model, since the model predicts the empirical relations with the regression analysis. Since the empirical models have been established with a fixed equation parameters, which have been based on the limited number of data, if they confront novel data that is little different from the original data, only the regression coefficients of model are usually modified. But if new data is very different from modeling data set, then not only the coefficients but also the equation form of the model should be updated. Contrariwise, artificial neural networks (ANNs) do not need a fixed equation form and instead of that, they work with a set of input and output data. Accordingly, they can continuously re-train using the new-recorded data without any change in their structures.

According to the literatures the most significant applications of ANNs based methods in engineering seismology can be classified into the following categories: (most significant studies on the application of ANNs in engineering seismology can be found in chapter 4.1.)

- Detection of the SGM process
- Identification and Picking of the seismic phases
- Generation of the ground motion signal

Generation of the ground motion signal by the use of ANNs can be performed using parametric and non-parametric models. In the first approach, the simulation process is conducted by the use of conventional stochastic models so that the parameters of the models are estimated with ANNs. In opposite of the parametric models there is non-parametric approach that conducts the simulation of accelerogram directly by the use of specified inputs like response spectra or power spectra density (PSD). On the other hand, the non-parametric ANNs models are trained to solve the inverse problem namely mapping of the spectra on the accelerogram. In the following sections these two

distinguish ANNs based SGM simulations will be discussed briefly. A short overview of the artificial neural network structures and the training process can be found in 4.1.2.

3.3.1. Parametric ANNs Model of Strong Ground Motion

Using of the design spectrum in most of seismic design codes has prescribed rather than the time history accelerogram. Although design spectrums in these procedures is undoubtedly convenient tools for the seismic design of a structure, some of the important characteristics originally contained in each spectrum can be lost through normalization and averaging processes (Katayama, 1982). In addition, the time history analysis of a structure needs well-defined recorded accelerograms or simulated accelerograms as an input load. Thus, it is important to generate the accelerograms compatible with a target spectrum. Lee & Han (2002) have developed a parametric ANNs based model to simulate SGM accelerogram and generate response spectra. Five neural-network-based models have been proposed for replacing traditional processes (Figure 3.6).

Artificial-neural-network-based model-I (ANN-I) substitutes the parameter identification process of empirical model for generating Fourier amplitude spectrum. ANN-II and ANN-III are trained to obtain the parameters of the power spectral density function and the intensity function, respectively.

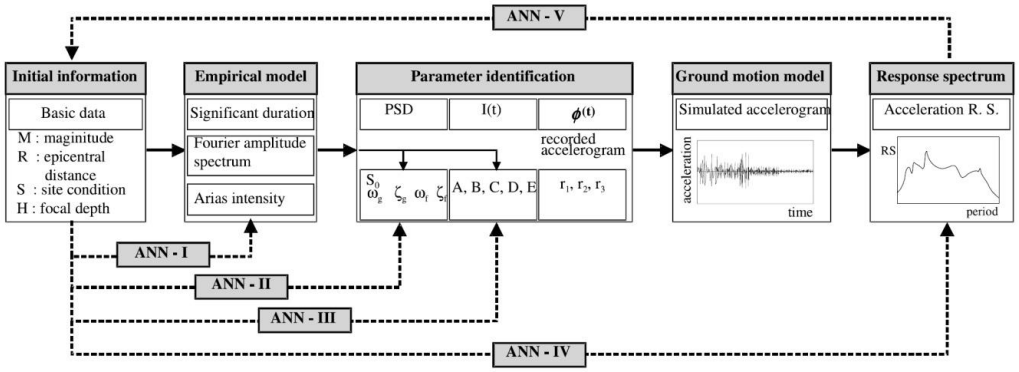

Fig. 3. 6 ANNs based parametric simulation model of SGM and response spectra (Lee & Han, 2002).

ANN-IV directly generates an acceleration response spectrum with basic information such as magnitude, epicentral distance, site conditions and focal depth. Finally, ANN-V inverses the ANN-IV, so that it can be applied to the generation of synthetic ground motion accelerograms compatible with a target response spectrum. Their suggested model produces parameters of an empirical model, which uses magnitude, epicentral distance, site condition and focal depth to simulate ground motion accelerogram.

The ANN-V is developed for the inverse model of estimation of the SGM parameters through the response spectra. Response spectra (ARS) is used as input and the initial information is considered as output, which is shown in Figure 3.7. This study shows that the procedure using neural-network-based models is applicable to generate artificial

earthquakes and response spectra. Several numerical examples are given to verify the developed models (Katayama, 1982).

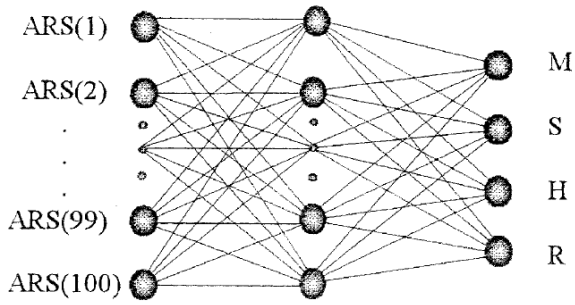

Fig. 3. 7 Response spectrum compatible accelerogram simulator (Lee & Han, 2002).

3.3.2. Non-Parametric ANNs Model of Strong Ground Motion

Earthquake response spectra are often used in analysis and design of structures. In some cases, it is desirable to develop an artificial earthquake accelerogram, or select an existing recorded accelerogram, compatible with a given response spectrum. The need for developing accelerograms from response spectra is increasing, as more non-linear dynamic analyses are being performed. Methods for generating realistic accelerograms are likely to become increasingly important, since the future design codes may require more non-linear dynamic analyses. Simulation of spectrum compatible accelerograms have been conducted by several researcher; Housner & Jennings (1964), Shinozuka & Sato (1967), Saragoni & Hart (1974), Kaul (1978), Levy & Wilkinson (1976), Wong & Trifunac (1979), Polhemus & Cakmak (1981), Khan (1987), Kimura & Izumi (1989), Collins *et al.*, (1995), Haddon (1996), Sabetta & Pugliese (1996).

Ghaboussi & Lin (1998) have proposed a non-parametric method for simulating strong ground accelerograms from response spectra. This method uses the learning capabilities of neural networks to develop the knowledge of the inverse mapping from the response spectra to earthquake accelerogram. In the proposed method, the neural networks learn the inverse mapping directly from the actual recorded earthquake accelerograms and their response spectra. This methodology is based on developing a neural network which takes the discredited ordinates of the pseudo-velocity response spectra as input, and the output of the neural network produces the Fourier spectra of the generated earthquake accelerograms. Since in discrediting the response spectra and Fourier spectra a reasonable accuracy should be maintained, they are discredited with a large number of discrete values.

A multi-layer feed-forward neural network learns to relate the response spectrum to the compressed Fourier spectrum (Figure 3.8). The model is composed of two sections. The upper part of it is the upper-half of the trained replicator neural networks. The connection weights of upper section of the AGNN remain unchanged during the training of the rest of the neural network. The lower section is a neural network which relates the pseudo-velocity response spectrum to the compressed FFT. This part of the neural network has

four layers. The input layer has 90 nodes which receive the values of the pseudo-velocity response spectrum at 90 discrete frequencies

$$S_v = \{S_v(\omega_j), j = 1, \dots, 90\} \tag{3.15}$$

$$S_v(\omega) = \omega \, max|x(t)| \tag{3.16}$$

$$\ddot{x}(t) + 2\zeta\omega\dot{x}(t) + \omega^2 x(t) = -\ddot{x}_g(t) \tag{3.17}$$

The results show that when given a pseudo-velocity response spectrum as input, the proposed method either generates an accelerograms very similar to one from its training set, one which has a pseudo-velocity response spectrum close to the input, or it synthesizes a new and realistic looking accelerogram. The proposed methodology was also tested by using design spectra as input and generating accelerograms compatible with those spectra (Ghaboussi & Lin, 1998).

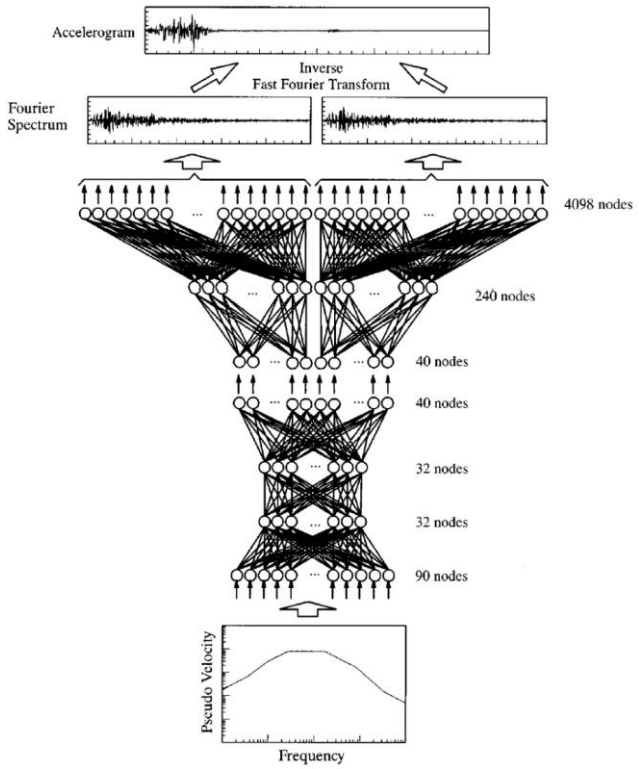

Fig. 3. 8 Accelerogram generator Neural Network (Ghaboussi & Lin, 1998).

3.4 REAL-TIME PREDICTION OF STRONG GROUND MOTION

Evolutionary simulation of SGM process during the occurrence is called real-time prediction (simulation). It is obvious that the accuracy of this type of SGM simulation models is strongly dependent on the time. Since the real-time prediction of SGM is mostly requested in building control systems to control the actuators force, the reaction time is limited to some parts of second. Reviewing of the conducted studies on the real-time prediction of SGM shows that the most of the developed models have considered the real-time prediction as a side-topic in predictive control system of structures, which work dependently and interactively to the control algorithm (Kawamura, 1990; Kawamura & Yao, 1990; Mei *et al.*, 2001). In this section the few developed real-time SGM prediction model will be reviewed and discussed briefly.

3.4.1. Time-Series based Prediction Model

Application of parametric time-series models in earthquake engineering has been considered by a number of researchers in the last few decades. In this regard, the auto regressive moving average (ARMA) model has been used to simulate the SGM's acceleration time-series (Hoshiya & Hasgur, 1978; Jurkevics & Ulrych, 1978; Polhemus & Cakmak, 1981; Chang *et al.*, 1982; Samaras *et al.*, 1985; Kozin, 1988; Conte *et al.*, 1992; Aghababaii *et al.*, 2002). By allowing the model parameters to vary with time, these models can have both temporal and spectral non-stationarity. Auto-regressive (AR) models can approximate various stochastic processes. In these models, the current deviation of the process from its mean value is expressed as a function of previous deviations and a white noise sequence. Another important model for stochastic processes is the moving average (MA) model. This model relates the current value of the process to the past values of a white noise sequence. In the prescribed models, the parameters and the white noise variances are estimated from the original seismic data. By including both AR and MA terms, one obtains a mixed ARMA model.

Aghababaii *et al.*, (2002) has used the time-varying ARMA process as a method for simulating earthquake ground motions which is capable to reproduce the non-stationary amplitude as well as the frequency content of the earthquake ground accelerations. The moving time-window technique is used to estimate the time variation of the model parameters from the actual earthquake records. In this approach, a discrete stationary linear transfer function is applied to a sequence of white noises. The output is a zero-mean stationary process with the preferred frequency characteristics that depends on the parameters of the transfer function utilized. The following time-varying ARMA model can be used to simulate SGM

$$a_k - \emptyset_{1,k} a_{k-1} - \ \ldots - \emptyset_{p,k} a_{k-p} = \sigma_k e_k - \theta_{1,k}(\sigma_{k-1} e_{k-1}) - \ \ldots - \ \theta_{q,k}\left(\sigma_{k-q} e_{k-q}\right) \quad (3.18)$$

where $\{e_k\}$ is a unit variance discrete Gaussian white noise, a_k the discrete ground acceleration to be simulated at the time step $k\Delta t$, $k = 0, 1, 2,\ldots$, with Δt being the sampling time interval. The variance envelope $\{\sigma^2_{e,k}\}$ of the Input noise represents the amplitude non-stationarity of the model. The time-varying parameters $\varphi_{i,k}$ and $\theta_{i,k}$, are

used to model the non-stationarity of the frequency content. The slow variation of the standard deviation envelope $\{\sigma_{e,k}\}$ of the model, compared to the sampling time of the earthquake process, makes the uncoupling of two types of non-stationarity possible.

Furthermore, the auto-regressive (AR) model can be used to predict SGM as a real-time model. Mei *et al.,* (2001) have introduced a real-time model used in predictive control which is constantly updated using real-time on-line observations. A real-time Feed-forward loop certainly promises to add predictive and adaptive features to the control actions to account the time dependent features in the ground motion. The ground acceleration time history can be introduced using a time-varying AR model to reflect the non-stationary features of ground motion. At each time instant $t_k = kT$; a p-dimensional AR model is formulated using the Yule–Walker equation. The simulated seismic excitation at time t_k is defined as $d(k)$. The error, $e_r(k)$; between the measured and the modeled excitation is then obtained at each step. The AR model is expressed in the state-space form and is subsequently embedded in the overall system state-space equations as follows

$$r(k+1) = A_r(k)r(k) + B_r(k)e_r(k) \tag{3.19}$$

$$d(k) = C_r(k)r(k) + D_r(k)e_r(k) \tag{3.20}$$

Where

$$r(k) = [d^T(k-p)\ d^T(k-p+1) \dots\ d^T(k-2)\ d^T(k-1)]^T \tag{3.21}$$

$$A_r(k) = \begin{bmatrix} 0 & 1 & \dots & 0 \\ \dots & \dots & \dots & \dots \\ -a_p(k) & \dots & \dots & -a_p(k) \end{bmatrix}, \qquad B_r(k) = [0 \quad \dots \quad 1] \tag{3.22}$$

$$C_r(k) = -b_0(k)\big[a_p(k) \dots\ a_1(k)\big], \qquad D_r(k) = b_0(k) \tag{3.23}$$

$a_p(k)$, $a_{p-1}(k)$, … , $a_1(k)$; $b_0(k)$ are obtained from the AR model at time t_k .

3.4.2. Prediction Model based on Conditioned Fuzzy Classifier

To realize an optimum and adaptive control of structures subjected to earthquake loading, the prediction of uncertain input waves is necessary. During the last two decades, many theoretical and experimental investigations on active and dynamic structural control have been performed. To realize an optimum and adaptive structural control system, Yao and H. Kawamura (1990) proposed an application method of fuzzy logic (also Kawamura *et al.,* 1990). In this system as shown in Figure 3.9 in order to concern the uncertainties of future loading and structural identification, fuzzy control rules described with conditioned fuzzy sets and an assumption of piecewise linear responses are employed, respectively (Figure 3.10).

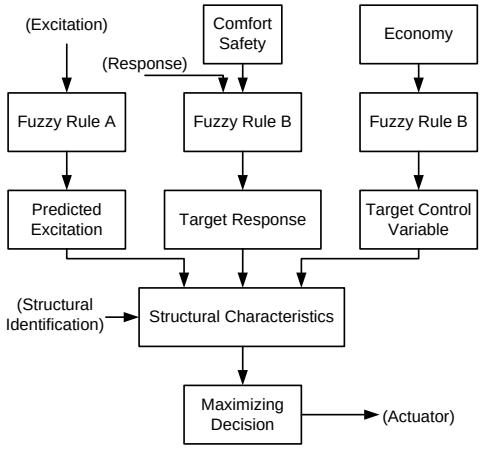

Fig. 3. 9 Flow chart of fuzzy optimum control (Kawamura & Yao, 1990).

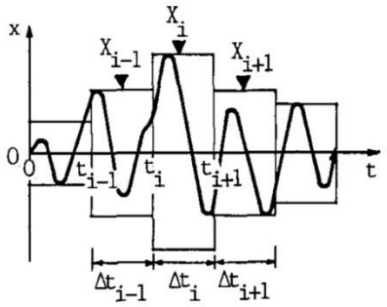

Fig. 3. 10 Piecewise SGM model (Kawamura & Yao, 1990).

Figure 3.11 shows the fuzzy rules (conditioned fuzzy sets) for the real-time prediction of the next earthquake ground motion. These rules are described from the observed four SGM records by the use of data mining method where observed acceleration is integrated into velocity every 0.01 sec. Based on the past observed SGMs, the first and second order differences Δx_i and $\Delta 2x_i$ given by Equations 3.24, 3.25 are calculated and probability mass functions of the next increment Δx_{i+1} are illustrated. By normalization, membership functions μ's of Δx_{i+1} are given as shown in Figure 3.12.

$$\Delta x_i = x_i - x_{i-1} \tag{3.24}$$

$$\Delta^2 x_i = x_i - 2x_{i-1} + x_{i-2} \tag{3.25}$$

To predict the next x^p_{i+1}, one can obtain the membership function $\mu'_{DX}(\Delta x_{i+1})$ of the next increment Δx_{i+1} by the linear interpolation as shown in Figure 3.12 in which Δx_i and $\Delta^2 x_i$ are measured. By the center of gravity method, the next increment $\Delta x'$ is determined, and the next predicted excitation x^p_{i+1} is given by

$$x_i^P = x_{i-1} + \Delta\dot{x} \tag{3.26}$$

$$\text{Or } x_{i+1}^P = x_i^P + \Delta\dot{x} \tag{3.27}$$

Equation 3.26 is used for the prediction at the beginning of interval time Δt, and equation 3.27 is used within Δt.

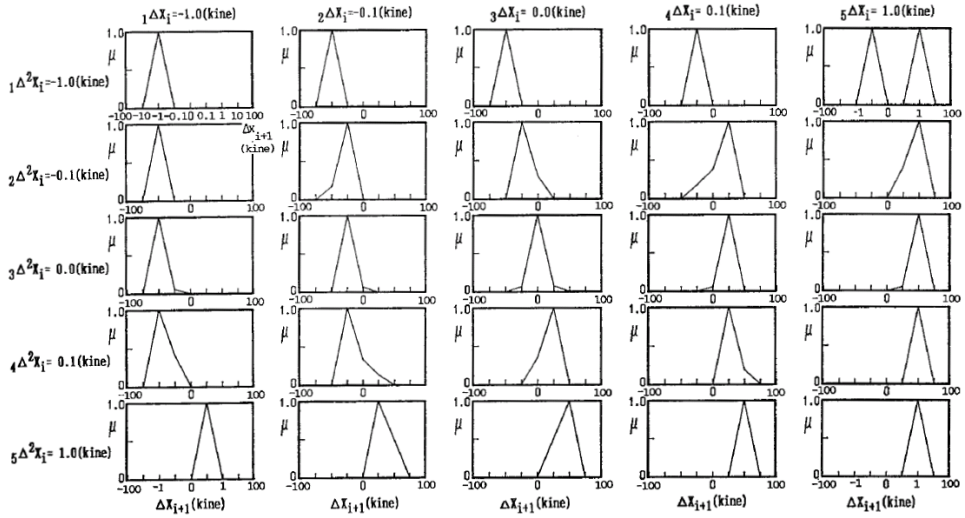

Fig. 3. 11 Fuzzy rules (conditioned fuzzy sets) for the prediction of the next earthquake ground motions (Kawamura & Yao, 1990).

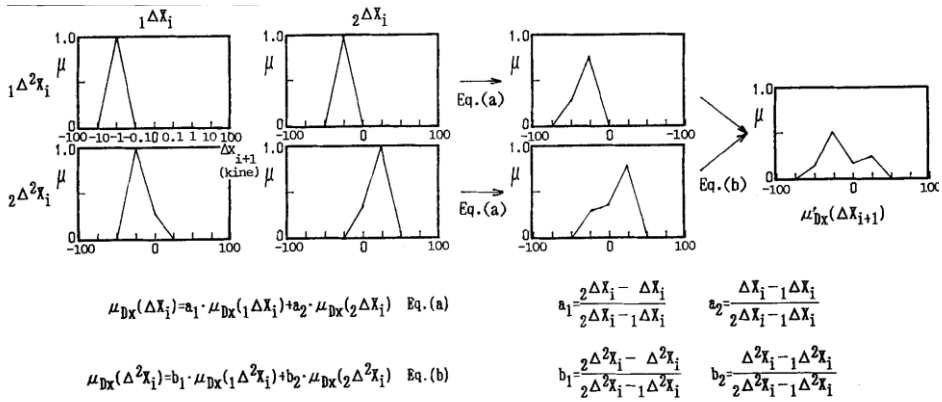

Fig. 3. 12 Linear interpolation method of conditioned fuzzy set rules (Kawamura & Yao, 1990).

3.4.3. Hybrid Prediction Model

Radeva *et al,* (2005) have suggested a model for real-time prediction of SGM on the bases of site parameters, where neuro-fuzzy model is combined with long-range dependence time-series analysis. At first classification of seismic waves is provided on the base of principle axis transformation and evolutionary power spectrum estimation. Secondly, the resonance frequency of S-wave is estimated on the base of resonance frequency of P-wave with the help of artificial intelligence methods, stochastic and neuro-fuzzy modeling. This so called hybrid model combines learning capability of neural networks with possibility of taking decision in fuzzy-logic models. Neuro-adaptive learning techniques were used for the fuzzy modeling procedure to learn information about a data set for P-wave characteristics, in order to compute the membership function parameters that best allow the associated fuzzy inference system to track the given input/output data.

For interpretation of the input/output map the model uses neural networks, which maps inputs through input membership function and associated parameters, and then through output membership functions and associated parameters to outputs. The parameters, associated with membership function were changed through the learning process. Their adjustment was facilitated by a gradient vector, which provides a measure of how well the fuzzy inference system is modeling the input/output data for a given set of parameters as power spectral density of the bedrock acceleration, the predominant frequency and the damping ratio of the soil layer. Based on the evolutionary power spectrum of the real-time measured SGM, belonging the wave to several subclasses is assessed. The model uses a database for SGM for classifying the main parameters of stochastic seismic waves. The records in the database were sorted according to their belonging to one of the separated classes and subclasses and the most important parameters characterizing each subclass, like resonance frequency, damping ratio, peak value, density distribution, etc. On the base of long-range dependence time-series analyses for each subclass different stochastic prognoses models are developed (Radeva *et al.,* 2004a). Afterward starts the module of vector quantization, which gives density distribution between target classes (Radeva *et al.,* 2004b), defined in the prognoses model in such a manner that in each class we should have the same number of target values. By the use of learning vector quantization the destructive phase model for recorded wave will be created after that. The processes of analyzing the recorded part of strong motion seismic record, classification of the wave to certain subclass and neuro-fuzzy modeling for receiving the destructive phase model are provided parallel and with a continuous updating from the recorded part of the seismic record. The process of fast estimation of strong motion seismic waves gives, as a result the destructive phase model, which can be used for further analyses and prognoses.

3.5 CONCLUSIONS

Several site-base strong ground motion simulation models were discussed in this chapter. Although the filtered stationary simulation methods are widely used in structural engineering analysis, the earthquake ground motion models based on the spectral representation method have several drawbacks. For example, they require predefined modulation functions, including their shape and duration. Moreover, the phases are usually taken as uniformly distributed and independent of each other. This characterization of the phase angles is questionable. As shown by Kubo (1987), for example, the phase angles of the ground motion affect the response of a structure. It is therefore important to accurately reproduce the characteristics of the phase angles of recorded ground motions in simulated ground motions.

The Artificial Neural Networks (ANNs) have found a wide range of usage in several engineering as well as engineering seismology applications in the recent decades. Generation of the ground motion signal by the use of ANNs can be performed using parametric and non-parametric models. In this chapter, some of the most significant applications of ANNs in simulation of SGM accelerograms are reviewed briefly.

Chapter 4
Soft-Computing based Real-Time Prediction Model

A wave type based soft-computing method for real-time prediction of Strong Ground Motion (SGM) accelerograms is developed. The four developed non-parametric models are built on the non-homogeneity of the SGM process. The models respect the different wave types of the seismic process, the individual frequency domains and their time-dependency amplitude distribution pattern.

An important part of the method is to detect dominant seismic wave phases. Two general approaches are considered in this chapter. In the first approach, the real-time prediction of the process is performed by a phase-entire model in which the early signals of an on-going seismic phase are used to predict the entire phase signal. Through the other approach, prediction of the seismic signal is done by shifting a moving window during the specified wave phase, which predicts the on-coming signal in time window $\tau+\Delta t$ based on the measured data in the current time window τ. Besides the use of constant windowing, semi-adaptive and adaptive windowing approaches were also employed. The learning capability of Artificial Neural Networks is used to establish the real-time prediction models. Application of the artificial neural networks in engineering seismology already covers a wide range of problems.

In this chapter the most important applications of Artificial Neural Networks in several fields of engineering seismology problems are reviewed briefly. After that the architecture of the neural networks and different learning paradigms of the networks are discussed. The important early-stop training approach of neural networks to avoid overfitting is presented as well. The second part of the chapter is dedicated to the developed real-time prediction models, and their components are elaborated in detail.

4.1 ARTIFICIAL NEURAL NETWORKS

4.1.1. Components of Artificial Neural Networks Model

Artificial neural networks inspired methods have found a wide range of applications in different fields of engineering during the last decades. Specifically, the ability of artificial neural networks to map the nonlinear phenomena as well as learning capability and approximation property make them very powerful tool to solve several complicated engineering problems. Artificial neural networks are categorized under the soft-computing methods, which are developed inspired by the functional aspects of biological neurons connectivity. The most frequently used model of the artificial neural network is illustrated in figure 4.1.

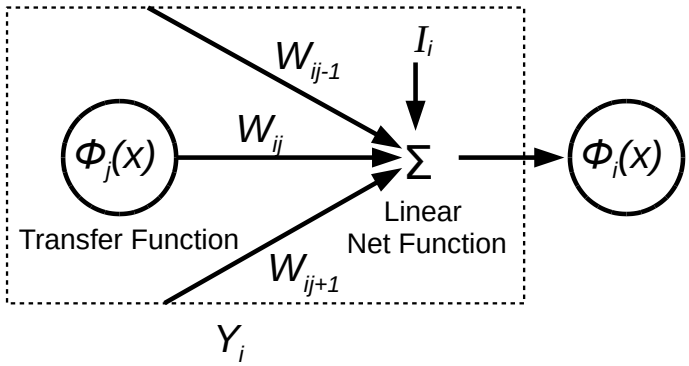

Fig. 4. 1 Artificial neural network model.

In Figure 4.1, each neuron consists of two parts: the net function and the transfer function. The net function determines how the network inputs are combined inside the neuron. Here the linear net function is shown. Set of connections between the artificial neurons create a complex structure which projects a multivariable function. The variables (weights) of the artificial neural network have to be weighted such that the desired target vector can be produced by the input vector. Mathematically the artificial neural networks with linear net functions are expressed as linear combinations of transfer functions $\Phi_j(x)$ and take the form

$$Y_i(x, W) = \sum_{j=1}^{m} W_{ij}\, \emptyset_j(x) + I_i \qquad (4.1)$$

Where m is the number of neurons in the previous layer of the network, $\Phi_j(x)$ the output of neuron j, the net input to neuron i, W_{ij} the connection weight between neuron j and neuron i and I_i the bias input associated with neuron i itself. Based on the transfer function, the form of connectivity between the artificial neurons and the learning strategy which is used the architecture of artificial neural networks system can be identified. Two types of the most used ANNs architectures, namely feed-forward back-propagation and radial basis function neural networks have been deployed in the developed soft computing based real-time prediction models. The learning paradigms and early stop training approach of ANNs will be discussed in the following paragraphs and the

structures and corresponding training approaches of the every using ANNs will be elaborated in the next sections.

4.1.2. Learning Paradigms of Neural Networks

Various methods to set the weights of the connections exist. One way is to set the weights explicitly, using a priori knowledge. Another way is to *train* the neural network by feeding it teaching patterns and letting it change its weights according to some learning rule. The majority of the networks require training in a supervised or unsupervised learning mode. The learning situations can be categorized into two aspects. These are

- *Supervised learning* in which the network is trained by providing it with input and matching output patterns. These input-output pairs can be provided by an external teacher, or by the system which contains the neural network (self-supervised). The teacher estimates the negative error gradient direction and reduces the error accordingly. As a result, most supervised learning algorithms reduce to stochastic minimization of error in multi-dimensional weight space. In learning without supervision, the desired response is not known, thus, explicit error information cannot be used to improve network behavior. Since no information is available as to correctness or incorrectness of responses, learning must somehow be accomplished based on observations of responses to inputs that we have marginal or no knowledge about (Figure 4.2).

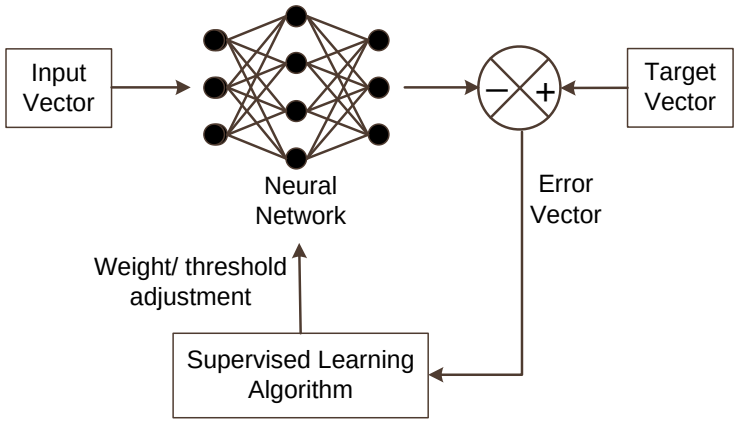

Fig. 4. 2 Schematic of the supervised learning approach.

- *Unsupervised learning* or Self-organization in which an output unit is trained to respond to clusters of pattern within the input. In this paradigm, the system is supposed to discover statistically salient features of the input population. Unlike the supervised learning paradigm, there is no a priori set of categories into which the patterns are to be classified; rather the system must develop its own representation of the input stimuli. The technique of unsupervised learning is often used to perform clustering as the unsupervised classification of objects without providing information about the actual classes. This kind of learning corresponding to minimal a priori information available.

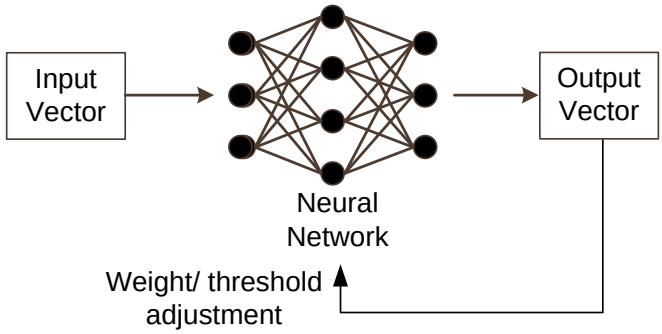

Fig. 4. 3 Schematic of the unsupervised learning approach.

The performance of artificial neural network can be superior to the conventional threshold classification method, which bases its prediction on an individual parameter, while the neural network is capable of handling collectively the complex nonlinear problems involving many implicitly correlated parameters. In spite of the usefulness of ANNs in many cases, the ANNs regarded as black box, while the physical nature of problem is ignored. Neural networks are ideal for solving problems that do not have unique and mathematically precise solutions. Any neural network representing a functional association is only expected to learn that association approximately, over the range of parameters represented in training case (Figure 4.3).

Since the artificial neural networks are designed to generalize the problem like other nonlinear estimation methods such as kernel regression and smoothing *splines*, they can suffer from either under-fitting or over-fitting. A network that is not sufficiently complex can fail to detect completely the signal in a complicated dataset, leading to under-fitting unlike a network that is too complex may fit the noise, not just the signal, leading to over-fitting. Over-fitting is especially dangerous because it can easily lead to predictions that are far beyond the range of the training data set. All standard neural network architectures such as the fully connected multi-layer perceptron are prone to over-fitting (Geman *et al*. 1992).Techniques for reducing the size of each parameter dimension are suggested to overcome the over-fitting problem, such as weight decay or early stopping. Early stopping is widely used because it is simple to understand and implement and has been reported to be superior to regularization methods in many cases, e.g. in (Finno *et al*. 1993).Validation can be used to detect when over-fitting starts during supervised training of a neural network; training is then stopped before convergence to avoid the over-fitting.

To perform the early stopping process the validation data set has been used in the following order. The training data is split to a training set and validation set in the ratio of 80 to 20 percent respectively. The training process is stopped as soon as the error on the validation set reaches the minimum value (Figure 4.4). As the result of the training processes the weights which has the network before reaching the minimum value by the validation error is selected as the training weights. This approach uses the validation set to anticipate the behavior in real use (or on a test set), assuming that the error on both will be similar: The validation error is used as an estimate of the generalization error.

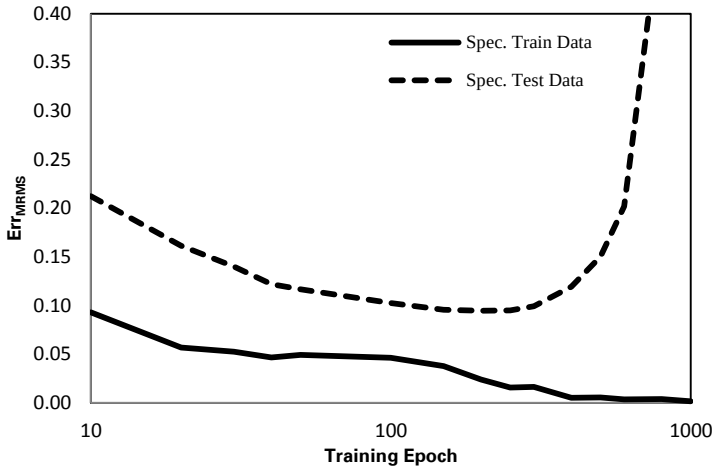

Fig. 4. 4 Training and validation (Test) error curves. Vertical and horizontal axes denote error and time (epoch number) respectively.

In this section, the most significant aspects of the learning and training process of the artificial neural networks as well as general structure of them were discussed briefly. In the next sections, we will introduce two types of the most used artificial neural networks architectures which were employed in the developed prediction models; Namely Feed-Forward Back-Propagation and Radial Basis Function artificial neural networks.

4.1.3. Application of Artificial Neural Networks in Engineering Seismology

Application of the artificial neural network in engineering seismology covers a wide range of problems. According to the literatures the most significant applications of ANNs based methods in engineering seismology can be classified into the following categories:

- Detection of the Strong Ground Motion (SGM) process
- Identification and Picking of the seismic phases
- Simulation of SGM signal

In the following sections applications of ANNs in solving engineering seismology problems will be reviewed. At the end of this section, the architecture of ANNs and the fundamental components of the method and its learning approach will be discussed.

Detection of the Strong Ground Motion Process

The early warning systems process continuously the ground motion activities to estimate the *existence* and *quiddity* of the oncoming SGM. In other words, the warning systems discriminate at first between the seismic and non-seismic events, and subsequently estimate the magnitude of the seismic event. Wang and Teng (1995) have applied a real-time artificial neural network-based pattern classification system to distinguish the earthquake events from non-earthquakes. Their real-time earthquake monitoring aims at

(1) detecting seismic events of potential interests, (2) Locating the source and estimating the size of detected events, (3) predicting the areas that could be affected by strong shaking, (4) initiating an early warning system. They have used spectral amplitudes of the picked phase window to train the network for event discrimination. A neural-network-based early warning system for finite faults have been developed by Böse *et al*. (2006). They have trained the networks to estimate the hypocenter location and moment magnitude of the oncoming event. To discriminate between exploration-generated artificial seismic event and local earthquakes E. Pezzo *et al*. (2003) have developed an automatic system. This discrimination system is based on an artificial neural network and is composed of two modules. The first is devoted to the extraction of the seismogram signatures and the second to the classification of seismic events into two classes. For the feature extraction (preprocessing stage), they used Linear Prediction Coding (LPC) algorithm.

Identification and Picking of Seismic Phases

Picking the onset of dominant seismic phases is a very important issue in engineering seismology. We know that the most destructive part of the SGM process belongs to the S-wave phase. Wang and Teng (1997) have been developed an ANNs based method to discriminating the local S phase using four feature, which were selected as input attributes of the ANNs s-phase picker: (1) the ratio between short-term average and long-term average, (2) the ratio between horizontal power and total power (3) autoregressive model coefficient (4) the short-axis incidence angle of the polarization ellipsoid. Another significant approach in seismic phase picking was developed by combining the results obtained from three back-propagation neural networks (BPNNs) seismic phase detectors Zhao and Takano (1999) have developed ANNs based detector model. The model combines of the features of short term's higher accuracy and long term's lower false alarm rate. They introduced a technique of combining multi-term detectors to solve the problem. In detail, they simultaneously run a long-term sub-detector (term=10 sec), a mid-term sub-detector (term=2.5 sec) and a short-term sub-detector (term=1.5 sec) and multiply their outputs. Through this combination, the detectors retain the features of the short-term detector's high accuracy and the long-term detector's low false alarm rate. Since the high accuracy from the long-term sub-detector is not requested, the data sample rate is reduced from 20.0 to 5.0 Hz. by resampling the data to speed up the detector's computation. The phase detection is done by shifting the moving window point by point, forming a continuous output stream, and then comparing the output with a threshold value in order to catch signals.

Generation of Strong Ground Motion Signal

One of the applications of the ANNs in the earthquake engineering and structural analysis is the generation of the SGM time history, which is requested in dynamic and nonlinear structural analysis. Ghaboussi and Lin (1998 and 2001) are the pioneer researchers, who have developed a model based ANNs to generate the SGM signal (accelerogram). Their developed approach uses the learning capabilities of neural networks to develop the knowledge of the inverse mapping from the response spectra to SGM accelerogram. Their final developed model (Ghaboussi and Lin 2002) produces a stochastic ensemble of SGM accelerograms from any response spectra or design spectra. Determining an

accelerogram from its spectrum is an inverse problem, if the calculating of the spectrum from an accelerogram is considered as a forward problem. The forward problem of calculating the response spectrum is an irreversible process since a significant amount of information is lost in going from the acceleration to its response spectrum. Mathematically based methods are not particularly suitable for solving these inverse problems because of the lack of unique solutions (for more information refer to 3.3.2). Lee and Han (2002) have employed ANNs to generate synthetic ground motion accelerograms compatible with a target response spectrum. Their suggested model estimate parameters of an empirical model, which uses magnitude, epicentral distance, site condition and focal depth to simulate ground motion accelerogram. Ghaffarzadeh and Izadi (2008) have developed an artificial generation method of spatially varying seismic ground motion using pseudo-velocity response spectrum. Spatial variation of seismic ground motion should be considered in dynamic analysis of large span structures such as dams and bridges, in which the structure's support subjected to different base excitation. They have developed two neural networks. A feed-forward back propagation neural networks was used to replicate its input vector into output vector. The main generalized regression neural network was used to generate accelerograms from pseudo velocity spectra. The SGM accelerograms recorded are collected (Kawakami, 1999, Zerva, 2002, Shama 2007) from closely spaced array of seismographs as SMART-1 array in Loting, Taiwan has been used. Their results shows that by increasing distance, acceleration values in the accelerograms tend to decrease and time shifting of peak acceleration is observed.

4.2 NON-PARAMETRIC (NP) REAL-TIME MODELING OF STRONG GROUND MOTION

Real-time seismology refers to a process in which seismic data are collected and analyzed during an on-going SGM event. One of the examples of the Real-time systems is early-warning system in which the significant features of an event are estimated from very beginning of the rupture process. Several studies have approved the correlation between the early receiving signals and magnitude, PGA and duration of the seismic event (Umeda 1990, Ilo 1995, Scrivner and Helmberger 1995, Sato and Kanamori 1999, Kanamori 2005 and Allen 2006). Precision of the estimations is strongly affected by the length of the signals which is considered after the onset of P-wave (Böse *et al*. 2008, C. W. Scrivner *et al*., 1995, T. Odaka *et al*., 2003, Richard M. Allen, 2006).

In defining a real-time prediction model the important question need to be answered is how deep history of the inputs can be used for prediction. In this study based on the correlation between the consecutive signal windows two soft computing real-time SGM prediction models are developed. The early model predicts the entire phase of an on-going SGM accelerogram according to the beginning signals. Additionally several ANNs structures have been developed to estimate the length of dominant seismic wave-phase based on the early signals. The second developed model is an evolutionary model which predicts the on-going SGM based on the consecutive measured signal windows. On the other hand, this model is established to get the measured SGM in current time window as priori to predict the on-coming signals in the following time windows. Before applying

the measured strong ground motion data to establish the prediction models, it is necessary to prepare the data in order to improve the results. The preparing process of the neural networks input/output vectors are called pre/post-processing. In the following section the most significant pre-proccesing approach which is undertaken in this study is elaborated.

4.2.1. Pre-Processing of the Accelerogram Signal

A large SGM database (182 horizontal components) has been used to train and validate real-time prediction model (see chapter 6.1 to find the information about the used database). The effective durations of the ground motion records were obtained by selecting the time interval for which the first 5% and the 95% contribution to the accelerogram intensity (integral of the square of the acceleration) take place.

For most practical applications of the artificial neural networks, the original input variables are typically preprocessed to transform them into some new space of variables where, the pattern recognition problem will be easier to solve (Bishop 2003). In the current study, the pre-processing of the input accelerograms are performed by the use of the Fourier Transformation (FT). In effect, the FT decomposes a function or a process into oscillatory functions. Therefore, the transformation will emphasize the periodic characteristic of the strong ground motion process by decomposing the signal to the constituent frequencies. Furthermore, by the use of the FT it becomes possible to generate multiple frequency data points from the limited data points. Additionally, undertaking the FT leads to the uniform length of the data vectors. Otherwise setting up of a unique neural networks with unequal data vectors would be impossible.

Accordingly the input of the neural networks is represented by the vectors of the real and imaginary parts of the Fourier transform, if $a(t)$ is the earthquake ground acceleration, the Fourier Transform has been computed by using the Fast Fourier Transform algorithm, as follows

$$A(\omega) = A_r(\omega) + iA_i(\omega) = \sum_{t=0}^{N-1} \exp\left(-\frac{i2\omega t}{N}\right) a(t)\Delta t \tag{4.2}$$

$$A_r = \{A_r(\omega_l), l = 1, \dots, n\} \tag{4.3}$$

$$A_i = \{A_i(\omega_l), l = 1, \dots, n\} \tag{4.4}$$

The real part of a transform represents the symmetric part of the curve (between 0 and 2π) and the imaginary part is antisymmetric. It is shown that the Fourier transformation leads to more frequency correlated results (Lin and Ghaboussi 2001, Zahedi Khameneh and Scherer 2008). In order to synchronize length of the input data vectors, every signal windows (input data points) is filled with zero which called zero padding and after that, the data vector is transformed by the use of FFT. It is known that zero padding does not affect the FFT of the original signal. Similarly, inverse FFT of the output vector is undertaken to return the data in the original scale (acceleration).

4.3 PHASE-ENTIRE PREDICTION MODEL (NP1)

A good starting point to establish a real-time prediction model is to consider the beginning of every dominant seismic phase as priori data to predict the entire of the dominant seismic phase (separated models for P and S-Coda). Assume $f(x)$ is the wave type based real-time SGM predictor (see Figure 4.5)

$$\left[\hat{a}(t_{1,2,\ldots,k})\right]_{phase} = f\left(a(t_1), a(t_2), \ldots, a(t_j)\right)_{phase} \quad (4.5)$$

Where $a(t_i)$ is the signal value at the time instant *i*, $\hat{a}(t_l)$ is the predicted value at the time instant *l* (The indices *phase* indicates the dominant seismic phase).

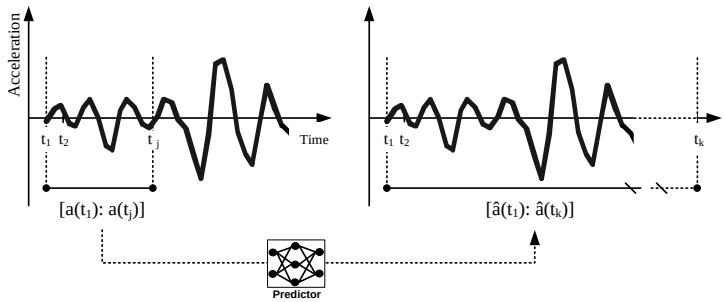

Fig. 4. 5 Phase-entire real-time SGM predictor, $a(t_i)$ and $a\hat{}(t_i)$ are the input and predicted signal respectively.

Since the prediction of SGM signal might be considered as a pattern recognition problem and the ability of the Feed-Forward neural networks to solve this kind of problems, a model based on artificial neural Networks is proposed. As it is shown in Figure 4.6 the proposed model consists of two modules; namely Duration Estimator Artificial Neural Networks (D-ANNs) and Signal Generator Artificial Neural Networks (S-ANNs). D-ANNs is implemented to estimate the wave phase length and the S-ANNs carries out the generating of SGM accelerogram according to the beginning signal of the wave phase.

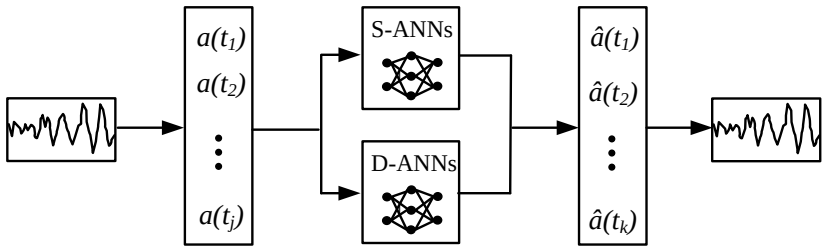

Fig. 4. 6 Schematic of the Artificial Neural Networks based prediction model.

4.3.1. Phase-Duration Estimator

As it was mentioned in order to consider the non-homogeneity of the SGM process, the process is split down into the homogeneous sub-processes in order to derive the prediction models related to the dominant sub-processes. To estimate length of the dominant seismic phase, four Feed-Forward artificial neural networks models have been designed. In the following section, the common structure of Feed-forward neural network will be reviewed and then architectures of the developed models will be discussed accordingly.

Feed-Forward Back-Propagation neural network (FFBP)

Feed-forward back-propagation multilayer network is the most widely used neural network which consists of an input layer, one or more intermediate hidden layers, and an output layer. Outputs of every layer nodes are transmitted to the nodes in the next layer through links associated with weights. The input to each node is the sum of the weight and outputs of nodes in previous layer. Each node is then activated in accordance with the summed input using a preset activation function that is usually a log-sigmoid function

$$\emptyset_j(x) = \frac{1}{1+exp(-x)} \tag{4.6}$$

The phase-duration estimator neural network uses sigmoid transfer functions in the hidden and linear transfer function in output layer (Figure 4.7). The network will produce the desired outputs when the weights are adjusted to appropriate value. As it was mentioned in the previous section, the procedure to adjust the weights is called *training* procedure. The most popular training algorithm for feed-forward multilayer networks is the back-propagation algorithm. In this algorithm, training is achieved by modifying the weights to minimize the network's mean squared error at every iteration. The trained networks are then applied to predict the length of the dominant seismic phase.

Given a training set comprising a set of input vectors $\{x_n\}$, where n=1,2, …, N, together with a corresponding set of target vectors $\{t_n\}$, the following error function (Bishop 2003) should be minimized to perform the learning process

$$E(w) = \frac{1}{2}\sum_{n=1}^{N}\|y(x_n, w) - t_n\|^2 \tag{4.7}$$

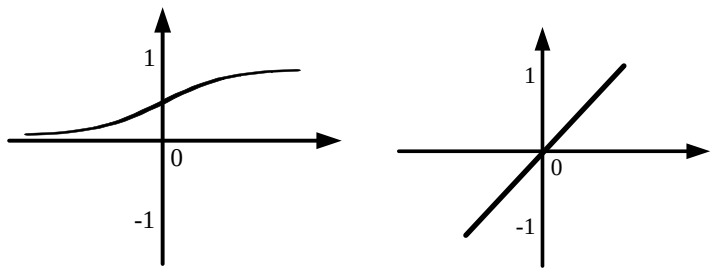

Fig. 4. 7 Logistic sigmoid Linear and transfer functions.

Network architecture

The first 0.64 Seconds (32 sample points with sample rate of 0.02 sec) of dominant seismic phase is considered as input vector to predict the length of the phase. Length of the dominant seismic phase is calculated by subtraction of P-wave onset from the dominant S-wave phase onset

$$Dur_{p\text{-}wave} = t_{s\text{-}dominant} - t_{p\text{-}dominant} \tag{4.8}$$

Length of the dominant seismic phase $Dur_{p\text{-}wave}$ is an approximation of the length of the dominant P wave for the near- and middle field events in which the P and S phases represent an overlapping.

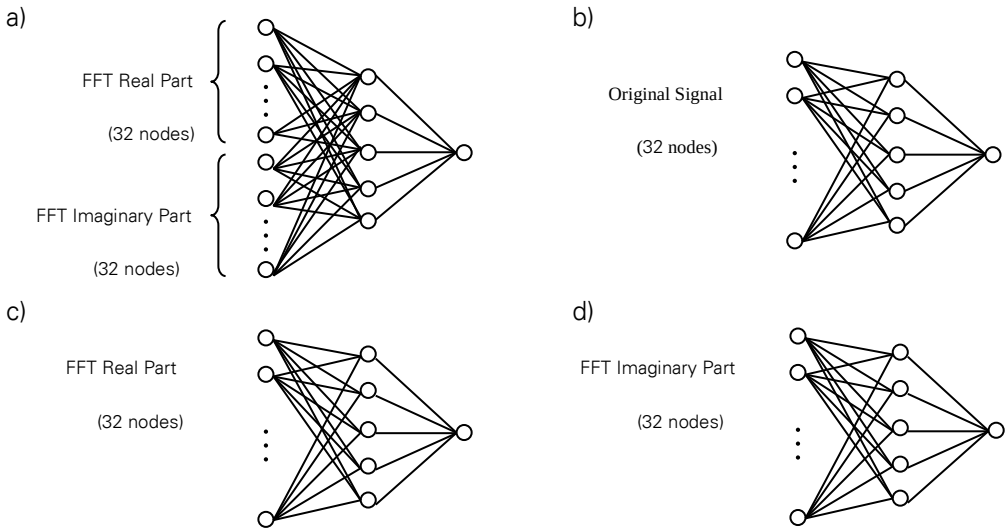

Fig. 4. 8 Structures of the duration-estimator models (D-ANNs); Model *a* has 64 nodes in input layer (32 nodes for real and 32 nodes for imaginary part of FFT) model *b* uses the original signal as input (32 sample pints). In models *c* and *d* the real and imaginary part of FFT are applied in input layer, respectively.

As it was mentioned, four different feed-forward neural network architectures have been developed to estimate the duration of the dominant seismic phase. The proposed neural network structures have one hidden and one output layer. As it is illustrated in Figure 4.8 the model *a* has 64 input nodes which are correspond to both real and imaginary part of the measured signal. In model *b* the original measured signal is fed to the artificial neural networks. The models *c* and *d* use respectively the only real or imaginary parts of the FFT.

4.3.2. Signal Generator Artificial Neural Networks (S-ANNs)

A two layer feed-forward neuronal networks is implemented to perform the prediction of the SGM accelerogram (Figure 4.9). The input layer is set to 64 nodes (32 for real and 32 for imaginary parts of FFT). Since lengths of the used data vectors are not identical, the length of the input vector is adjusted to 64 data points and the length of the target data

set is set to the longest training data set namely 256 points (5.12 seconds). The data vectors which contains less than the predefined length are filled with zero (zero padding). Number of hidden layer nodes, are adjusted to the sum of the input and outlet layer (64+512=576), which is approved during trial and error process.

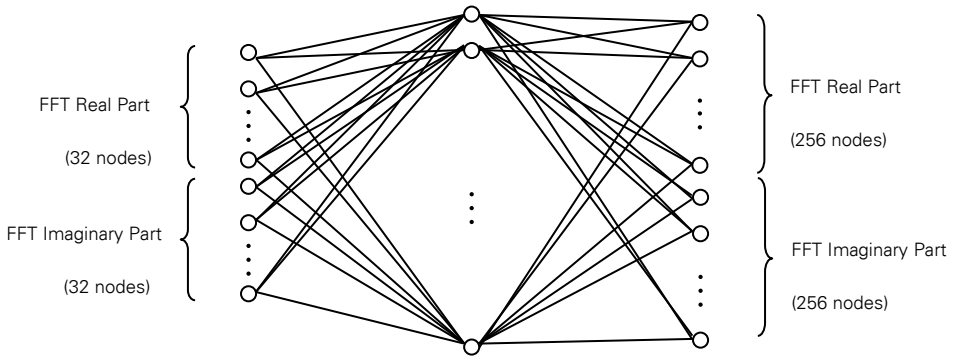

Fig. 4. 9 The structure of the signal generator artificial neural networks (S-ANNs).

4.4 EVOLUTIONARY PREDICTION MODEL (NP2)

According to the dependency between the successive signal windows in SGM process, an evolutionary prediction model is developed to predict the SGM accelerogram in time-window *(t+Δ T)* based on the measured accelerogram in time-window *t*. Assume $f(x)$ is the evolutionary wave type based real-time SGM predictor

$$\left[\hat{a}(t_{j,j+1,\ \ldots,j+k})\right]_{phase} = f\left(a(t_j), a(t_{j-1}), \ldots, a(t_{j-p})\right)_{phase} \qquad (4.9)$$

Where $a(t_i)$ is the input value at the time instant *i* for every $k \geq p; k, p \in N$, $\hat{a}(t_l)$ is the predicted value at the time instant 1 (Figure 4.10) (The indices *phase* indicates the current dominant seismic phase).

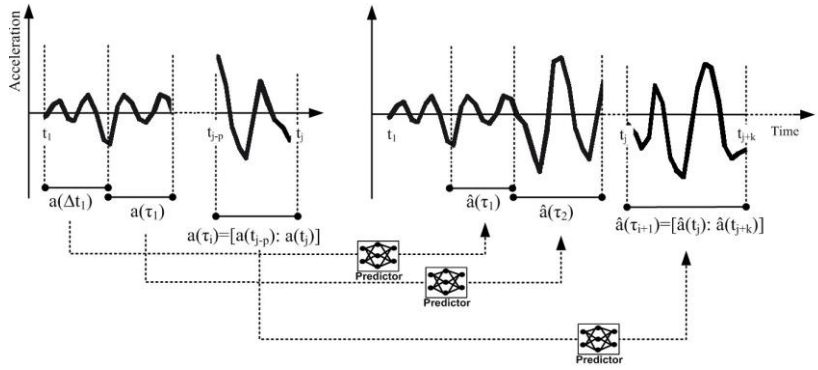

Fig. 4. 10 Evolutionary real-time SGM predictor, *a(t$_i$)* and *a^(t$_i$)* are the input and predicted signal respectively.

Although use of the constant sampling window is straightforward, it will lead to lose the signal carries the period longer than the windows length. To be able to catch the accurate dominant frequency during the time window an adaptive windowing paradigm is suggested which adjust the dominant frequency compatible sampling windows.

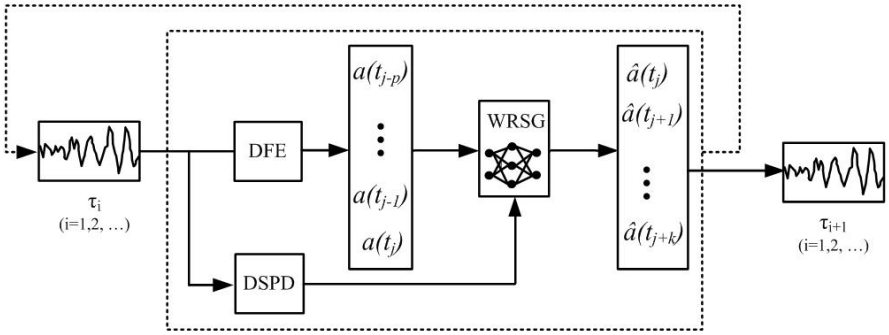

Fig. 4. 11 Components of the evolutionary real-time prediction model. Abbreviations DFE, WRSG and DSPD refer to the Dominant Frequency Estimator, Wave type Relevant Signal Generator and Dominant Seismic Phase Detector units respectively.

Due to the fact that SGM process build up of a set of different wave types (the main ones are P, S and Coda-waves) and individual propagation pattern of every wave type which leads to different onset times, the SGM process is to be considered as a non-homogenous process and for that reason every wave phase should be modeled separately to get approximately homogeneous time intervals. Therefore, an important part of the method is to detect dominant seismic wave phases. The developed wave type relevant real-time prediction model applies a radial-basis function (RBF) network to generate SGM accelerogram, due to the capability of RBF to solve pattern recognition problem (Bishop 2003). The RBF network is able to learn the data pattern in an effective manner which consumes less time than the feed forward networks. The most important components of the developed real-time model are illustrated in Figure 4.11. As it is shown, the model consists of three major units. Namely a unit to construct frequency adaptive windows, a unit to detect the dominant seismic phase and a unit to generate the strong ground accelerogram in real-time manner. In the following sections every unit will be elaborated in detail.

4.4.1. Dominant Seismic Phase Detector (DSPD)

To consider the non-homogeneity of SGM process it is assumed that the process is consisted of a set of the theoretically homogeneous phases. To be able to apply the phase relevant prediction models, discrimination of the dominant seismic phases is required. During the last decades several algorithms have been developed To distinguish the main seismic phases. Some of the recently reported techniques are wavelet transform (Okal *et al*. 2004), adaptive filtering (Oonincx 1998), singular value decomposition (Mogotra 1991), Markov amplitude (Mohanty 2007) and Time-Dependent Principal Correlation Axes (TPCA) analysis (Scherer & Bretschneider 2000). The method developed based on the TPCA analysis considers the propagation path of the seismic

wave to detect the dominant seismic phases. Comparing the other phase detection models the TPCA has the advantage of using the physical background of the strong ground motion process. The early idea of TPCA was introduced by Kubo & Penzien (1979) and is defined as the Eigenvectors of the covariance matrix of acceleration components, which is correctly defined only if the underlying process is a stochastic stationary process (the principles of TPCA are explained in 2.3.3).

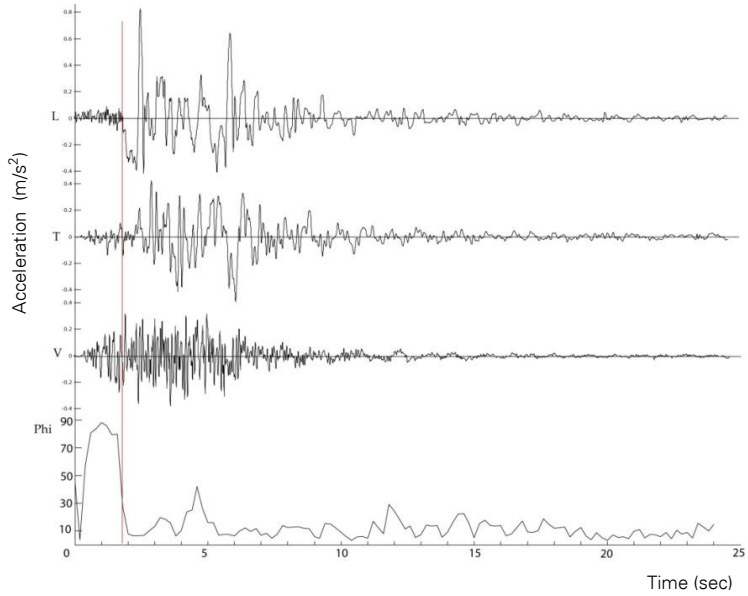

Fig. 4. 12 Three orthogonal components of earthquake Northridge. On the left side bottom the variation of the Vertical angle φ versus time is illustrated (Windowing length for stochastic principal transformation set to 1 sec, overlapping ratio is 80%). The vertical red line indicates end of the dominant P-wave phase.

The application of the technique yields in another three transformed components which are characterized by the concentration of the most significant share of energy of every time window into the component corresponding to the maximum Eigenvalue. As elaborated in Scherer & Bretschneider (2000), the course of the main principal axis T_1 reveals significant patterns, which can be analyzed by T_1's strike angle θ and elevation angle φ, defined similar to strike and rake of the slip vector in source mechanics. In a moderate distance to the rupture, high elevation indicates P-waves or Rayleigh waves, while low elevation corresponds to S waves and Love waves. Steep ascent or descent of elevation indicates a change of dominance from P to S waves and vice versa. Subsequent the detection of a wave phase change in real-time observation stream, system will replace the current wave phase relevant signal generator to up-coming wave phase relevant signal generator.

4.4.2. Dominant Frequency Estimator (DFE)

In defining the real-time predictor system one of the most important questions needs to be answered is how deep history of inputs and outputs is to be used for prediction. The

number of output nodes in a time-series predictor system is a problem-oriented task. In a one step-ahead prediction it is apparent that only one output node is sufficient as the prediction node. Correspondingly, in the case of multistep-ahead prediction, the number of output nodes should correspond to the prediction horizon, i.e. to the number of forecasts to be simultaneously presented at the network output (Palit and Popovic 2005). Prediction horizon in the SGM real-time predictor model should be adjusted so long as the dominant signal can be modeled completely.

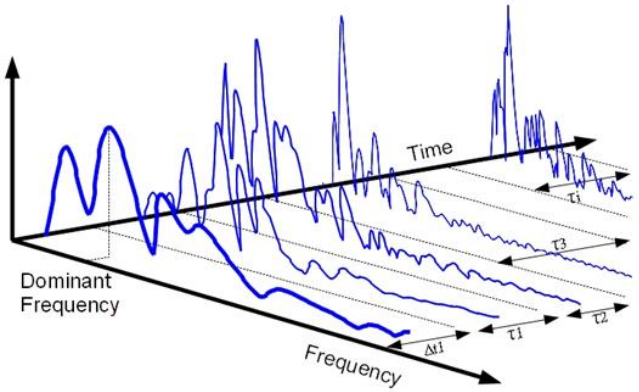

Fig. 4. 13 Adaptive windowing approach; the black solid line indicates the variation of dominant frequency during the time by the use of sliding windows. The black dashed lines indicate frequency adaptive windows.

A good starting point for this consideration is to initially assume that a constant number of available evidences can be used for every input and output prediction step. Because of the non-stationarity of the SGM process using of constant window will lead to lose the dominant signal which carries the period longer than the windows length. The shorter window's length leads to have more local picks and catches the high frequency signals, contrariwise the longer windowing results the smoothed output signal. As a rule, the time-window should be long enough to produce stable estimated parameters, while capturing the low frequency components of the earthquake record. Windows size should also be at least larger than the dominant natural period of the record so that it could properly capture the important frequency content of the earthquake. At the same time, the time-window size should be sufficiently short to capture the time evolution of the frequency content and amplitude of the record. The overlap between the successive windows must also be long enough to generate a smooth spectrum in the frequency domain. To study the role of windowing method in real-time prediction model three windowing approaches are applied in the developed real-time model; namely constant (NP2.1), semi-adaptive (NP2.2) and adaptive windowing (NP2.3).

Unlike the constant windowing method, in the developed semi-adaptive windowing approach, only the length of the start window is set to a default value and based on the frequency content of the start window by the use of a dominant frequency estimator algorithm the lengths of the following windows are determined. To establish an adaptive windowing approach the length of every sampling window has to be determined related to the dominant frequency of the previous time-window. The dominant frequency

estimator (DFE) works based on a three steps approach. At first, the length of the start window is set empirically. The effect of the start window length will be discussed in the result chapter. Secondly, the dominant frequency is computed by the mean of the runtime efficient method of zero crossing analysis. Thirdly, length of the analyzing windows is determined as one over the dominant frequency (one period length). The minimum and maximum thresholds for windows length are set unequally for P and S-Coda phases. The consequences of applying the three windowing methods in the real-prediction model are compared and discussed in the result section.

4.4.3. Wave type Relevant Signal Generator (WRSG)

Application of soft computing methods to generate SGM signal returns to the last decade. The developed models use the artificial neural networks to solve the reverse problem. Ghaboussi and Lin (1998) have developed a method which has generated spectrum compatible accelerograms using neural networks. We have established and trained a radial basis function (RBF) neural network to predict SGM accelerogram during an on-comming earthquake based on the current signals.

Radial-basis function neural network (RBF)

RBF neural networks are widely used in different fields of engineering due to their capability of fast training, generality and simplicity. A RBF network is a neural network approached by viewing the design as a curve-fitting problem in a high dimensional space. Learning is equivalent to finding a multidimensional function that provides a best fit to the training data, with the criterion for "best fit" being measured in some statistical sense. At the heart of an RBF network is the hidden layer that is defined by a set of radial-basis functions, from which the network derives its name. The RBF is similar to the Gaussian density function which is defined by a *centre* position and a 'width' parameter

$$\varphi(x) = exp(-\frac{(x-c)^2}{r^2}) \tag{4.10}$$

Where c is the centre and r is the radius (Figure 4.14). The Gaussian function gives the highest output when the incoming variables are closest to the centre position and decreases monotonically as the distance from the centre increases. The width of the RBF unit controls the rate of decrease; for example, a small width gives a rapidly decreasing function and a large value gives a slowly decreasing function. RBF networks can require more neurons than standard feed-forward back-propagation networks, but often they can be designed in a fraction of the time it takes to train standard feed-forward networks.

Network architecture

The developed radial-basis networks consist of two layers: a hidden radial-basis layer, and an output linear layer. Each hidden unit of a RBF network computes a distance function between the input vector and the center of a RBF characterizing that particular unit. On the other hand, each neuron of a multilayer perceptron computes the inner product (dot product) of the input vector applied to that neuron and the vector of associated synaptic weights.

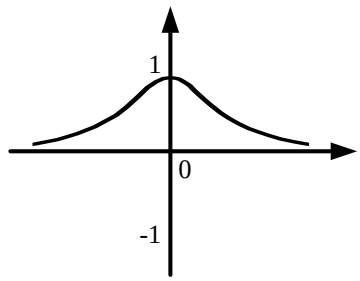

Fig. 4. 14 Gaussian radial basis transfer function.

The schematic of our suggested RBF network with *2l* inputs and *2k* outputs is depicted in Figure 4.15. As it will discuss in 4.3 the Fast Fourier transformation is applied to pre-process the input vector of the RBF neural network. The both real and imaginary parts of the Fourier transformation are applied to train the prediction model. Such a network implement a mapping $f_r: R^{2l} \rightarrow R^{2k}$ according to the output of the network at the k_{th} output node is given by

$$\hat{f}_k(x) = \sum_{i=1}^{n} b_{i,k}\, \varphi(\|x - c_i\|) \tag{4.11}$$

Where $x \in R^{2l}$ is the input vector, $\varphi(.)$ is a given function from $R^{+}$to R , $\|.\|$ denotes the Euclidean norm, $b_{i,k}$, $1 \leq i \leq n$, are the weights, $c_i \in R^n$, are known as the RBF centers. In the RBF network, the functional form $\varphi(.)$ and the centers $\mathrm{c_i}$ are assumed to have been fixed. If a neuron's weight vector is equal to the input vector (transposed), its weighted input is 0, its net input is 0, and its output is 1. If a neuron's weight vector is a distance of spread from the input vector, its weighted input is spread, its net input is *SQRT (-log(.5))* or 0.8326, therefore its output is 0.5.

To train the RBF networks actually no training is accomplished and the transpose of training input matrix is taken as the layer weight matrix (Wasserman 1993). In order to adjust output layer weights, a supervised training algorithm is employed. If for each input vector X_i in the training set, the outputs from the hidden layer are made a row in a matrix $\emptyset$, target vectors Ti are placed in corresponding rows of target matrix *T* and each set of weights associated with an output neuron is made a column of the matrix *W*, training consists of solving the following matrix equation

$$T = \emptyset W \Rightarrow W = \emptyset^{-1} T \tag{4.12}$$

Matrix *W* is, in general, not square; it is not invertible, only its pseudo inverse can be found by singular value decomposition (SVD) method (Wasserman 1993).

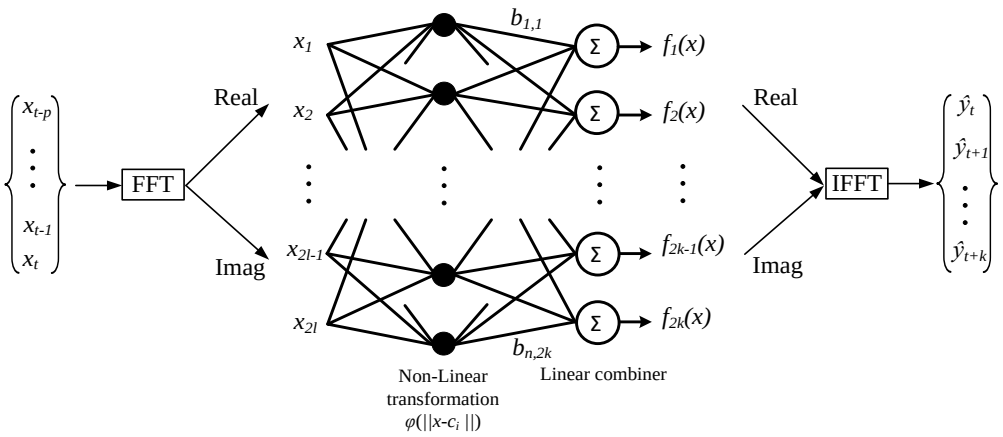

Fig. 4. 15 The developed RBF neural network signal generator and pre- and past-processing blocks.

4.5 CONCLUSIONS

As described in this chapter we have proposed two wave-type based real-time prediction models to predict the accelerogram of an on-going strong ground motion. Namely the phase-entire (NP1) and the evolutionary prediction models (NP2). The phase-entire model consisted of two parts, one for the estimation of length of the wave-phase and the other one to generate the SGM accelerogram. The developed NP1 can that take into account the non-homogeneity of the SGM process. The developed evolutionary model (NP2) consisted of the following units: a unit to detect dominant seismic phase, a units to determine the adaptive dominant frequency to set the processing windows length and a unit to generate the wave type relevant signal using RBF neural network. During the evolutionary modeling of SGM three windowing approaches are followed. Namely, constant, semi constant and adaptive approaches.

It will be shown in chapter 6 that the acceptability of the results in the case of constant windowing approach (NP2.1) is strongly related to the sampling windows length. On the other hand applying of the semi-adaptive approach (NP2.2) in which the window's length is set based on the frequency content of the beginning sampling window of every dominant seismic phase cannot represent necessarily an acceptable prediction during whole wave phase. The predicted real-time accelerogram by the use of the adaptive windowing approach (NP2.3) shows the best compatibility with the observed accelerogram comparing with the other windowing approaches. In this case the response spectrums of the predicted accelerograms show a very well adaptability in dominant period region. The best distribution along time and frequency of predicted accelerogram is obtained by the use of adaptive windowing approach. The performance of the developed prediction approaches will be discussed in detail in chapter 6.

Chapter 5
Stochastic Real-Time Prediction Model

In this chapter the developed wave type based stochastic method for real-time prediction of strong ground motion (SGM) accelerogram is described. In the developed models, the non-homogeneity of the SGM process is achieved by splitting the process in its two main dominant phases, namely P and S-Coda phases. Since separating of the temporal amplitude and spectral non-stationary characteristics of the SGM process increases flexibility and simplifies modeling and parameter estimations, two distinguished parts- one for the amplitude, and one for the non-stationary spectral content of the SGM, are suggested and developed.

In order to model the spectral amplification of several layers and modes of resonance, the multi Kanai-Tajimi filter (multi-KTF) method is applied. It provides an extended KTF by superposing multiple KTF according to the number of observed resonances to a multi-KTF. The temporal stochastic evolutionary process of the amplitudes is modeled by using the relevant wave type based envelope functions which show the best matching to the used database. The parameters of the real-time predictor model are identified and estimated by continuously matching the model to the target accelerograms. Because of the temporal nature of the amplitude envelope function, non-deterministic pattern recognition methods are suggested to be employed in real-time model estimation of the parameters of the amplitude envelope function. The envelope function is described through three parameters which are related to variables that directly represent the physical properties of the accelerogram. The parameters of the amplitude envelope are estimated by using the rising angle (tendency) of the measured data.

In this chapter, components of the stochastic real-time prediction model are represented. Applying the database the best matching amplitude envelope functions and power spectral models are established and the approach for real-time estimation of model parameters are discussed accordingly.

5.1 STOCHASTIC REAL-TIME MODELING OF STRONG GROUND MOTION

The conventional stochastic models of strong ground motion (SGM) were built fundamentally based on the assumption that strong ground acceleration can be modeled as a filtered white noise process or as a filtered Poisson process. More recently, models based on the spectral representation of stochastic processes have become more popular. Complexity of the nature of the formation of seismic waves, so that they are initiated by irregular slipping along faults followed by several random reflections, refractions, and attenuations within the complex ground formations through which they pass, a stochastic approach may be most suitable solution to model the SGM process. Despite this, the modeling of SGM based on the spectral representation method has several drawbacks. For example, it is always assumed that the SGM is a spectral stationary process, in which the spectral characteristics remain constant during the time; in addition, they require pre-assigned power spectrum, which might be totally different from the on-coming event, as well as modulation functions, including their shape and duration as it was already discussed extensively in chapter 3.

Accordingly, in establishing a stochastic parametric real-time SGM model (SP) to predict the acceleration time-histories, the non-stationarity of the process both in time and frequency domains should be considered. The temporal non-stationarity refers to the variation of the amplitude of the ground motion in time and variation of the frequency content of the ground motion in time is referred to as the spectral non-stationarity. Unlike the common SGM simulation process, in which the model parameters are set previously and remains constant during the modeling, in real-time prediction models capturing and improvement of the essential features of the real-time measured SGM, including the temporal and the spectral non-stationarity will be performed continually during the on-going measurement. Therefore, in establishing a real-time stochastic model the following specifications should be considered

- Frequency adaptive windowing; it is well known that the frequency content of SGM process is changing during the time continuously. The process starts with the high frequency P-wave phase and terminated by the low-frequency coda waves. Therefore, the SGM process should be subdivided into a sequence of time windows to represents its temporal variation. Length of the time window sequences are determined consecutively based on the predominant frequency content (see section 5. 2 and 4.2.2.2).
- Multi modes power spectra density (PSD) function; Local site effects are associated with local geological conditions, which is strongly dependent on the sedimentary (soil) deposits condition that often built up of several layers of sediment with different resonance frequencies. In general, the used PSD function should be able to map the resonance frequencies of several layers. This could include independent Kanai-Tajimi PSD for each potentially layer and are superposed additively to a multi-Kanai-Tajimi (MKT) spectrum, such as proposed by Scherer *et al.* (1988)(MKT will be discussed in section 5.1.1).

- Non-stationary power spectra (changing of the frequency content of SGM during the time); as it was mentioned previously to apply the non-stationarity of SGM process to the PSD, model parameters should be changed continuously during the process. Therefore, one way is developing the wave phase relevant PSD models, in which the parameters are extracting for every wave phase. One drawback of the phase relevant PSD model is that the spectral non-stationarity during the wave phase is ignored. This obstacle can be overcome by the use of the frequency adapting windowing approach. In this approach, the parameters of the PSD function are extracted in real-time manner in every analyzing window which will be led to a frequency non-stationary modeling of SGM process (see section 5. 2).
- Seismic phase based envelope function; several amplitude envelope functions have been developed to map the temporal non-stationarity of SGM process (the most frequently used envelope functions are listed in chapter 3.2.3). Since SGM is a non-homogenous process which is built up of a train of different seismic wave types, development of seismic phase relevant envelope functions leads to form more realistic the SGM signal (see section 5.1.2).
- Non-deterministic soft computing envelope model; since envelope function of an on-going SGM process is completed evolutionary during the time and because of lack of data, using the deterministic parameters extraction methods cannot bring a proper estimation. Therefore, by means of a soft-computing based approach the time related significant features of the on-going process will be obtained evolutionary (see section 5.3).

In the following section, formulation of the stochastic real-time prediction model will be expressed and implementation of the model components as well as real-time estimation of the model parameters will be discussed afterwards.

5.1.1. Model Construction

In this chapter, we are going to develop a method for stochastic real-time prediction of SGM, which uses information that is measured continually during the time of occurrence. For this purpose, an approach based on fitting a parameterized stochastic model to real-time recorded ground motion is developed to model the frequency content of SGM and to model the amplitude envelope function a soft-computing based method is developed as well. It is important to properly model both spectral and temporal non-stationary, particularly for inelastic and degrading structures, which tend to consider the resonant frequencies that also evolve in time.

A fully non-stationary stochastic model is developed which is based on evolutionary time-modulating filtered Gaussian white-noise, in which according to the spectral characteristics of the current time window the parameters of the filter are estimated continuously during the time. Whereas the time-modulation provides temporal non-stationarity, the variation of filter parameters over time assures the spectral non-stationarity. To map the amplitude and spectral function the developed approach is used with two separated functions, whose parameters satisfy the requirements and describe the form of random fluctuations in the stochastic model.

This method is based on the assumption that the spectral non-stationary process can approximately be assumed to be stationary within a time-window with appropriate size. The prediction model is mathematically defined by Separation of time and frequency domain

$$a(t) = A\left(t, A_{0\tau,w}, b_{\tau,w}, c_{\tau,w}\right).\ S(\omega, \zeta_{gi,\tau}, \omega_{gi,\tau}) \tag{5.1}$$

Where *a(t)* represents acceleration as a function of time. In this equation, *A* denotes the amplitude envelope function, which is a function of the parameters of wave phase relevant amplitude envelope function $A_{\tau,w}$, $b_{\tau,w}$ *and* $c_{\tau,w}$; *S* is the power spectral density function that is characterized by the damping ration $\zeta_{gi,\tau}$ and predominant frequency $\omega_{gi,\tau}$. The stochastic parameters of evolutionary envelope function are estimated for every analyzing time window τ during the seismic phase *w*. The parameters of the spectral density function are extracted for every resonance layer/mode *i* in analyzing time windows τ deterministically.

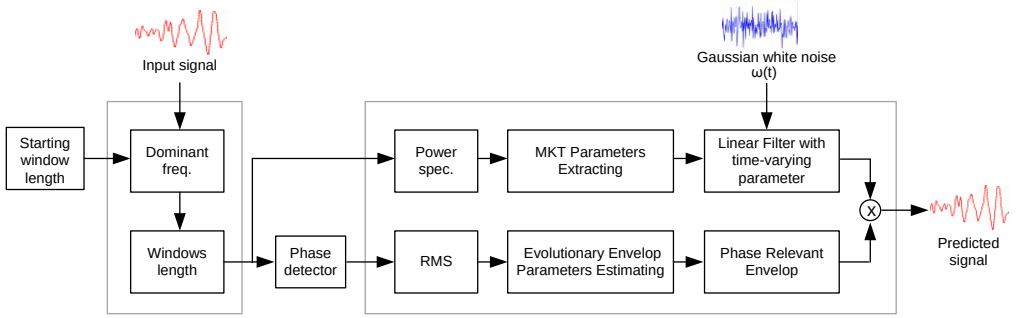

Fig. 5. 1 Schematic of the real-time stochastic prediction model.

Figure 5.1 illustrates the suggested stochastic prediction approach of the SGM process. As it is shown in frequency-domain, the extracted spectral features of the measured signal are used to filter the random Gaussian white noise. The time-domain parameters of envelope function are estimated by applying an evolutionary envelope estimation. The developed model is categorized under site based models which do not require detailed seismological information and are therefore more readily applicable to region where very few instrumental recordings have been made. The prediction approach can be used in every site of interests only by the use of single accelerometer.

Data Preparation

A large SGM database (218 horizontal components) has been used to train and validate the real-time prediction model (see chapter 6.2.1 to find the information about the using database). The effective duration of the earthquake records was obtained by selecting the time interval for which the first 5% and the 95% contribution to the accelerogram intensity (integral of the square of the acceleration) take place.

5.1.2. Modeling of Frequency Content of Strong Ground Motion

The power spectral density (PSD) function is intended to reflect the modulation of the bedrock over a wide frequency range of distributed energy of the wave train by the local underground in the frequency range. The significance of the power spectrum arises from the fact that it illustrates how the variance of the stochastic process is distributed with frequency. Frequency content of the recorded ground acceleration is generally expressed by the PSD proposed by Kanai-Tajimi (1957 and 1960)

$$S(\omega) = S_0 \frac{\left[1+4\zeta_g^2\left(\omega/\omega_g\right)^2\right]}{\left[1-\left(\omega/\omega_g\right)^2\right]+4\zeta_g^2\left(\omega/\omega_g\right)^2} \tag{5.2}$$

Where ζ_g and ω_g are respectively, the site related dominant damping and dominant frequency coefficients and S_0 is the constant power spectral intensity of the bed rock excitation. Kanai has suggested 15.6 rad/s for ω_g, and 0.6 for ζ_g, as being representative of firm soil conditions. S_0 is a scaling parameter representing the energy of the incident wave and can be replaced without loss of generality, by an external scaling size. S_0 refers to the bedrock and therefore it can be identified relatively safe from wave-type specific, empirical inspection laws of the bedrock characteristics stationary process models, which have been determined and verified in a number of studies (Aki, 1967; Ambraseys *et al.*, 1996; Ambraseys & Douglas, 2003).

In practice this parameters need to be estimated from the local earthquake records and/or site geological conditions. One disadvantage of this approaches, however is that the specific characteristics of a particular seismological scenario cannot always be accounted for, e.g., the commonly adopted PSD function proposed by Kanai-Tajimi (KT) has a shape that is only dependent upon properties of the site but not of the source. The role of the site dependent predominant frequency and damping ratio on KT-PSD function are shown in Figures 5.2 and 5.3 respectively.

KT power spectral density function may be interpreted as corresponding to a band limited white noise excitation at the bedrock level filtered through the overlying soil deposit at a site. The local soil layer can be seen as an amplifying filter, amplifies only certain frequencies, but others can pass through. This approximation is suggested by Kanai (1957). Modulation of a wave train with band limited white noise by horizontal layers in the spectrum leads to the formation of distinct, relatively slender peaks at the fundamental frequencies of these.

In spite of the popularity and wide range of use of the KT-PSD model in modeling of frequency content of the SGM process, the fundamental limitation of KT-PSD should be considered

1. The KT-PSD is a simplified spectral model of SGM process, which referred only to a single resonance frequency. For the site which consists of several deposit layers the KT-PSD is not able to map the several resonance frequencies.
2. The most serious shortcoming of the using of original KT-PSD in SGM modeling is its treatment of earthquake as stationary random processes.

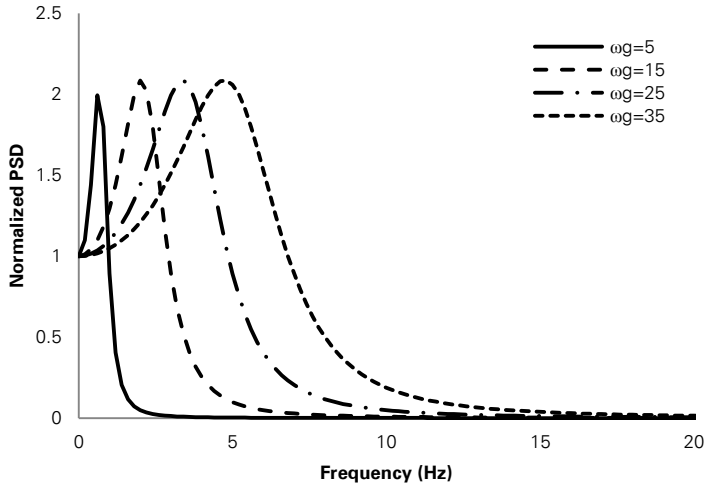

Fig. 5. 2 The effect of changing of the predominant frequency on KT-PSD for the constant damping ratio ζ_g=15%.

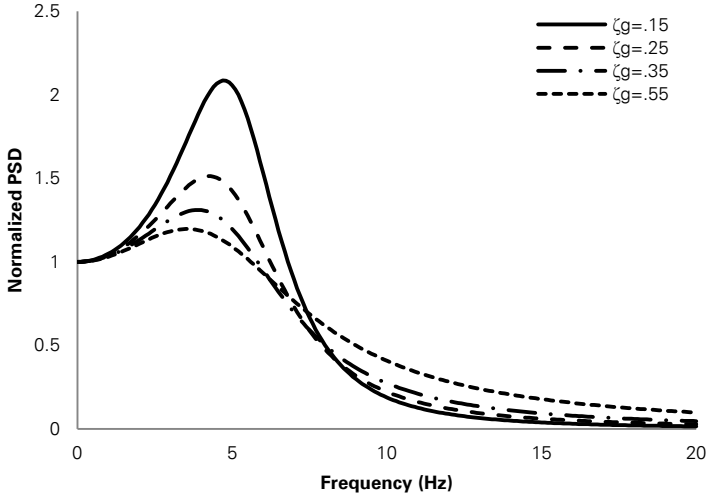

Fig. 5. 3 The effect of changing of the damping ratio on KT-PSD for the constant predominant frequency ω_g=35.

In fact, sites are often consisted of several layers of sediment with several potential resonance frequencies. It is observed that more than one predominant frequency may be present in the data, reflecting effects of topography and soil condition. In general, PSD model cannot be able to map resonant frequencies of several layers. Applying the independent KT-PSD for every potentially layer and superposing them to a multi-Kanai-Tajimi (Multi-KT) spectrum, which was proposed by Scherer *et al.* (1988), make it possible to consider the effect of *n* layer deposit in spectral modeling

$$Multi\ S(\omega) = \sum_{i=1,2,\dots,n} S(\omega, S_{0i}, \omega_{gi}, \zeta_{gi}) \tag{5.3}$$

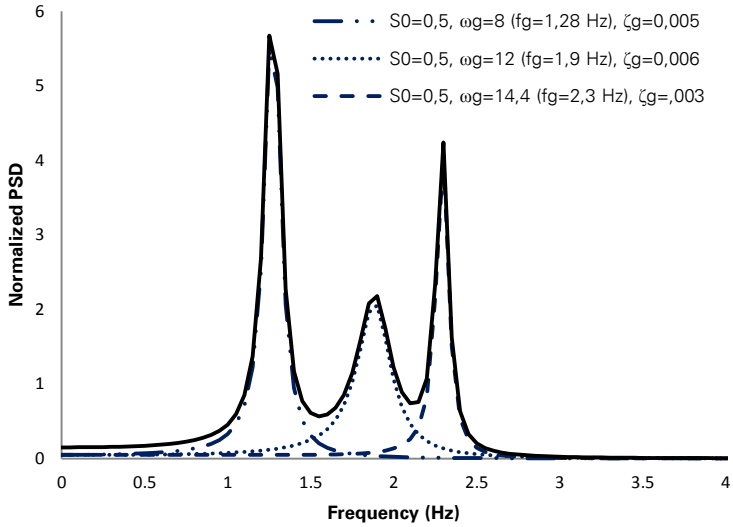

Fig. 5. 4 Multi Kanai-Tajimi Power Spectrum for three resonance modes.

Multi-KT-PSD allows the modeling of ground resonance including several resonance modes. Estimation of the mode relevant resonance parameters, S_0, ω and ζ for every mode/layer leads to refined caching of resonance features with significant amplitude. The amplitude threshold is set empirically and the less significant peaks are neglected in the prediction model. As it was mentioned previously, parameter S_0 refers to the bedrock resonance amplitude and therefore it should remain constant for all resonance modes. It is therefore physically more realistic to define the multi-KT-PSD with uniform S_0 for all layers/modes and only the parameters ω and ζ will be estimated separately for each layer in the prediction model.

The second significant shortcoming of implantation of KT-PSD in SGM prediction model as it was mentioned is the stationarity of KT-PSD. To overcome this limitation it is assumed that there is specific long enough time windows length, in which the SGM process, can be considered as a stationary stochastic process with a zero-mean and can be described by its power spectrum. Therefore, the whole process should be splitted to the sub-process in which the process remains stationary. Because of the non-stationarity of the SGM process using of constant window will lead to lose the dominant signal which carries the period longer than the windows length. The shorter window's length leads to have more local picks and catches the high frequency signals, contrariwise the longer windowing results the smoothed output signal. As a rule, the time-window should be long enough to produce stable estimated parameters, while capturing the low frequency components of the earthquake record. Windows size should also be at least larger than the dominant natural period of the record so that it could properly capture the important frequency content of the earthquake. At the same time, the time-window size should be sufficiently short to capture the time evolution of the frequency content and amplitude of the record. The overlap between the successive windows must also be long enough to generate a smooth spectrum in the frequency domain.

5.1.3. Modeling of Amplitude Envelope of Strong Ground Motion

To consider the temporal non-stationarity generally the SGM simulation models applying the time-varying amplitude (variance) models which called envelope or modulating functions. The form of the envelope function is arrived at through consideration of the manner in which energy is temporally distributed throughout an accelerogram. The energy content, *I*, of the envelope function is given basically by

$$I = \int_0^\infty A(t)^2 \, dt \tag{5.4}$$

The energy content is an important parameter of the modulating function. It has been reported (Quek *et al.,* 1990) that the response of the structure is primarily influenced by the energy content of the envelope function rather than its shape. The time-varying envelope can be estimated for single record using short time-average over the time window τ as

$$I_{[t-\tau/2,t+\tau/2]} = \frac{1}{\tau} \int_{t-\tau/2}^{t+\tau/2} A(t)^2 \; dt \tag{5.5}$$

The most frequent used amplitude envelope functions are discussed in section 3.2.3. Almost all amplitude envelope functions consider the SGM process as a homogeneous process and do not regard the fact that it is built up of several seismic waves. As it is known the most prior wave which is received is the P-wave which has the highest velocity than the other waves. Following the P-wave, the slower S-waves are arrived which carry the most energy of the earthquake. After the arriving of the body waves, it is time to reach the surface waves, Coda and the scattered wave the earth surface. According to the epicentral distance, the priority of the following waves might be different. Scherer and Schüller (1988) have recommended three basic seismic waves which are sufficient to generate a time-frequency pattern of the seismic process as illustrated in Figure 5.5; namely P, S and Surface (and Coda) waves.

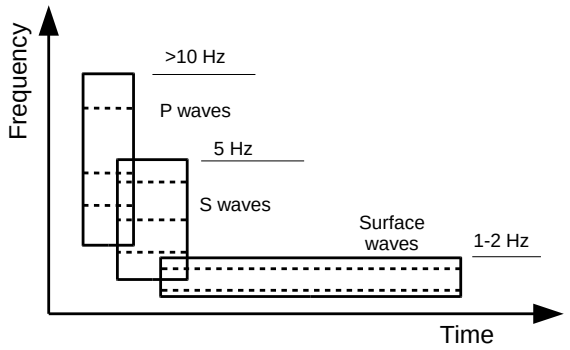

Fig. 5. 5 Simplified pattern of seismic acceleration in time and frequency (Scherer and Schüller 1988).

However, in order to model the amplitude modulation of the SGM process, the SGM is divided to the dominant P phase and the S-Coda phase. Applying the TPCA method which was elaborated in chapter 4.4.1, it is possible to discriminate the dominant seismic phases P and S. Despite of the lower amplitude of the Coda waves, the importance and

destructiveness of them is not to be underestimated. Because of the long duration of Coda waves, they always carry a great portion of the energy content of an earthquake. Furthermore, since the Coda waves exhibit the high period signals, they can cause huge damage in tall buildings as well as the long period nonstructural details.

In spite of the importance of the Coda waves, we do not develop a separated envelope function for Coda waves during the establishing of the stochastic real-time prediction model. It can be seen (Figure 5.5) that the lower frequency of the Coda waves discriminate it from the body waves in frequency domain. Nevertheless, there is not an obvious independent amplitude envelope for Coda waves in near- and middle-fields events (epicentral distance < 100 km) (see Figure 5.6). Hence, the lack of a reliable method to detect the Coda waves in near- and middle-field epicenteral distance and the absence of an independent Coda wave pattern in near- and middle-field events, eliminate the necessity of developing a separated amplitude model. Furthermore, separating of the Coda waves may cause more prediction error during the transition phase.

To establish the stochastic real-time prediction model, the SGM records of Northridge 1994 have been used (more information about the selected database can be found in 2.4). The variances of amplitude of the collected database after the following scaling process are illustrated in Figure 5.6

- SGM process is split into the dominant seismic phases P and S-Coda
- Using equation 5.5 the time-varying envelope is estimated
- The amplitude envelope is smoothed using moving average window
- The peak values are scaled to unit
- The amplitude envelopes are superposed at the point of global maxima

According to the wave type related non-homogeneity in amplitude envelope function of the SGM process it is reasonable to separately model envelope function for the dominant P-wave and S-Coda phases. The estimated amplitude envelopes (see Figure 5.6a) of the used data illustrate that the Gaussian distribution shows an acceptable fitting to P-dominant wave phase, accordingly the corresponding envelope function is defined as

$$A(t) = A_0 e^{-\frac{(x-b)^2}{2c^2}} \quad A_0, b, c>0 \tag{5.6}$$

Where *b* is the position of the centre of peak, and c controls the width of the bell shape envelope curve and A_0 is the scaling factor (see Figure 5.7).

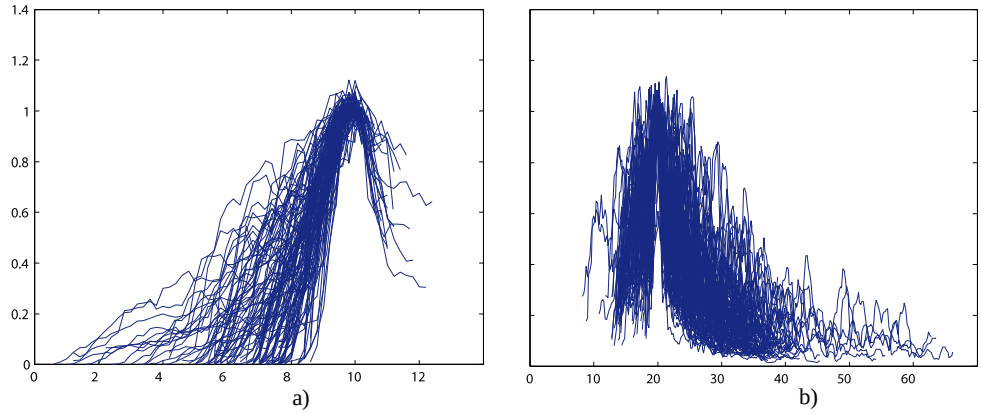

Fig. 5. 6 a) Amplitude envelope of P dominant seismic phase b) Amplitude envelope of S-Coda seismic phase (horizontal and vertical aches refer to time (sec) and scaled amplitude variance respectively).

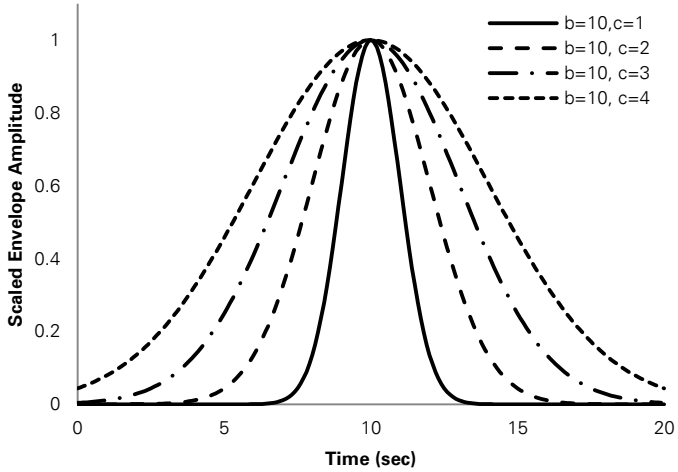

Fig. 5. 7 Gaussian envelope function for b=10 and various c.

To model the amplitude envelope of dominant S-Coda phase (see Figure 5.6b) the modulation function proposed by Shinozuka and Sato (1967) have been selected

$$A(t) = A_0(e^{-b_1 t} - e^{-b_2 t}) \;\; b_2 > b_1 \tag{5.7}$$

Where b_1 and b_2 are the parameters which control the shape of the modulation function and A_0 is the scaling factor. For generation of simulated earthquakes, b_1 has been varied from 0.25 to 0.45 and b_2 has been varied between 0.50 and 0.90 (see Figure 5.8).

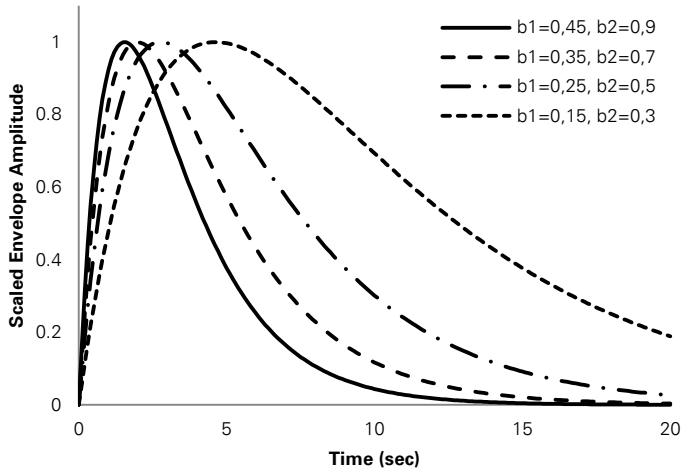

Fig. 5. 8 Shinozuka-Sato envelope function for various b_1 and b_2.

By the use of an evolutionary algorithm which will be expressed in the next section the parameters of the defined envelope functions at every time step is estimated continuously. The accuracy of the estimated fitting parameters is improved gradually during an on-going event by the use of evolutionary algorithm.

5.2 DEVELOPING THE REAL-TIME POWER SPECTRAL MODEL

As it was mentioned in 5.1.2 the multi Kanai-Tajimi power spectra density (PSD) is applied to map the multi resonance characteristics of SGM in the real-time prediction model. In order to consider the non-stationarity of SGM process, frequency adaptive windowing approach is applied to split the process into dominant frequency adaptive sub-processes. The resonance parameters of every assumed stationary sub-process is extracted from the PSD and will be used to filter Gaussian white noise process in order to form the spectral content of the following sub-process (time window sequences). PSD predictor is fundamentally established based on the assumption that the frequency distribution within a dominant wave phase changes gradually therefore the PSD pattern in a stationary sub-process can be used to build up the PSD function in the following sub-process. Accordingly establishing of spectral prediction equations and extraction of accordant parameters in the real-time prediction model is performed under the following sub-routines (see Figure 5.9)

- Estimation of PSD of every dominant frequency relevant sub-processes.
- Smoothing of PSD and detection of significant peaks.
- Extraction of PSD parameters after the fitting process for every resonance mode.
- Evaluation and correction of the extracted values for resonance parameters.

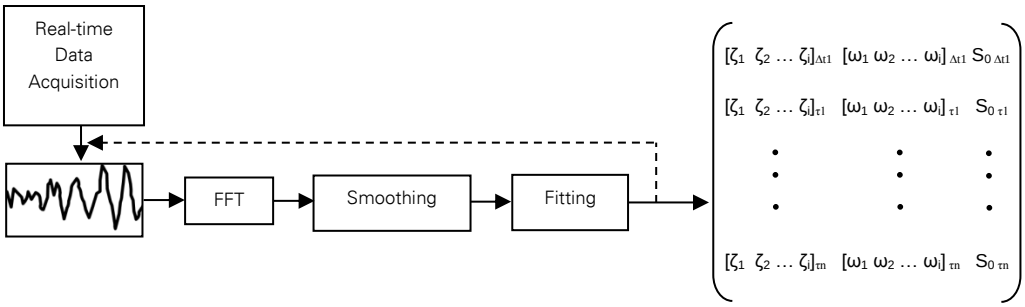

Fig. 5. 9 Real-time power spectral model.

5.2.1. Estimation of PSD parameters

In general, PSD is computed using Fourier transformation. Since ground consists not just of horizontal, homogeneous and isotropic layers, but is much more complex structure, so that the estimated spectrum may contain a great number of local peaks and valleys and is quite irregular hence it requires smoothing techniques to improve the spectrum estimator and reduce the variance, which may introduce bias or distortion to the data. Accordingly, the PSD will be smoothed using the moving average approach with the span of 0.1 Hz. The moving average treats as a low-pass filter with filter coefficients equal to the reciprocal of the moving average span. Soil damping and resonant frequency are two primary dynamic factors of soil layer(s) near the ground surface. The resonant parameters can greatly influence seismic wave responses at soil site, which plays a key role in design of geotechnical and structural engineering systems on soils (e.g. NEHRP 1997). Typically, identification of these two factors in linear and non-linear soil sites is performed by examining the frequency-dependent site-amplification factor that is normally calculated as the Fourier spectral ratio of seismic wave recordings at soil versus referenced rock sites (e.g., Borcherdt 1970 and Safak 1997). In absence of the SGM record on the rock site (reference record), the resonance parameters of the multi Kanai-Tajimi PSD (equation 5.3) are estimated by fitting the power spectrum of every sub-process. Curve fitting is strictly limited to every dominant resonance mode. However, this approach leads to several bed rock spectral amplitude parameters $S_{0,\ i}$, which is physically unclear as it is assumed to be a single bed rock. To overcome this obstacle, the S_0 value is set constant during the entire process.

In buildup of a multi mode/layer spectral model only the resonances are modeled, which cause the significant spectral peaks. Therefore, the level of 40% of the global maximum in every PSD sub-process is set to consider the Local maxima. To distinct the close resonant frequencies of the soil modes/layers, $f_{g,\ i}$, an effective width Δf is to be defined. The effective width determines minimum distance between the consequent local maximum (See Figure 5.10)

$$f_{g,i+1} \geq f_{g,i} + \Delta f_i \tag{5.8}$$

In this study Δf is set to 2.0 Hz in order to assure that only the dominant peaks are considered. Having shorter Δf would lead to more peaks, which could influence

negatively the results during curve fitting approach and over-fitting obstacle. On the other side, the longer Δf might neglect some important resonance frequencies.

Using the nonlinear least-squares method is suitable to fit the Kanai-tajimi PSD to the smoothed PSD curve. A nonlinear optimization problem with several variables and constraints should to be solved accordingly. The multi Kanai-Tajimi is approximately adjusted simultaneously for all modeled peaks. The algorithm of trust-region-reflective is used to solve the curve fitting problem. This algorithm is a subspace trust-region method and is based on the interior-reflective Newton method described by Coleman & Li (1994 and 1996). Every iteration involves the approximate solution of a large linear system using the method of preconditioned conjugate gradients (PCG).

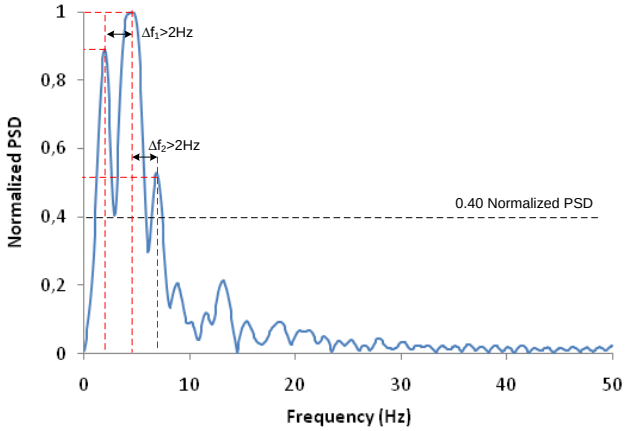

Fig. 5. 10 Distinction of the close resonance frequencies.

The convergence criteria are the convergence criteria are Residualnorm, Gradientennorm or a max. Number of iterations, depending on which is less than once a predetermined level. The nonlinear least-squares method has particular strengths with sufficiently smooth functions. Therefore, they converge in the PSD functions very quickly and actually deliver optimal parameter values.

Damping ratio summarizes the effects of mechanical damping material and the wave radiating damping through the horizontal plane of the layer. Estimation of the mode relevant damping factor ζ_i by the use of the non-linear curve fitting might be lead to unrealistic large values, in which the physical concept of the soil damping ratio is abused. Therefore, the estimated damping factor should be evaluated to check if it could satisfy the predefined restriction or not. Kanai has suggested 0.6 for damping ratio for the firm soil while the minimum and maximum values for this ratio are restricted to 0.15 and 0.55 by Ansari *et al.* (2000).

5.2.2. Applying the PSD model

The Kanai-Tajimi PSD function may be interpreted as corresponding to an ideal white noise excitation at the bedrock level filtered through overlying deposits at a site. As it was mentioned before, the serious shortcomings of the original Kanai-tajimi model are

treatment of earthquake as stationary random process and disability to model multi modes resonances. An improved version of the model which is able to capture the non-stationarity features of SGM process was introduced in 5.1.2. The non-stationarity multi resonance Kanai-Tajimi model is represented by the following equation

$$\ddot{X}_f + 2\zeta_{gi,\tau}\omega_{gi,\tau}\dot{X}_f + \omega_{gi,\tau}X_f = n(t) \tag{5.9}$$

Where X_f is the filtered response, $\omega_{gi,\tau}$ and $\zeta_{gi,\tau}$ are the resonance mode and time window dependent ground frequency and damping ratio respectively. In equation 5.9 *n(t)* is a stationary Gaussian process with the following parameters

$$E[n(t)] = 0 \; E[n(t_1)n(t_2)] = 2\pi G_0 \delta(t_1 - t_2) \tag{5.10}$$

Where *E[]* refers to the expected value, G_0 is the constant power spectral intensity of the noise, and $\delta(\,)$ is the Dirac delta function.

5.3 DEVELOPING REAL-TIME EVOLUTIONARY AMPLITUDE MODEL

According to the selected amplitude envelope functions relevant to the dominant seismic waves which were introduced in previous section, three different envelope parameters for consequent time-windows in every seismic phase should be estimated. Since the amplitude envelope function is a function of time, it is not possible to determine the parameters of the stochastic real-time envelope functions deterministically before it is completed. A model contains Artificial Neural Networks (ANNs) in combination with curve-fitting algorithm have been developed to form evolutionary amplitude envelope functions. The model parameters are identified for a large number of recorded accelerograms with known earthquake and site characteristics. The resulting observational data are used to construct predictive relations for the model parameters in terms of earthquake and site characteristics by the means of ANNs. As it was mentioned previously the SGM data of Northridge 1994 was used to build up the prediction model.

These predictive relations allow generation of the model parameters for a given set of earthquake and site characteristics. Each set of generated model parameters is used to simulate a ground motion time-history. Variation among these simulated ground motions resembles the natural variability of recorded ground motions and is an important advantage of the presented method. In the following sections, components of the evolutionary ANNs based model will be discussed and using of the trained ANNs based model in real-time prediction model will be elaborated.

5.3.1. Establishing of the Evolutionary Amplitude Envelope Model

Using the learning capability of Artificial Neural Networks (ANNs), an evolutionary model has been developed which is trained to estimate the parameter of envelope function during an on-going SGM. A large SGM free field database of Northridge 1994 records has been collected to train and evaluate the model. The amplitude evolutionary (AE) ANNs was trained for every dominant seismic phase separately. Every SGM record is split

down into frequency relevant time-windows. Therefore, the input vector for AE-ANNs is built up of the consecutive time-windows in cumulative manner (see Figure 5.11). Except the length of the starting time window (Δ_{t1}) which is adjusted manually the length of the following time windows are determined by the use of the adaptive windowing algorithm which was elaborated in 4.4.2. Accordingly, the fitted signal is split in frequency adaptive time-windows which are used to train the AE-ANNs.

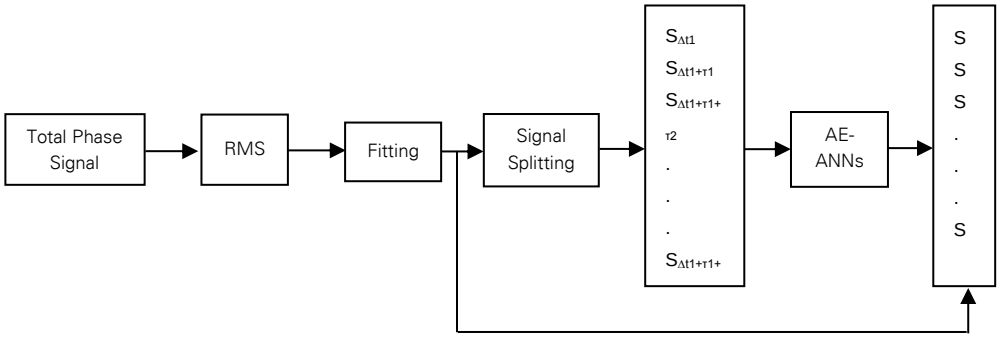

Fig. 5. 11 Training process of the evolutionary envelope model.

Preparation of the input/output vectors for training the Radial Basis Function (RBF) is conducted during the following steps

- The SGM process is split into the dominant phases P and S-Coda.
- The time-varying envelope is estimated using equation 5.5.
- The amplitude envelope is smoothed using moving average window.
- The smoothed envelope is fitted to predefined curves (the resulted curve will be used as target vector of the RBF). (see Figure 5.12)
- The fitted curve is split to the frequency adaptive windows which will be used as input vector.

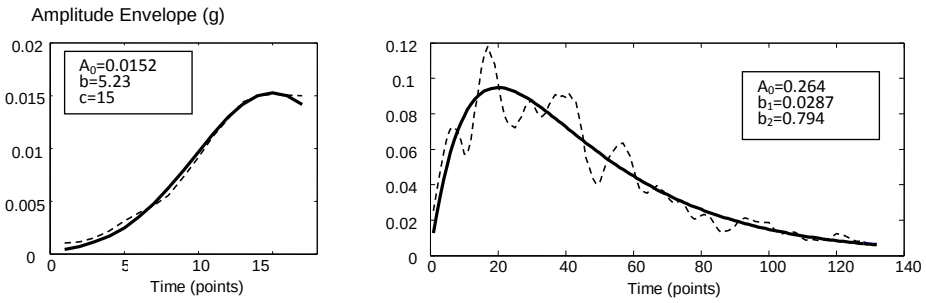

Fig. 5. 12 Fitting the envelope functions to the estimated time-varying envelope. The left and right curve indicates the fitting approach for dominant phase P and S-Coda respectively. The solid and dashed lines indicate the wave-type based observed and fitted envelopes respectively. The curve parameters are shown in the boxes.

A two layers radial-basis network (RBF) contains a hidden radial-basis and an output linear layer has been designed to form the Evolutionary Amplitude Envelope model (the structure and characteristics of the radial-basis ANNs was explained in 4.4.3 in detail). As it is illustrated in Figure 5.13 the input vector contains 128 points (64 arrays for real and 64 arrays for imaginary parts) for dominant seismic phase P and 512 points (256 arrays for real and 256 arrays for imaginary parts) for dominant seismic phase S-Coda. During the training of AE-ANNs, the networks learn to establish a relationship between the trends (rising angle) of amplitude envelope in every time-window (a part of dominant phase amplitude envelope) and whole of the dominant phase amplitude envelope which is not possible to perform by the use of deterministic functions. In other words, the evolutionary model is trained to find the most proper envelope curves corresponding to the vector of the curve segments which is completed gradually during the time. Network weight parameters are iteratively updated during a training phase until appropriate statistical models of the data are found. The results shows that the model can estimate the better fitted curve after the passing some time steps. (In section 4.2.1 it was discussed why the FFT is conducted)

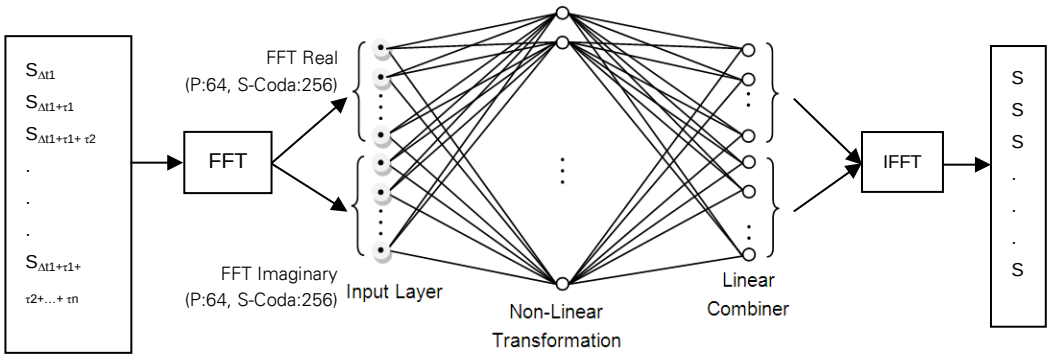

Fig. 5. 13 The architecture of amplitude evolutionary artificial neural networks (AE-ANNs).

5.3.2. Applying the Evolutionary Amplitude Envelope Model

The real-time amplitude envelope predictor employs the trained AE-ANNs to estimate the parameters of envelope function in every time-windows step. According to the calculated envelope of the measured signal, the amplitude envelope is predicted by the use of AE-ANNs. The predicted curve will be fitted to the phase relevant envelope functions and the curve parameters are collected in parameters matrices. As it is illustrated in Figure 5.14 parameters of the P-dominant seismic phase envelope function for every time-window Δt_1, $\Delta t_1+\tau_1$, ... , $\Delta t_1+...+\tau_m$ and the parameters of the S-Coda seismic phase envelope function for every time-window τ_k, $\tau_k+\tau_{k+1}$, ... , $\tau_k+...+\tau_{k+n}$, where $k=m+1$ are listed in the relevant seismic phases matrices.

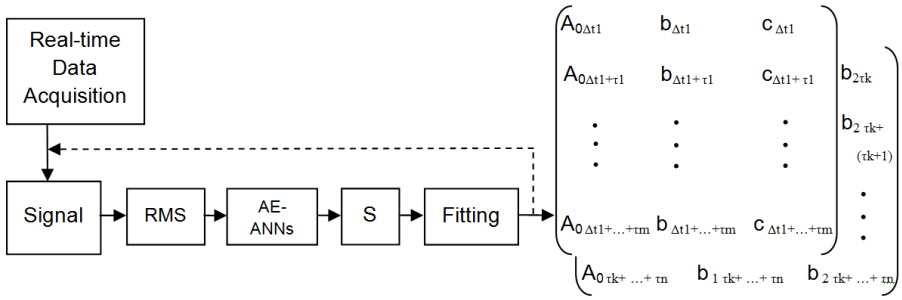

Fig. 5. 14 Applying the evolutionary amplitude envelope in real-time model.

5.3.3. Correction of the Energy Content

The predicted SGM accelerograms show that applying the real-time evolutionary envelope model can catch only the amplitude modulation form (shape) and the energy content remains still lower than the energy content of the original accelerogram. Therefore, the energy content should be corrected by the use of a relevant scaling factor. To perform the energy content correction the Arias (Arias, 1970) intensity index is applied, which calculates the energy content by the use of integral of the acceleration square. Therefore, the energy correction factor is calculated as

$$E_{cor_{\tau i}} = \sqrt{\frac{I_{env_{\tau i}}}{I_{acc_{\tau i}}}} \quad i = 1,2,\dots,n \tag{5.11}$$

Where $I_{env_{\tau i}}$ and $I_{acc_{\tau i}}$ are the Arias intensity of the envelope function and predicted strong ground motion accelerogram, respectively. Index i denotes the time windows number. The energy correction factor is calculated and applied for every time windows.

5.4 CONCLUTIONS

A parametric wave-type based real-time prediction model was described in this chapter. The developed model is categorized under the site-based model which does not require any information about the seismic source. Advantage of the developed methodology is that take into account the non-homogeneity and non-stationarity of SGM process. In the developed real-time parametric predictor, the non-homogeneity of SGM process was achieved by splitting the process in its dominant phases, namely P and S-coda. Using the frequency adaptive windowing, the SGM process was divided into the stationary sub-processes. Therefore, the non-stationarity of SGM process can be approximated very well by the use of consecutive stationary windows. The SGM process was modeled by the use of two separated temporal amplitude and spectral non-stationary models.

In order to model the spectral amplification of several layers and/or modes of resonance, multi Kanai-Tajimi filter (multi-KTF) was applied. To model the amplitude envelope functions normal distribution and Shinozuka-Sato envelopes have been used which were matched very well to the database. The results was obtained by the use of the evolutionary envelope model show that the curve parameters could be estimated very

well and the efficiency of the estimation was improved during the evolutionary approach during the time. The performance of the prediction approach will be discussed through an example in chapter 6.

Chapter 6
Application and Verification of the Real-Time Prediction Models

In this chapter the performance of the two different prediction methods including several model variations is verified by the use of several Strong Ground Motion (SGM) records which showing the main important criteria of the non-stationary SGM process. Using the selected seismic database for any specified set of earthquakes and site characteristics, sets of model parameters are generated, which are in turn used in the real-time model to predict the SGMs. At first, the application of the soft-computing based models are discussed; namely phase-entire and evolutionary models. In the following sections, the preparation and the application of the real-time stochastic prediction model are discussed from several points of view. Verification of the non-parametric entire-phase model is performed by comparison of the duration estimations obtained by the use of four different models. Besides the non-parametric phase-entire signal generator is applied as well and the predicted accelerograms are evaluated in both time and frequency domains. Following, the effectiveness of the developed non-parametric evolutionary models are verified by the use of several categorizations. Additionally, it is discussed how the windowing approach affects the predictions.

In the final section of the chapter the two distinguish parts of the developed stochastic model are verified. It is shown how well the wave-type based evolutionary amplitude envelope model can find the envelope function of the real-time measured signal and moreover the predicted accelerograms is compared to the observed data in both time and frequency domains.

6.1 APPLICATION OF the SOFT-COMPUTING BASED REAL-TIME MODEL

6.1.1. Database

The developed non-parametric methodology which uses the learning capability of artificial neural networks has been applied to two SGM databases consisting of 10 (altogether 20 horizontal components) and 91 (altogether 273 orthogonal components) free-field earthquake accelerograms for NP1 and NP2 respectively. The strong ground motion records are collected from PEER NGA database and Iranian Building and Housing research Center (BHRC). The PEER NGA database is an update and extension to the PEER Strong Motion Database, first published on the web in 1999.

To develop the non-parametric Entire-Phase real-time predictor (NP1) 20 horizontal earthquake records are chosen which belong to 10 earthquakes. Considering the Soil type, magnitude and epicentral distance the SGM records are selected. Since the soil condition is the most important factor in amplification of ground motion, the earthquake records which are measured above almost similar soil condition are selected. The selected strong ground motions belong to strong earthquakes with moment magnitude between 6 and 7.4 (more information about the database are listed in Table A.1 Appendix A). 15 randomly selected horizontal records of the SGM database has been used for training of the NP1 and the remaining SGM records being used to validate the models.

To increase the universality of the Evolutionary real-time predictor (NP2), the models are established by the use of categorized world wide SGM database. According to the following criteria the SGM records Northridge (1994), Kobe (1995), Duzce, Turkey(1999), Hector Mine (1999) and Chi-Chi, Taiwan (1995) have been collected to be applied in the model. As it can be seen in Appendix A, Table A.2 the accelerograms are collected through the earthquakes with magnitudes ranging from 6.20 to 7.72, and are recorded at the sites with Vs_{30} ranging from 200 to 715 m/s namely soil classes C and B according to Eurocode 8 (Table 6.1). The selected events from epicentral distance point of view belong to the near- and middle-field earthquakes (respectively $\leq$15 km and between 30 and 50 km). The collected data are resulting from focal mechanism strike-slip, reverse and reverse-oblique faulting regime.

All the accelerograms were resampled at 0.02 sec to synchronize the SGM records having different sample rates. The verification of the proposed models will be undertaken in the next sections in which the effect of categorization according to the epicentral distance, focal mechanism and shear wave velocity are considered.

Table 6. 1 Vs30 values for main site classes according to EC8

Site class	Vs30 [m/s]
A – Rock or other rock-like geological formation	> 800
B – Deposits of very dense sand, gravel, or very stiff clay (Stiff Soil)	360 – 800
C – Deep deposits of dense or medium-dense sand, gravel or stiff clay (Soft Soil)	180 – 360
D – Deposits of loose-to-medium cohesion-less soil (Very Soft Soil)	< 180

6.1.2. Verification of the Entire-Phase Real-Time Prediction Model (NP1)

Duration estimator artificial neural Networks

The duration estimator model (D-ANNs) was developed to estimate the length of the dominant wave phase based on the measured early signals. As described in chapter 4, to find the most effective network structures for D-ANNs, four different networks are suggested. The results obtained by 15 validation datasets are illustrated in Figure 6.1. Although the performance of the four developed D-ANNs are rather scattered for several validation datasets, altogether they show that the training process was performed well. Figure 6.1 shows that in the cases of Sarein, Iran (1997), Northridge, US (1994) and San Fernando, US (1971) earthquakes there is not a dominant difference between the results obtained by several prediction models while the other records are sensitive to the using model. Generally, it can be concluded that the networks which were trained with both real and imaginary parts of FFT can estimate precisely the length of the dominant seismic phase. The network that applies only the imaginary part of FFT seems to estimate conservatively the length of the phase.

To verify the performance of the trained D-ANNs, the networks are tested using 5 novel strong ground motion datasets (test dataset), which didn't use during training process (Figure 6.2). The randomly selected test dataset includes the horizonl components of the events Cape Mendocino (1992), Loma prieta, US (1989), Northridge, US (1994), Avaj, Iran (2002) and San fernando, US (1971). The network, which was trained only with the imaginary part of FFT follows more pricisly the pattern of the data than the others and shows better estimation of the length of the seismic phase. The results obtained by the use of D-ANNs for both validation and test datasets, show that the performance of the network, which was trained with the untransformed dataset, does not necessarily better than the networks, which applied only real or imaginaroy part of FFT. It points the importance of the applied preprocessing of input data.

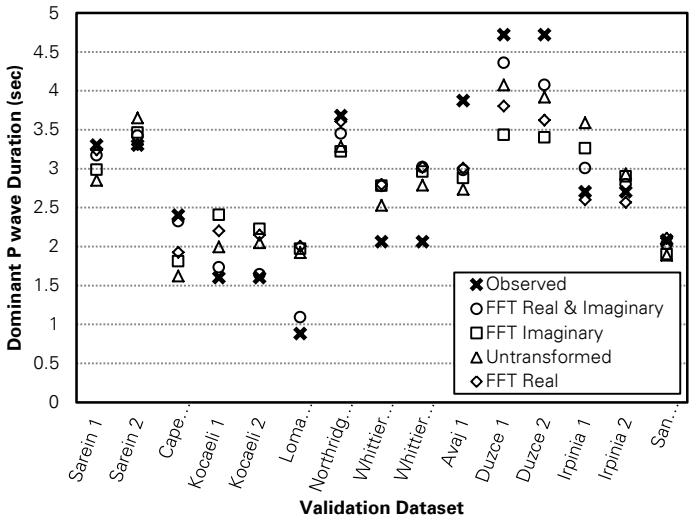

Fig. 6. 1 Estimation of the length of the dominant P-wave phase for 15 validation datasets (dominant P-wave duration is estimated according to the equation 4.8).

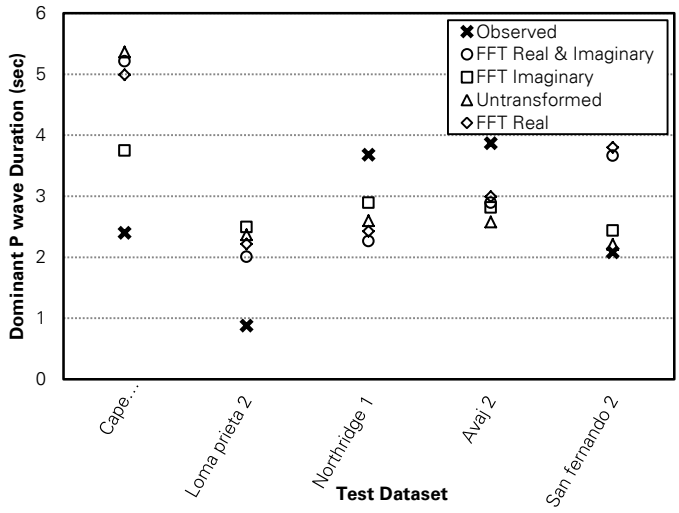

Fig. 6. 2 Estimation of the length of the dominant P-wave phase for 5 testing datasets (dominant P-wave duration is estimated according to the equation 4.8).

Signal generator artificial neural Networks (S-ANNs)

The training process in the case of the signal generator artificial neural Networks (S-ANNs) is more complicated than the D-ANNs. The convergence of the learning process for S-ANNS took definitely longer time than D-ANNs. The predicted SGM accelerograms obtained by the use of the training datasets show that the network was trained well even though the amplitude of the generated signals in some cases are lower than the observed data. As it is shown in Figure 6.3 the predicted signal can follow very well the

pattern of the observed signal in time-domain during the training process.

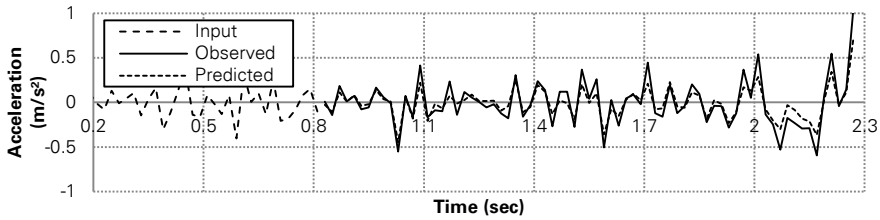

Fig. 6. 3 Evaluating the performance of the S-ANNS for validation dataset San Fernando 1 (table A.1).

To compare the evolutionary behavior of the generated signal and the original signal (target signal), normalized cumulative Arias intensity is applied. Figure 6.4 shows the Cumulative Arias Intensity (CAI) for the observed and predicted accelerogram using validation dataset. It can be seen that the CAI values of predicted signal is very similar to observed values in the beginning of the process. It has to be noted that similarity between the pattern of the CAI of the predicted and observed signal denotes that the NP1 model can very well recognize the pattern of the amplitude during the learning process.

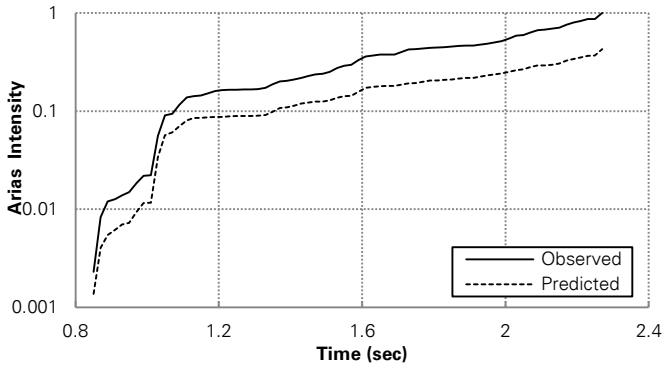

Fig. 6. 4 Normalized cumulative Arias intensity of validation dataset San Fernando 1 (table A.1).

To verify the performance of the model to map the frequency content of the SGM during the training process, the Fast Fourier power spectra of the observed and predicted accelerograms are illustrated in Figure 6.5. Obviously it can be seen that the frequency content within a wide frequency range of San Fernando 1 can be modeled very well.

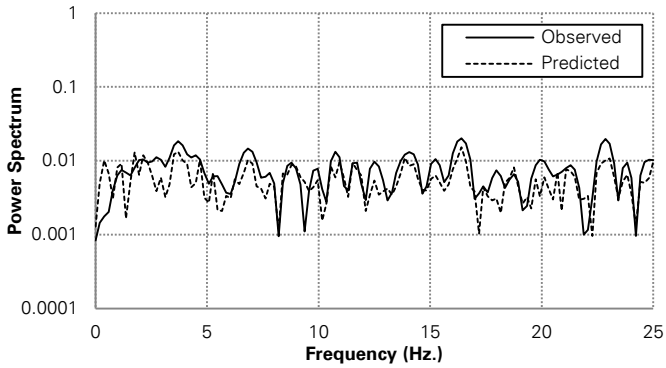

Fig. 6. 5 Power spectra of the predicted and observed validation dataset San Fernando 1 (table A.1).

In Figure 6.6, the predicted as well as the observed accelerograms by the use of a novel dataset Northridge 1 are shown. Generally, it can be seen that the predictor model NP1 could recognize the dominant pattern of the process. On the other hand, there are some peaks in which the amplitude values are predicted definitely lower than the observed values. For instance, the sudden dominant peaks around 2.1 sec and 3.0 sec which were not caught by the trained model. Nevertheless, it can be seen that the model can predict very well the peak value at 3.7 sec which arrives after some peaks at the end of the wave phase. The illustrated CAI curves in Figure 6.7 show a noticeable difference between the CAI of the predicted and observed accelerograms specially after the moment 2.0 sec as the signal's amplitude exhibits a high value of 0.7 m/s^2.

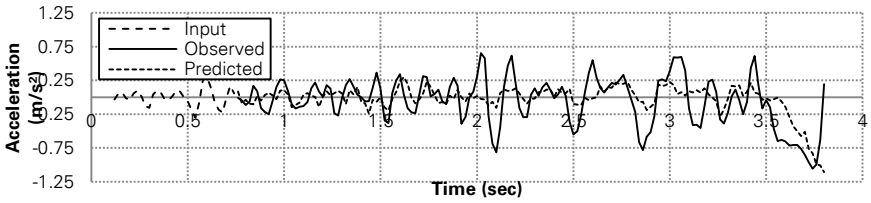

Fig. 6. 6 Evaluating the performance of the S-ANNS for test dataset Northridge 1 (table A.1).

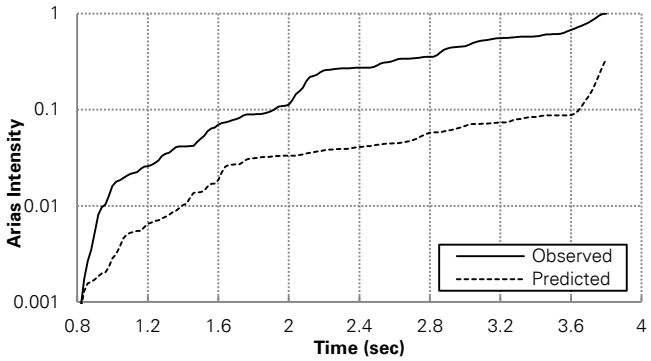

Fig. 6. 7 Normalized cumulative Arias intensity of validation dataset San Northridge 1 (table A.1).

As it is shown in Figure 6.8 the performance of the NP1 in frequency domain is obviously more acceptable than in time domain. The power spectrum of the predicted test accelerogram Northridge 1 shows that the predominant and high frequency parts of the signal (> 13 Hz.) are predicted very well. The energy of the low frequency signal around 5.0 and 7.0 Hz were underestimated.

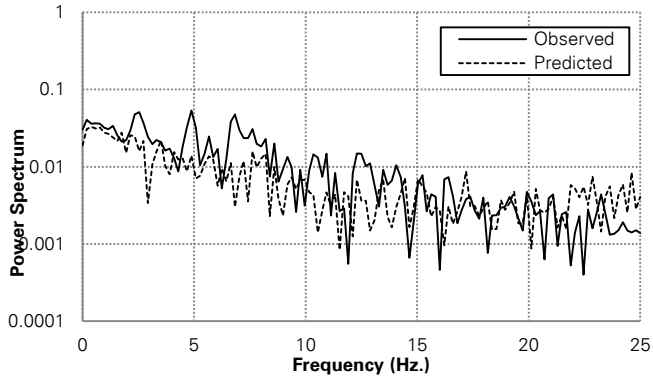

Fig. 6. 8 Power spectra of the predicted and observed test dataset Northridge 1 (table A.1).

6.1.3. Verification of the Evolutionary Real-Time Prediction Model (NP2)

Verification of the model

To quantify the error between the observed and predicted accelerograms during the training process of the RBF neural network the following error index based on the commonly used RMS is suggested

$$Err_{MRMS} = \frac{1}{\max(|y_{obs}|)} \sqrt{\frac{1}{N}\sum_{i=1}^{N}\left(y_{obs} - \hat{y}_{pred}\right)^2} \tag{6.1}$$

Where y_{obs} is the observed data, $\hat{y}_{pred}$ is the predicted data, N denotes the number of observations. The modification in RMS is carried out to scale the RMS-error to the phase relevant peak value. The error estimation is undertaken for predicted accelerogram and the corresponding response spectrum.

Early stopping training technique

During training of a neural network the goal is to obtain a network which has the optimal generalization performance. However, all neural network architectures are prone to over fitting. While the network seems to get better and better, i.e., the error on the training set decreases, at some point during training it actually begins to get worse again, i.e., the error on unseen examples (testing data set) increases. One of the straightforward ways to overcome the over fitting problem is the early stopping technique (Prechelt, L. 1998). At first, the training data set is split to training set and a validation set.

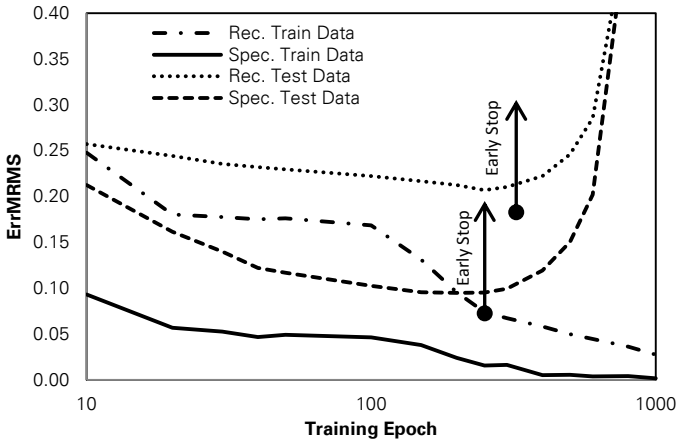

Fig. 6. 9 Training epochs of the RBF neural network by the use of modified RMS-error index. The estimated average error for training and test validation dataset for accelerogram record (Rec.) and corresponding response spectrum (Spec.) are illustrated.

The network is trained using only the training set and evaluate the per-example error on the validation set once in a while, e.g. after every ten epoch. The training will be stopped as soon as the error on the validation set is higher than it was the last time it was checked (see Figure 6.9). This approach uses the validation set to anticipate the behavior

in real use (or on a test set); assuming that the error on both will be similar: The validation error is used as an estimate of the generalization error.

Efficiency of the learning process

Figures 6.10, 6.11 and 6.12 show the performance of the trained RBF neural network on one of the 55 training SGM accelerograms in category of the reverse faulting (in the next section it will be shown that the best results are obtained by the use of the categorizing based on the focal mechanism). The record in time window t of this accelerogram was provided as the input to the developed RBF neural network and its output provided the record in the time window $t+\Delta t$ of the predicted accelerogram.

Comparison between the observed and predicted accelerograms (see Figure 6.10) indicates that the trained RBF neural network has learnt the training cases very well. Almost the amplitudes of all peaks as well as peak positions are predicted correctly. Similarly, comparing the response spectra of the observed and predicted accelerograms which are illustrated in Figure 6.11 shows that the response spectrum of the predicted accelerogram is very close to the response spectrum of the observed accelerogram and the predominant period range for the damping ratio of 5% is modeled very precisely.

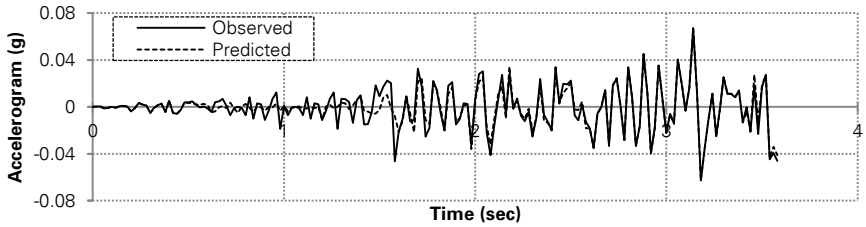

Fig. 6. 10 Observed and predicted accelerogram for validation accelerogram Northridge-01(14) using adaptive windowing approach (NP2.3).

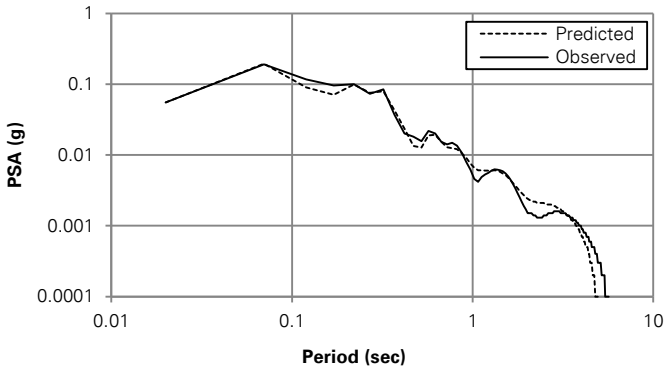

Fig. 6. 11 Observed and predicted response spectrum (ζ=0.05) for validation accelerogram Northridge-01(14) using adaptive windowing approach (NP2.3).

Figure 6.12 shows the spectrogram of the observed and predicted accelerograms. The spectrogram shows the distribution of the frequency content along the time axes. The spectrogram is calculated by the use of fast Fourier transformation (FFT) with the sliding

windowing method. The length of the FFT windowing is adjusted to 1.0 second with the overlapping ratio of 90%. It can be seen that the predicted accelerogram caries almost all dominant frequencies. Particularly, the dominant frequency range between 10 Hz and 15 Hz and the signal which caries the frequency higher than 20 Hz are predicted very well during the time. Nevertheless, the beginning of the lower frequency around 5 Hz is underestimated slightly. Accordingly, it can be concluded that frequency distribution along the time axes in predicted signal confirms a very well learning process.

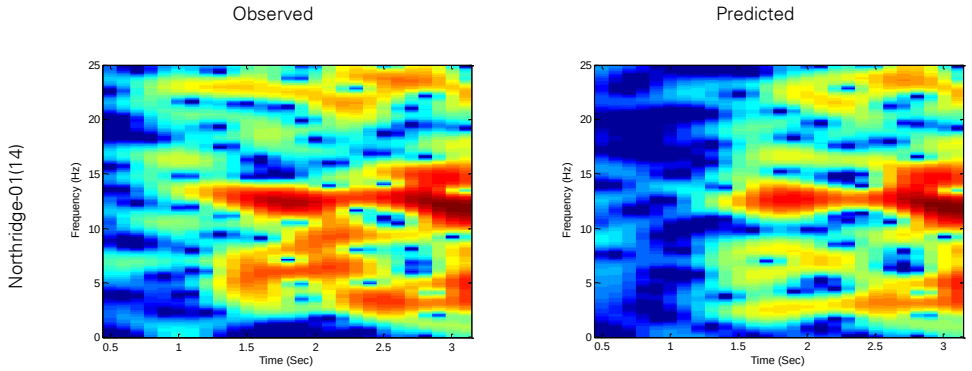

Fig. 6. 12 Spectrograms of the Observed and predicted accelerogram Northridge-01(14) (test dataset) using adaptive windowing approach (NP2.3)(Spectrogram specifications: Window length=1.0 sec, Overlap=90% and Frequency step=0.1 Hz).

The categorization aspects

To find out how the categorization affects the training process, the model has been trained by the use of several categorization aspects. In Table 6.2, the training process of the established model by the use of several categorizing aspects are compared. The average error values as well as the optimal training epochs are selected to represent the training efficiency. The last row of the table represents the error values which are obtained without any categorizing.

Comparison of the optimal training epochs between several groups shows that the categorizing based on the epicentral distance has the most scattered value than the other groups, namely 500 for middle and 100 for near distance categories. In the other words, the model which is trained with the near-field dataset was converged faster than the other models, although using the middle-field dataset leads to the slowest training process. It has to be noted that the number of optimal epochs refers only to the number of the learning iteration in which the neural network reaches the threshold error value and does not demonstrate the importance of every of the categorization criteria in seismology.

Table 6. 2 Average error value of the predicted accelerogram and response spectrum for test dataset using different categorizing approaches

	Optimal Epoch No.	Accelerograms	Response Spectra
Middle Distance	500	0.197	0.098
Near Distance	100	0.212	0.064
Strike-Slip	150	0.178	0.082
Reverse	200	0.205	0.094
Reverse-Oblique	200	0.163	0.070
Soil Type C	250	0.207	0.095
Soil Type B	250	0.164	0.080
Uncategorized	300	0.202	0.093

The error values are calculated by the use of the equation 6.1 and demonstrate the difference between the predicted and observed accelerogram. The results show that the minimum error values are achieved when the categorization based on the focal mechanism is undertaken. Furthermore, the average error of the spectrum of the predicted signal which shows the performance of the prediction in frequency domain agrees with the result obtained in time domain.

It can be concluded from Table 6.2 that the most uniform error distribution and the less training epochs were obtained by the use of the focal mechanism categorizing. The average error values between the observed and predicted accelerogram in the case of the novel testing dataset reach the minimum amounts if the focal mechanism categorization is carried out. On the other hand, the obtained results show that the model represents the worst performance when uncategorized dataset is applied.

Several windowing approaches

The average error values corresponding to the several windowing approaches are illustrated in Table 6.3. As it will be shown in the next paragraphs the performance of the model in the case of constant windowing approach (NP2.1) is strongly related to the non-stationary frequency content of the SGM signal, it means that the performance of the model which applies constant windowing is related to the length of the sampling windows.

Table 6. 3 Average error value of predicted accelerograms and response spectra for test dataset using different windowing approaches (after 200th epochs of training)

Windowing	Accelerograms	R. Spectra
Constant Δt=0.2 [sec]	0.0227	0.2296
Constant Δt=0.35 [sec]	0.0308	0.1831
Constant Δt=0.5 [sec]	0.0197	0.1388
Semi-adaptive	0.0338	0.1318
Adaptive	0.0122	0.0981

Nevertheless, surveying the average error values shows that the networks which apply the constant windowing approach (NP2.1) in general have the higher average error value than the networks which work with frequency adaptive windowing approach. The obtained error values show that the model applies the semi-adaptive approach could not perform an acceptable prediction in time domain.

Figure 6.13 represents the performance of the trained network on Northridge-01(10) using the test data set by the use of several windowing approaches. Comparison of the observed and predicted accelerograms indicates that the performance of the trained RBF neural network is strongly affected by the used windowing approach. The predictions obtained applying the constant windowing approach (NP2.1) show that the windows length of 0.2 sec leads to the closest results to the observed data especially for the higher frequency parts of the signal. This effect can be interpreted according the dominant frequency of the data which is approximately equal to 5 Hz (1/5= 0.2 sec) during the entire phase (see Figure 6.14). Nevertheless, the amplitude of the predicted signal in this case is generally lower than the observed signal. However, using the windows longer than 0.2 sec leads to catch the lower frequency parts of the signal, for instance by the use of the window 0.5 sec the long period signal between 3.3 and 4.0 can be predicted very well.

The predicted accelerogram by the use of the adaptive windowing approach (NP2.3) shows the best performance among the several windowing approaches. Figure 6.13 shows that predicted accelerogram using the model NP2.3 can follow very well the original signal properties. Nevertheless, at the beginning (between 0.7 sec and 1.2 sec) and at the middle of the phase (between 2.0 and 3.0 sec) the amplitude of the predicted accelerogram is lower than the observed data in spite of the rather acceptable frequency content of the prediction. The response spectrum of the predicted accelerogram shows a very well adaptability during dominant period.

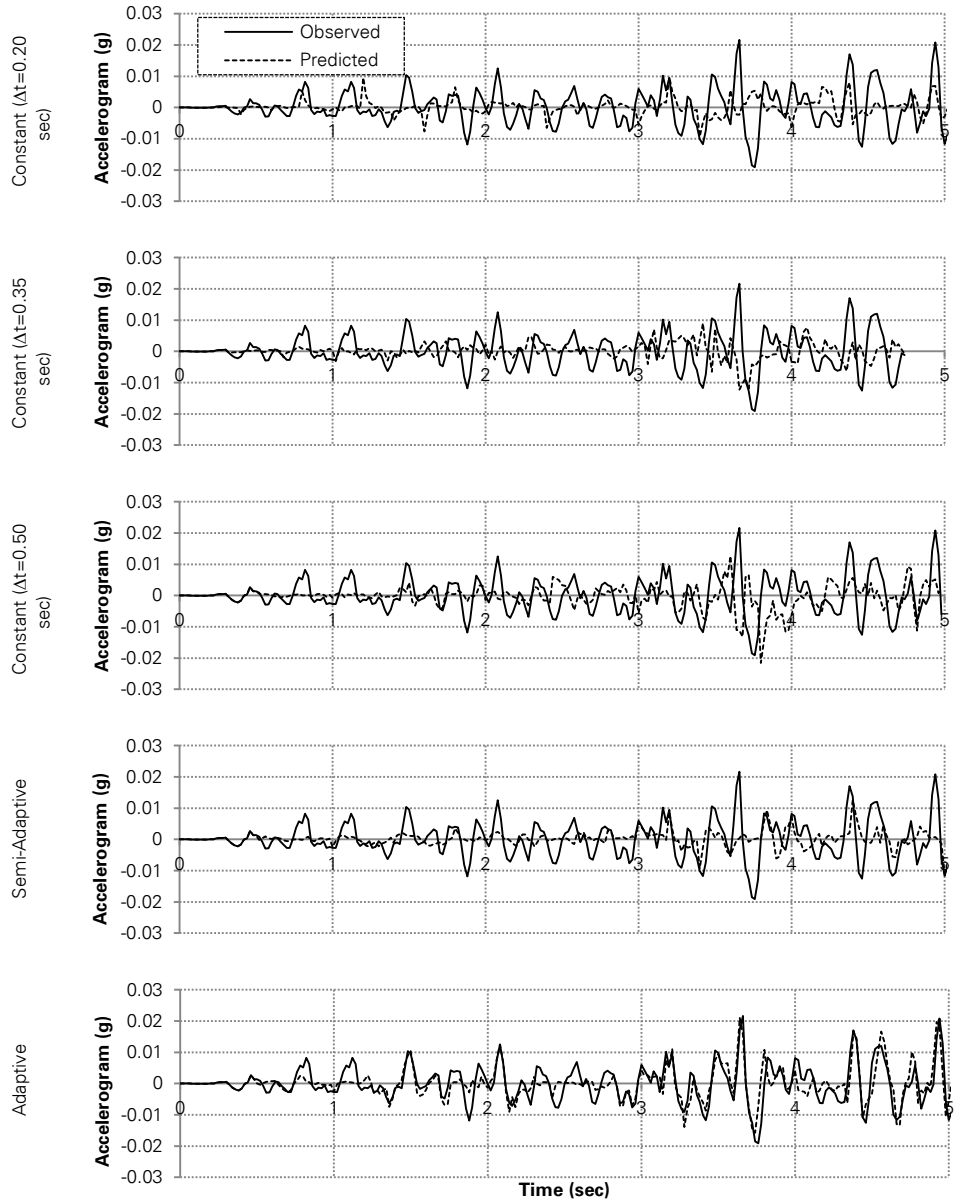

Fig. 6. 13 Observed and predicted accelerogram for validation accelerogram record Northridge-01(10) using several windowing approaches.

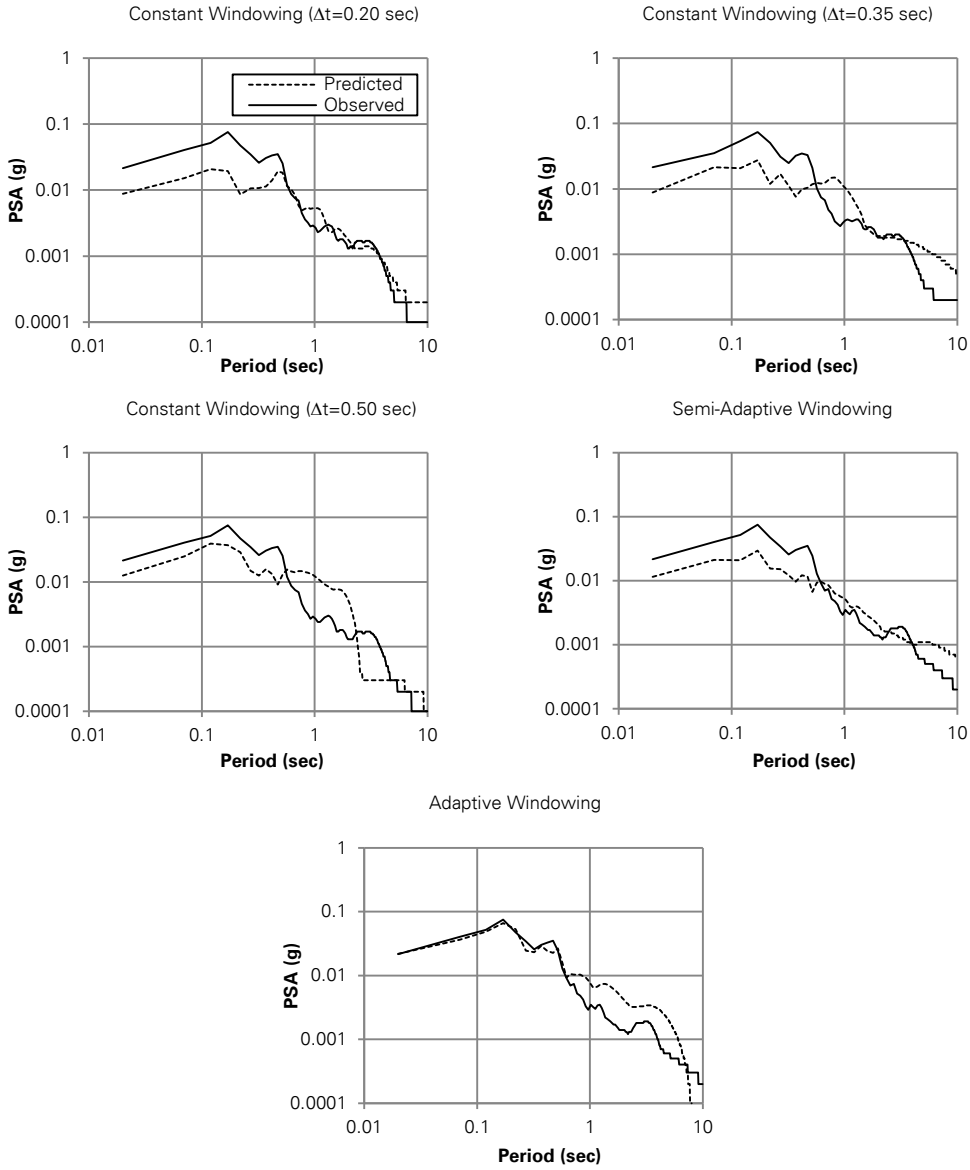

Fig. 6. 14 Observed and predicted response spectrum (ζ=0.05) for validation accelerogram record Northridge-01(10) using several windowing approaches.

Figure 6.15 shows the spectrograms of the observed and the predicted accelerograms Northridge-01(10) from the test data set by the use of several windowing approaches. As it was shown earlier, using the constant windowing of 0.2 sec shows the best compatibility between observed and predicted accelerograms among several constant windows which is related to the dominant frequency of the test accelerogram. The best frequency distribution along time is obtained by the use of the adaptive windowing approach. In this case the predicted accelerogram follows the pattern of dominant frequencies in the observed accelerogram very well.

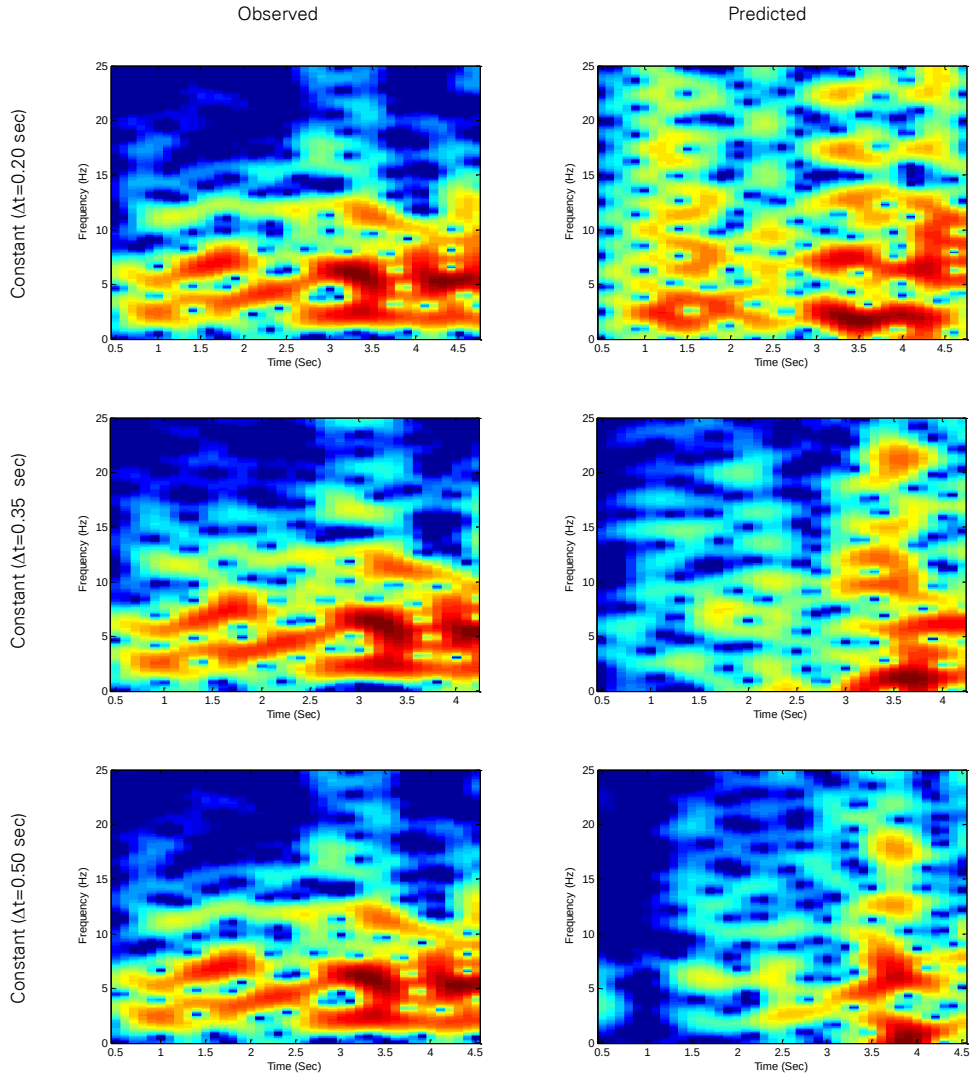

Fig. 6. 15 Observed and predicted spectrogram for testing accelerogram record Northridge-01(10) using several windowing approaches (Spectrogram specifications: Window length=1 sec, Overlap=90% and Frequency step=0.1 Hz).

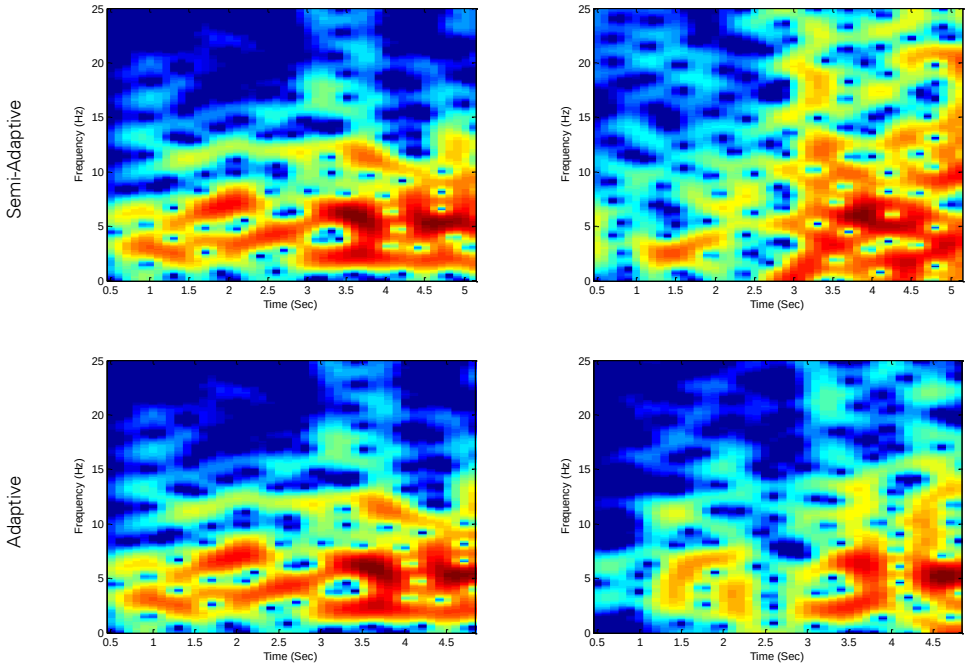

Fig. 6. 15 Observed and predicted spectrogram for testing accelerogram record Northridge-01(10) using several windowing approaches (Spectrogram specifications: Window length=1 sec, Overlap=90% and Frequency step=0.1 Hz) (Continued).

Performance of the trained network

The sample accelerograms shown in Figure 6.16 demonstrate the performance of the trained non-parametric evolutionary model (NP2) on six accelerograms from the test datasets. It has been tried to collect those accelerograms which are not identical neither in time nor in frequency domain. It can be seen that the collected accelerograms having a wide range of PGA. The NP2 model is trained by the use of the datasets which are categorized based on the faulting mechanism. The response spectra and the spectrograms of the predicted and observed accelerograms are illustrated in Figures 6.17 and 6.18 respectively.

Comparison between the predicted and observed accelerograms of Northridge-01(10) shows that the model can predict almost all the pick values. Nevertheless, the amplitude of the peaks around 1.0 and 2.5 sec are underestimated. The response spectra of the predicted and observed accelerograms which are shown in Figure 6.17 show that the response spectra around the dominant period (approximately 0.2 sec) is predicted very well. However, in the higher period range (> 0.5 sec) the predicted response spectrum shows lower values than the response spectrum of the observed signal. The spectrogram (right side of Figure 6.18) of the predicted accelerogram shows a good performance of the predictor in frequency domain in general. It can also be seen that around 2.5 sec the non-stationary frequency content of the Northridge-01(10) could not be modeled properly.

The predicted accelerogram of Chi-Chi-03 (46) seems not so acceptable between 2.0 and 3.3 sec in time domain. There are some peaks in which the amplitude values are under estimated. However, after 3.3 sec the predicted accelerogram is matched very well to the observed one in both time and frequency domains. It is also remarkable that the frequency distribution along the time is predicted very well (Figure 6.18). As it is obvious in Figure 6.17 the response spectrum of the predicted accelerogram matches to the original signal during the whole period range.

One of the best predictions can be seen during the Chi-Chi-05 (75). The original accelerogram like the white noise spreads in a wide frequency range (Figure 6.18). The spectrogram of the predicted signal is strogly compatible to the observed signal. It can be seen that the dominant period around 0.05 sec is predicted very well in the response epectrum (Figure 6.17) of the predicted accelerogram. Except in the high frequency area The accelerogram of Chi-Chi-06 (84) seem very similar to Chi-Chi-05 (75). The frequency range is predicted properly during the response spectrum and the spectrogram. Nevertheless, the underestimation of the amplitude between 5.0 and 6.0 sec is noticeable.

As it is shown in Figure 6.16 the predicted accelerogram of Chi-Chi-06 (85) accents an acceptable performance of the predictor in time domain. Almost all peak values are predicted properly among the whole of the signal. The rather flat response spectra of the signal which is spread between the periods 0.1 and 1 could be predicted properly. Comparing the spectrogram of the predicted and observed accelerograms (see Figure 6.18) shows an excellent performance of the predictor in frequency domain.

The predicted accelerogram of Chi-Chi-06 (86) shown in 6.16 shown a good prediction of the amplitude after 2.0 sec. The amplitude of the accelerogram between 1.4 and 2.0 was underestimated. Response spectrum and spectrogram of the predicted accelerogram match very well to the observed signal. Especially, the spectrogram shows (Figure 6.18) that the low dominant frequencies around 2.0 Hz were modeled perfectly.

Generally, it can be concluded that comparison between the spectrograms shown in Figure 6.18 indicates that the non-stationarity of the SGM process is reflected very well in the majority of the predicted accelerograms. The predictor shows an acceptable performance in real-time prediction of accelerograms which contain wide range of frequencies like Chi-Chi-05 (75) as well as which are spread in a narrow frequency range like Chi-Chi-06 (86). However, it was seen that in some cases the amplitude of the predicted accelerogram were underestimated.

Fig. 6. 16 Observed and predicted accelerograms obtained by applying the adaptive windowing approach.

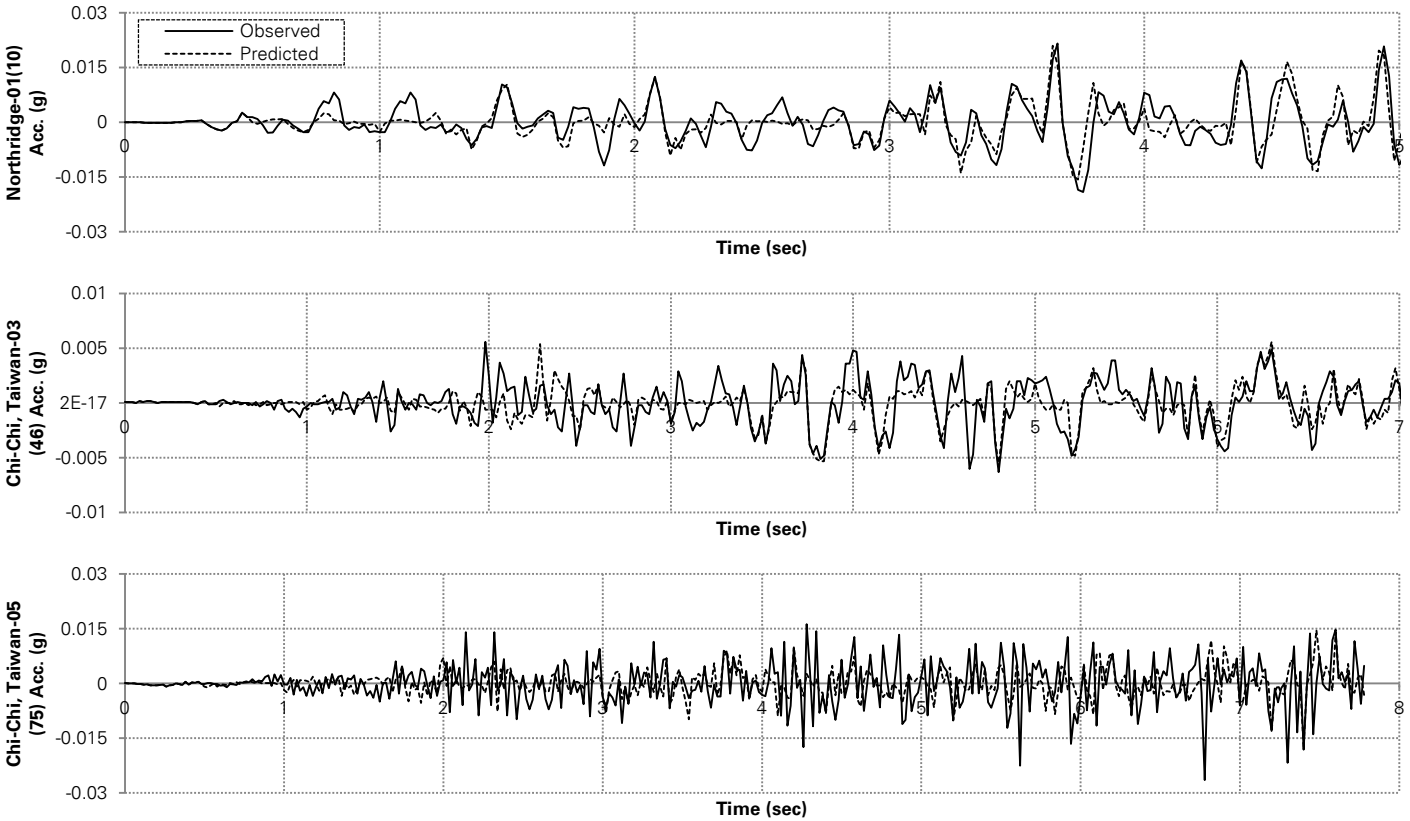

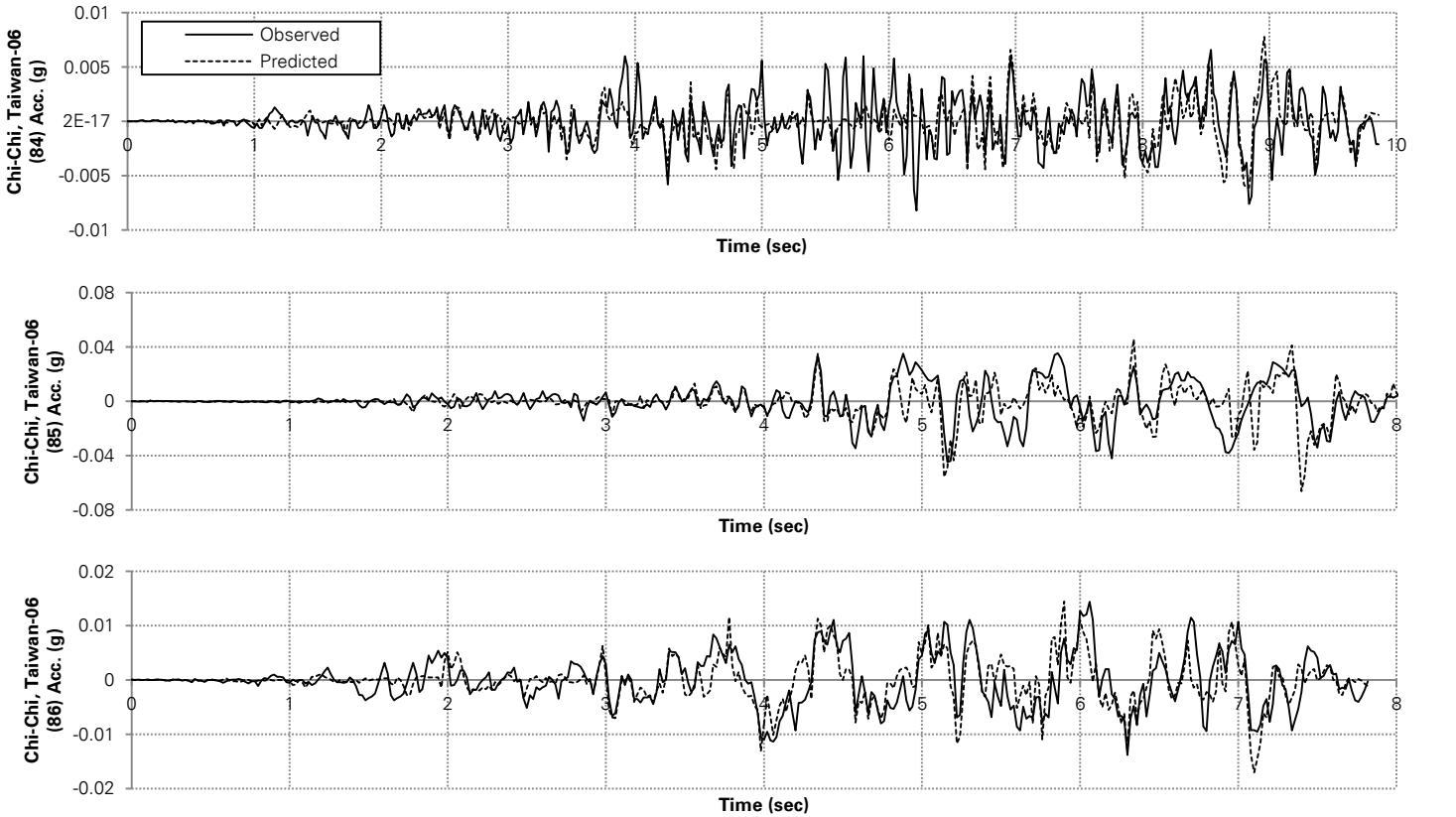

Fig. 6. 16 Observed and predicted accelerograms obtained by applying the adaptive windowing approach (Continued).

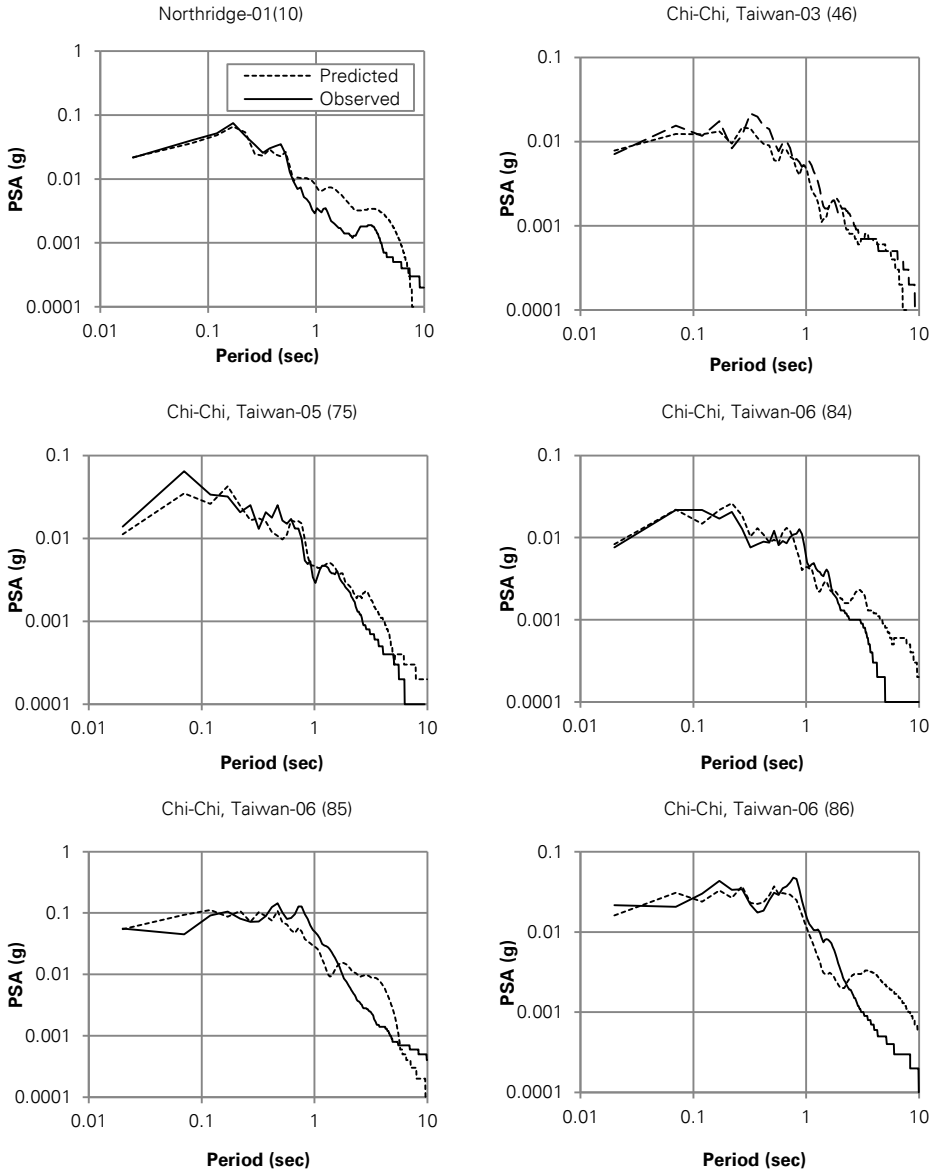

Fig. 6. 17 Response spectra of observed and predicted accelerograms (ζ=0.05) obtained by applying the adaptive windowing approach.

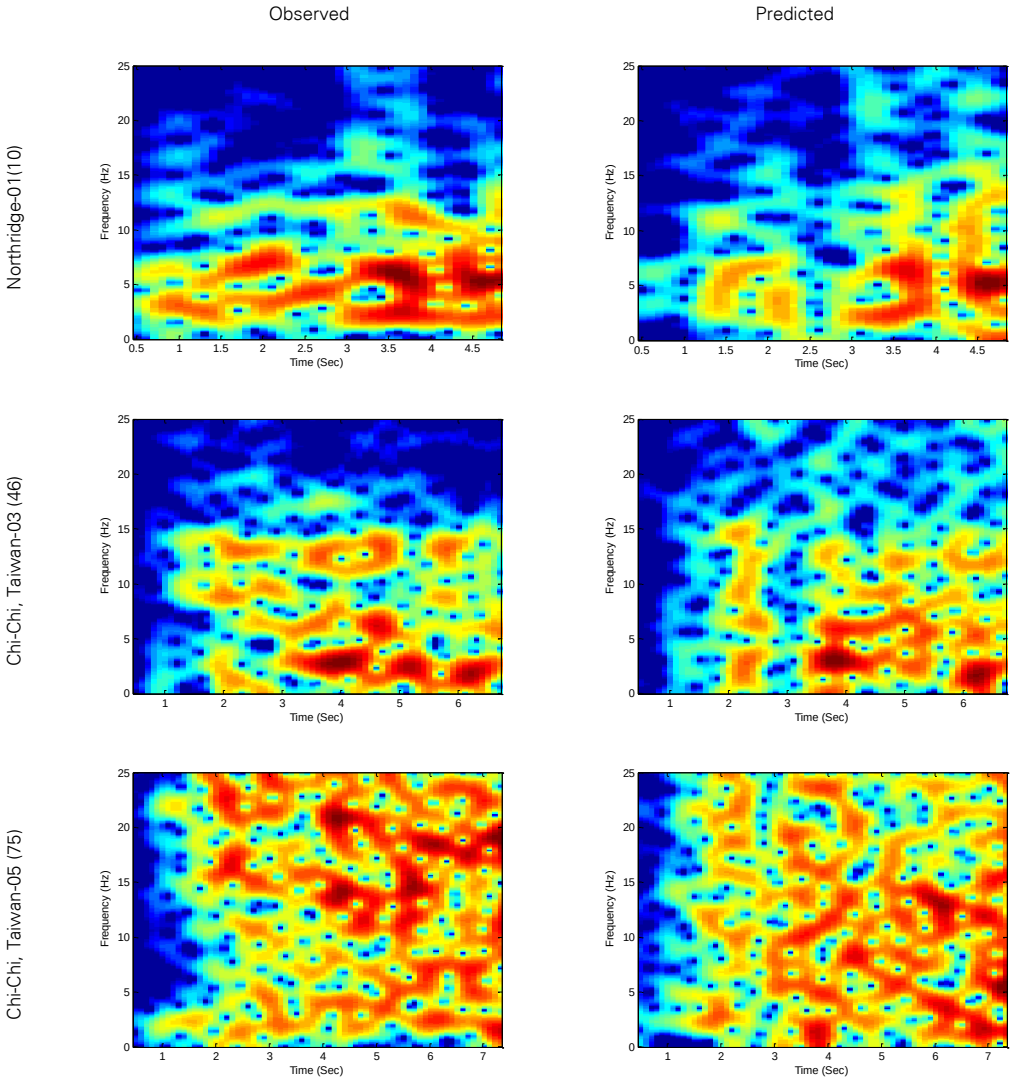

Fig. 6. 18 Observed and predicted spectrogram for testing accelerogram data set using adaptive windowing approach (Spectrogram specifications: Window length=1 sec, Overlap=90% and Frequency step=0.1 Hz).

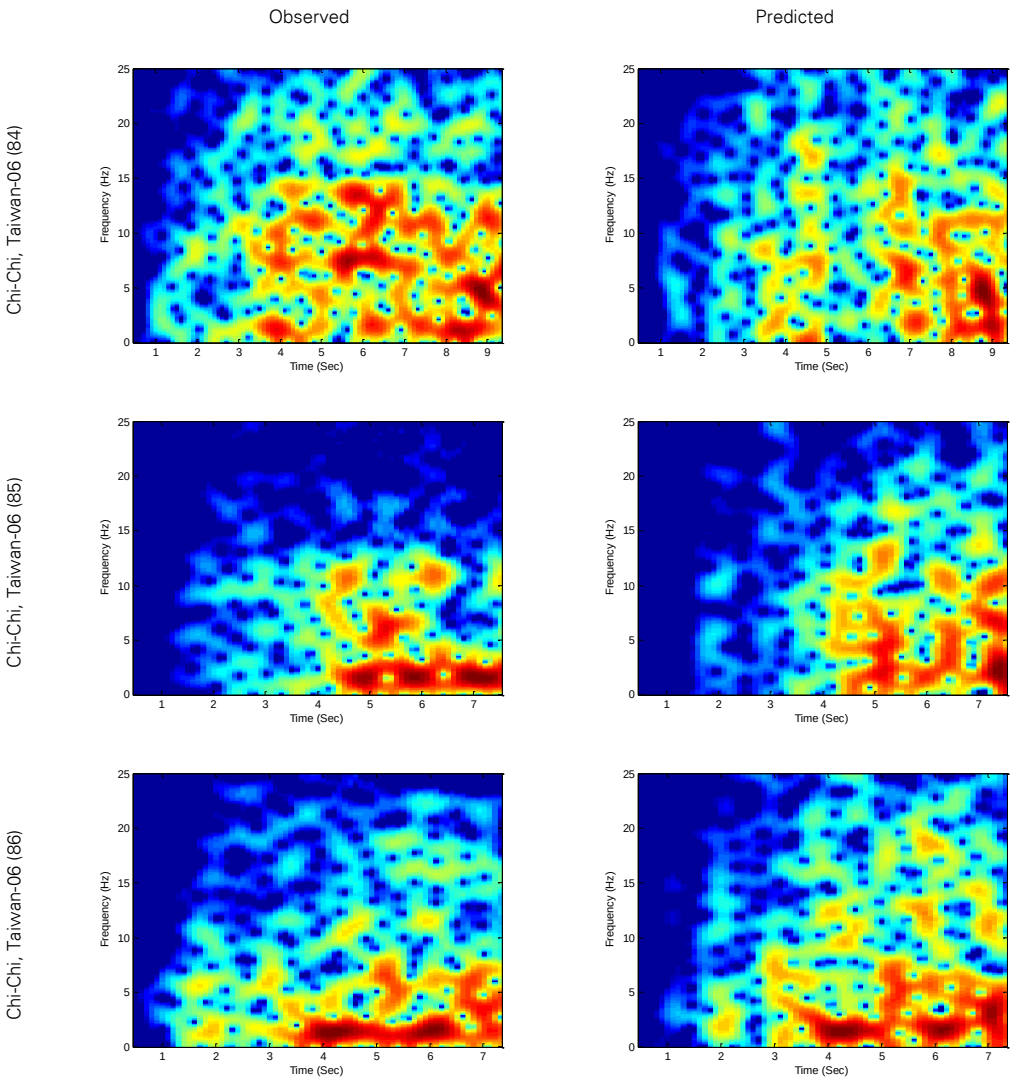

Fig. 6. 18 Observed and predicted spectrogram for testing accelerogram data set using adaptive windowing approach (Spectrogram specifications: Window length=1 sec, Overlap=90% and Frequency step=0.1 Hz) (Continued).

6.2 APPLICATION OF THE STOCHASTIC REAL-TIME MODEL

6.2.1. Database

To apply the stochastic real-time prediction model local SGM records of the main-shock of Northridge 1994 (M_w=6.69) have been used. As it is mentioned in the developed wave-type based stochastic predictor the parameters of spectral model are extracted during the application while the amplitude envelope is predicted by the use of a pre-trained model. Since the evolutionary envelope predictor is very sensible to the database, it is preferred to use the database which is recorded during the same earthquake. Therefore, 109 well recorded SGM free-field records (altogether 327 orthogonal components) from PEER NGA database are collected (see Table A.3 in Appendixes A).

The PGA values of the collected SGM database are ranging from 0.05 g to 1.66 g while the maximum value is recorded in epicentral distance of 5.41 km. The maximum epicentral distance is limited for the middle-filed station located of 85.72 km far from the seismic source. The shear wave velocities of the local recording stations are ranging from 160.58 m/s in Corson-Waterst. station and 996 m/s in Vasquez Rocks Park station (the database covers all EC8 soil conditions). All the accelerograms were resampled at 0.02 sec in order to synchronize the SGM records having different sample rates to be used by training of the amplitude evolutionary model.

6.2.2. Verification of the Stochastic Real-Time Prediction Model

As it was described in chapter 5, a wave-typed base stochastic model for real-time prediction of strong ground motion signal is developed. For this purpose, an approach based on fitting a parameterized stochastic model to real-time recorded ground motion is developed to model the frequency content of SGM and a soft-computing based method is developed to model the amplitude envelope function in evolutionary manner. It is necessary to properly model both spectral and temporal non-stationary, particularly for inelastic and degrading structures, which tend to consider the resonant frequencies that also evolve in time.

The developed non-stationary stochastic model contains a real-time time-modulating function called evolutionary amplitude envelope predictor. In this section, application of the envelope predictor by the use of a sample SGM record is explained. The effectiveness of the model for several seismic phases will be discussed after that. Using the filtered Gaussian white-noise, the frequency content of SGM is modeled in which according to the spectral characteristics of the current time window the parameters of the filter is estimated continuously during the time. Using developed approach several real-time stochastic predictions are conducted, which will be evaluated in both time- and frequency-domain in this section as well. Finally, in order to evaluate the energy distribution of the predicted SGM accelerograms during the time cumulative Arias intensity of the predictions are compared with the observed data for dominant P and S-Coda waves separately.

Real-time evolutionary amplitude envelope model

Evolutionary prediction of amplitude envelope function during consecutive prediction steps for dominant seismic waves P and S-Coda are illustrated in Figures 6.19 and 6.20, respectively. As it was described in chapter 5, the evolutionary amplitude envelope predictor performs the form estimation by the use of real-time measured signal in cumulative order. The results obtained from the predictor are fitted to the wave-type based envelope functions to extract the curve parameters (the solid curves in Figures 6.19 and 6.20). During the pre- and post-processing of the input and outputs signals, which is performed by the use of the reversible fast Fourier transformation (see section 4.3), it is seen that the ending part of the target signal (grey curves in Figure 6.19 and 6.20) was manipulated by this transformation. Despite this manipulation, since the predicted curve (the dotted curves in Figures 6.19 and 6.20) will be fitted to the predefined envelope functions, the results will not be affected (the solid curves in Figures 6.19 and 6.20).

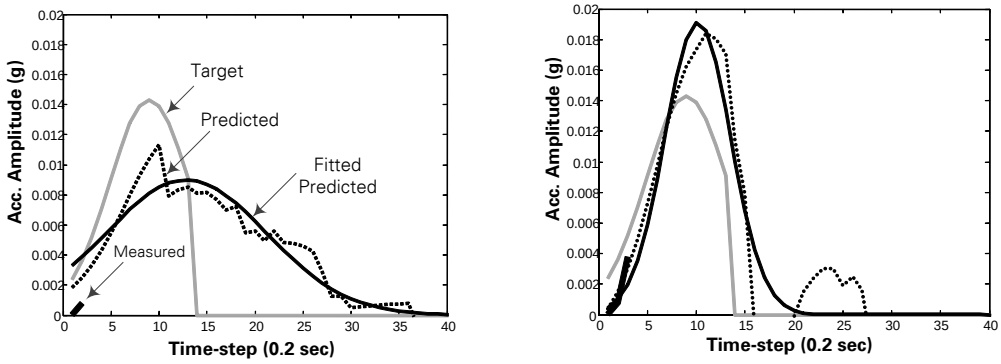

Step 1 (0-0.5 sec) Step 2 (0-0.7 sec)

Fig. 6. 19 Evolutionary envelope function for dominant P wave. The grey, dotted, solid and bold curves represent the target, predicted, and fitted predicted and real-time measured envelope functions, respectively.

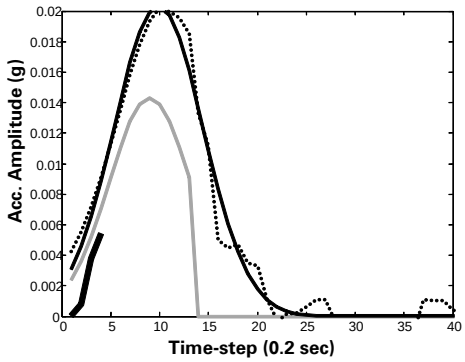

Step 3 (0-0.9 sec)

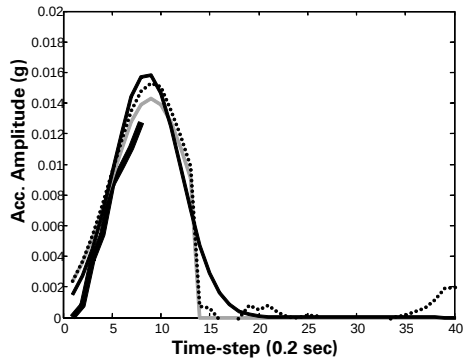

Step 4 (0-1.1 sec)

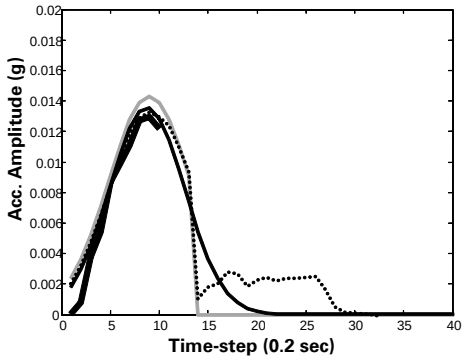

Step 5 (0-1.9 sec)

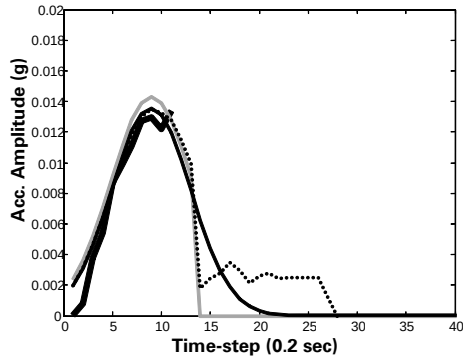

Step 6 (0-2.4 sec)

Fig. 6.19 Evolutionary envelope function for dominant P wave. The grey, dotted, solid and bold curves represent the target, predicted, and fitted predicted and real-time measured envelope functions, respectively (Continued).

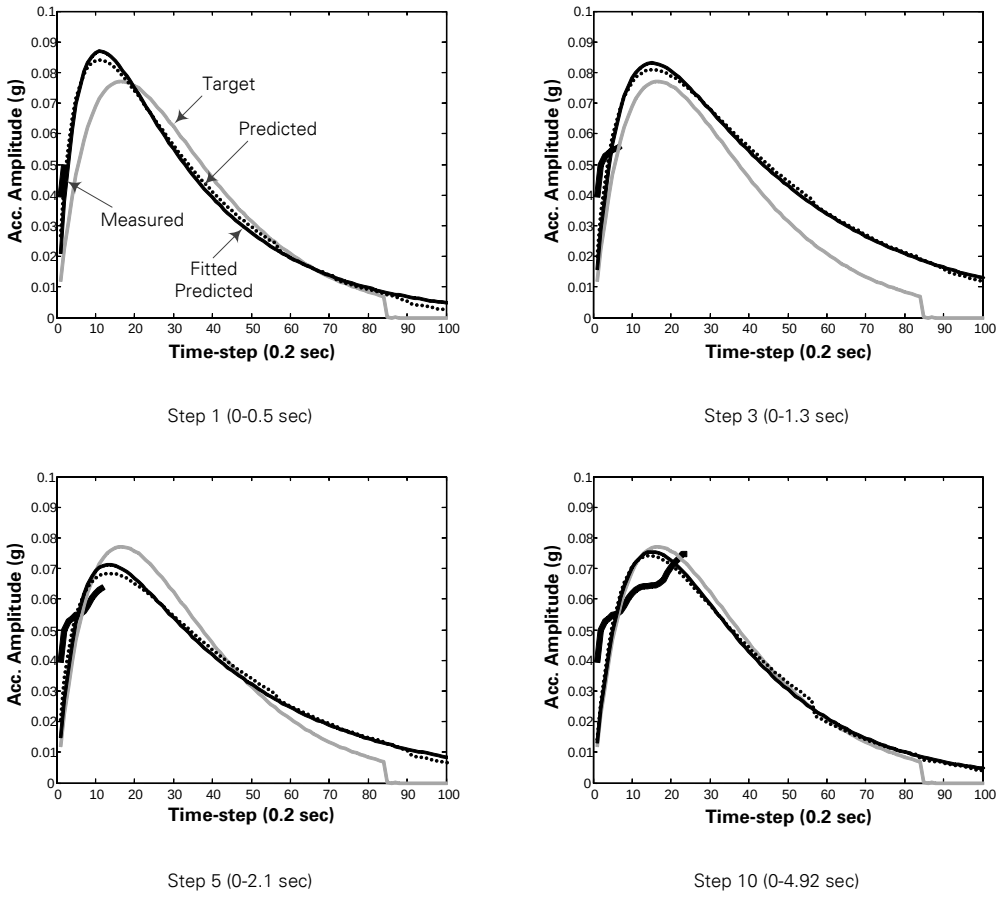

Fig. 6. 20 Evolutionary envelope function for dominant S-Coda waves. The grey, dotted, solid and bold curves represent the target, predicted, and fitted predicted and real-time measured envelope functions, respectively.

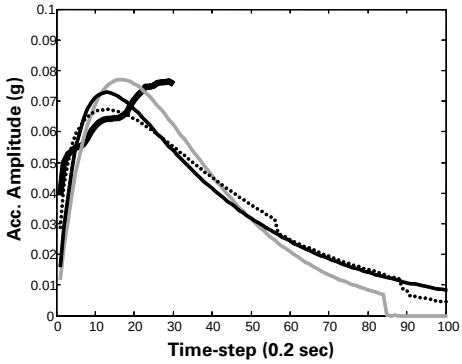

Step 12 (0-6.2 sec)

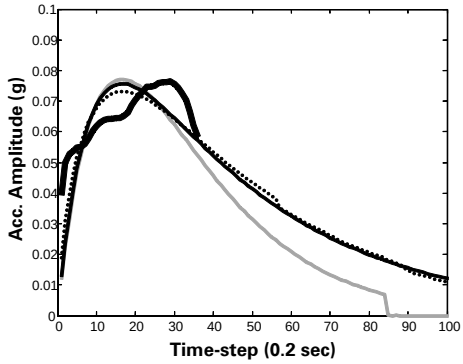

Step 13 (0-6.6 sec)

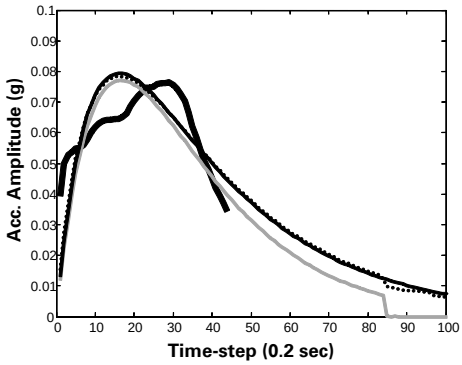

Step 15 (0-7.88 sec)

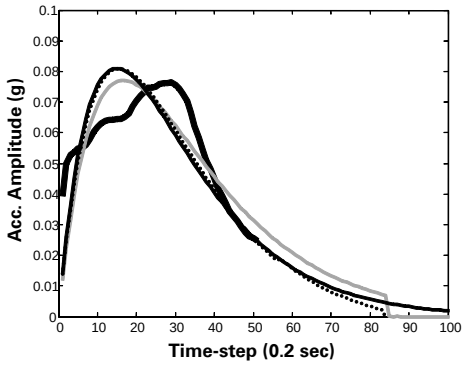

Step 17 (0-9.16 sec)

Fig. 6.20 Evolutionary envelope function for dominant S-Coda waves. The grey, dotted, solid and bold curves represent the target, predicted, and fitted predicted and real-time measured envelope functions, respectively (Continued).

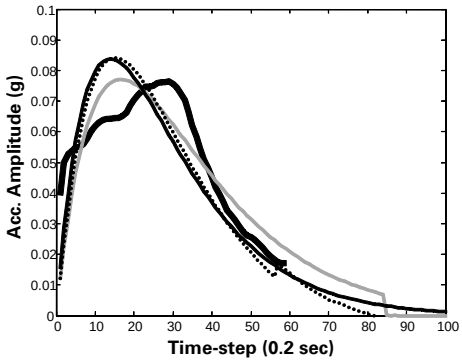

Step 20 (0-11.64 sec)

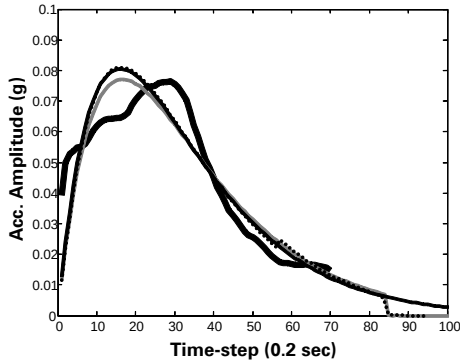

Step 23 (0-13.56 sec)

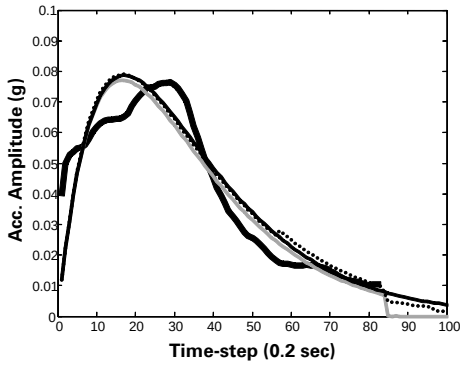

Step 26 (0-15.8 sec)

Fig. 6.20 Evolutionary envelope function for dominant S-Coda waves. The grey, dotted, solid and bold curves represent the target, predicted, and fitted predicted and real-time measured envelope functions, respectively (Continued).

The resulted curves obtained from the dominant P-wave envelope predictor show that the model has underestimated the envelope during the first trail. In the following prediction steps from 0.0-0.7 sec and 0.0-0.9 sec the predicted envelope is higher than the observed signal. Starting with the fourth step (0.0-1.1 sec) the obtaining results seem very close to the real signal. The resulted curves obtained from the dominant S-Coda wave envelope predictor show that the model can find the target envelope function from the early trail steps except the overestimation during 0.0-0.5 sec and 0.0-1.3 sec and underestimation during 0.0-2.1 sec. The following prediction steps show a rather good similarity between the predicted and observed envelope functions. Furthermore, the results show that the predicted envelope functions during dominant seismic waves of S-Coda represent more stability than the model of dominant P-wave. It is also notable that the developed prediction models are able to find correctly the position of the peak value.

The frequency content of the predicted strong ground motions

In order to evaluate the prediction efficiency of the developed stochastic real-time prediction model in frequency content, the results obtained by the application of the prediction model for Northridge 1994, LA- Chalon Rd are presented in this section. It is noteworthy that this SGM is recorded at a station 14.92 km far away from the epicenter of the main shock and above the soil type B according to Eurocode 8. Since the output of the stochastic prediction models are not deterministic and to evaluate the independency of the predictions to the basic random noise, four different trails of prediction are shown in this section.

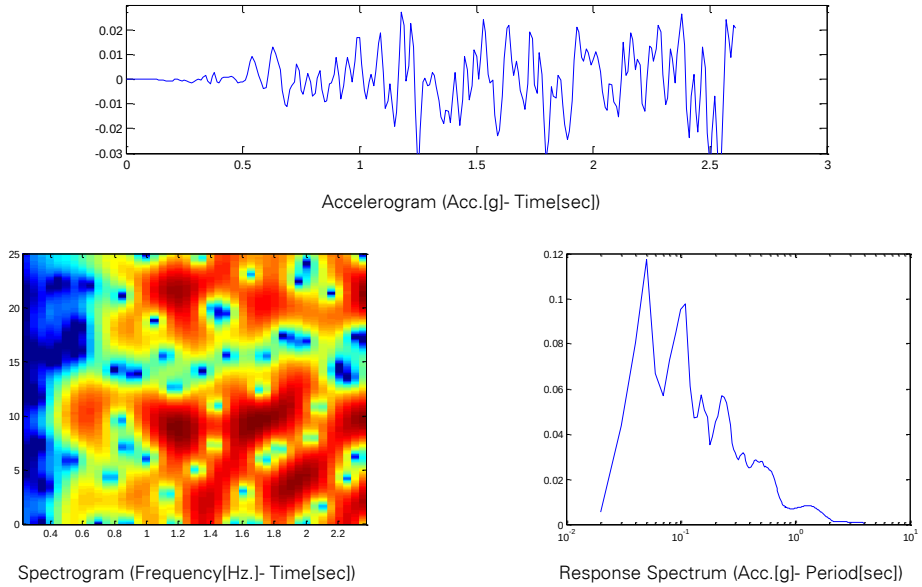

Fig. 6. 21 Observed strong ground motion accelerogram (top), spectrogram (button left) and response spectrum (button right) of dominant P-wave of Northridge 1994 recorded at LA - Chalon Rd.

The observed SGM time history as well as corresponding spectrogram and response spectrum for dominant seismic wave P and S-Coda are illustrated in Figure 6.21 and Figure 6.26, respectively. As it is shown in Figure 6.21, the frequency pattern of the sample SGM during dominant seismic P wave remains almost constant.

Two major trends can be detected in frequency distribution along the time; one is the high frequency area in almost 20 Hz and the other is the wide area, which is formed between frequency 4 Hz and 10 Hz. Despite the developed frequency model, applies several frequency models for consecutive time windows but it seems reasonable to use a single PSD for dominant P-wave. Similarly, the response spectra of the sample SGM shows two distinguish peaks in period of 0.05 and 0.1 seconds.

The prediction results are shown in Figures 6.22 to 6.25. They show that the predicted accelerogram could follow very well the amplitude envelope of the sample data as well as the peak values (The zero values in the beginning of the predicted signal denotes that no prediction is conducted in the first 0.5 sec of the signal). Evaluation of the spectrogram, which represents the distribution of frequency content along the time, shows a rather well prediction of the higher dominant frequency. Although the model has predicted the lower dominant frequency, the intensity of lower frequency seems to be underestimated, especially in samples 3 and 4 (Figures 6.24 and 6.25).

Response spectra of the predicted accelerograms (damping ratio: 5%) show that spectral response of the predicted SGM in lower period are modeled very well in spite of the underestimation of higher period response in most of the predictions (2,3 and 4).

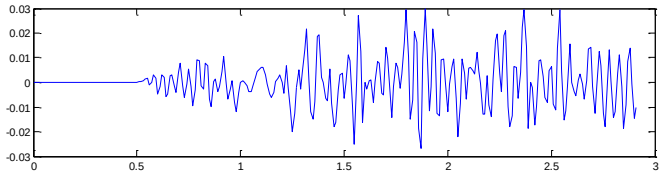

Accelerogram (Acc.[g]- Time[sec])

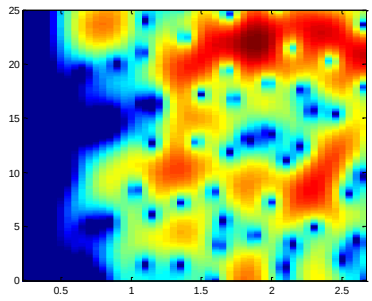

Spectrogram (Frequency[Hz.]- Time[sec])

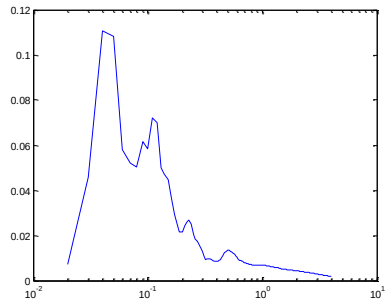

Response Spectrum (Acc.[g]- Period[sec])

Fig. 6. 22 Prediction #1 strong ground motion accelerogram (top), spectrogram (button left) and response spectrum (button right) of dominant P-wave of Northridge 1994 recorded at LA - Chalon Rd.

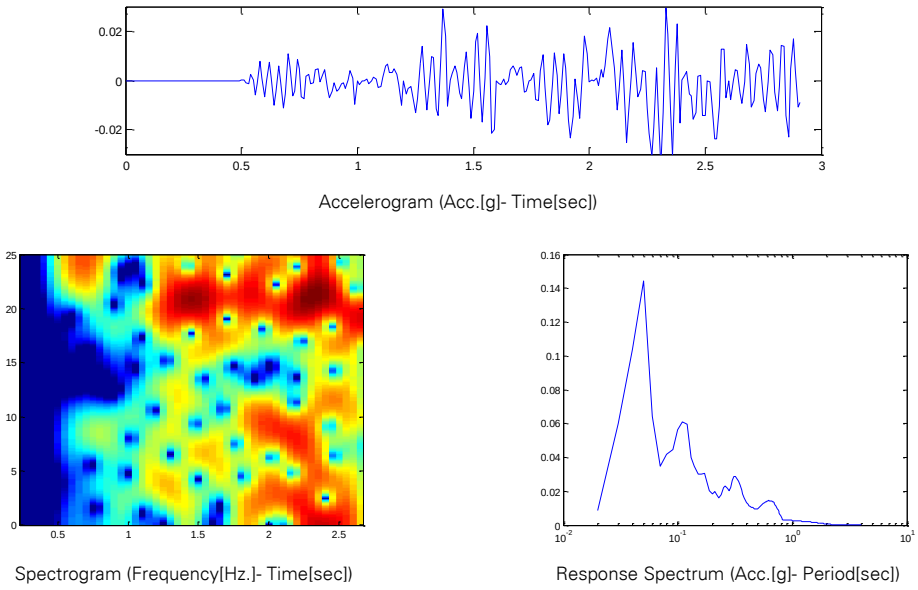

Fig. 6. 23 Prediction #2 strong ground motion accelerogram (top), spectrogram (button left) and response spectrum (button right) of dominant P-wave of Northridge 1994 recorded at LA - Chalon Rd.

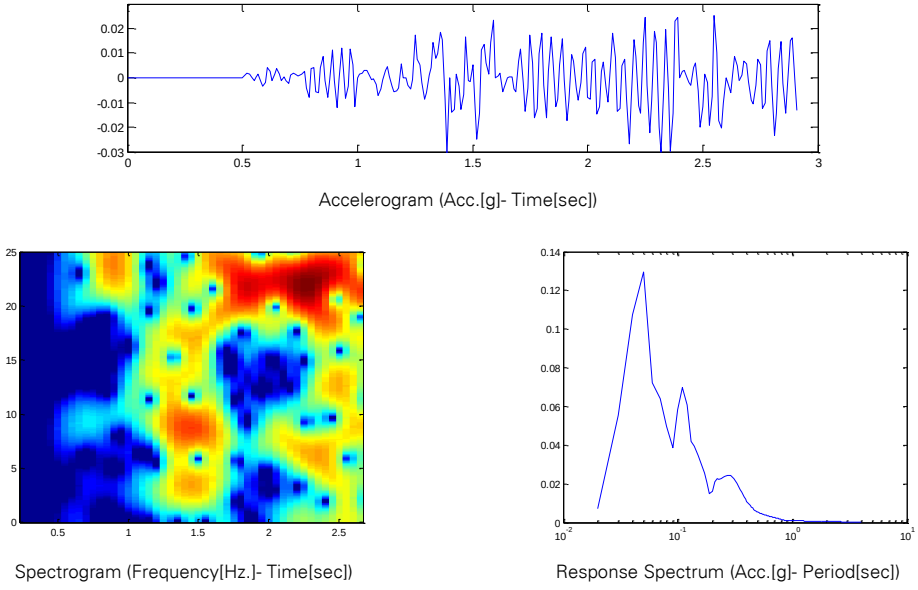

Fig. 6. 24 Prediction #3 strong ground motion accelerogram (top), spectrogram (button left) and response spectrum (button right) of dominant P-wave of Northridge 1994 recorded at LA - Chalon Rd.

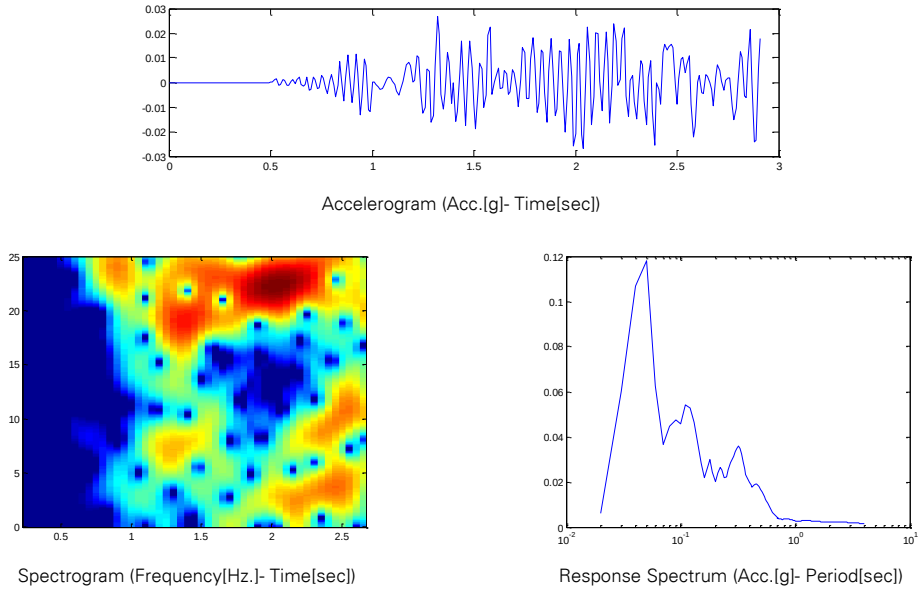

Fig. 6. 25 Prediction #4 strong ground motion accelerogram (top), spectrogram (button left) and response spectrum (button right) of dominant P-wave of Northridge 1994 recorded at LA - Chalon Rd.

In Figure 6.26 accelerogram, spectrogram and response spectra of dominant S-Coda waves are shown. As it is expected, the frequency content is extremely lower than for the dominant P-wave. Unlike the P-wave the frequency pattern of the sample SGM during dominant seismic S-Coda waves does not follow a constant pattern. Three major trends can be detected in frequency distribution along the time; one is the lower frequency area in almost early 5 second, the second one is the higher and wider frequency content from 5 to the 7 second and the last one is the rest lower frequency content. Response spectra of the sample SGM shows two peak areas in period of 0.2 and 0.45 seconds for dominant S-Coda waves.

The prediction results are shown in Figures 6.27 to 6.30. Similarly to the amplitude envelope prediction of dominant P-wave the predicted accelerogram could follow very well the amplitude envelope of the sample data as well as the peak values (The zero values in the beginning of the predicted signal denotes that no prediction is conducted in the first 0.5 sec of the signal) . Evaluation of the spectrogram shows a rather well prediction of the dominant frequencies in second and third part of the accelerogram but the early low frequency signal (first part of the signal), could not simulate correctly. Response spectra of the predicted accelerograms (damping ratio: 5%) show that spectral response of the predicted SGM in higher period are modeled very well in spite of the overestimation of higher period response in almost all predictions.

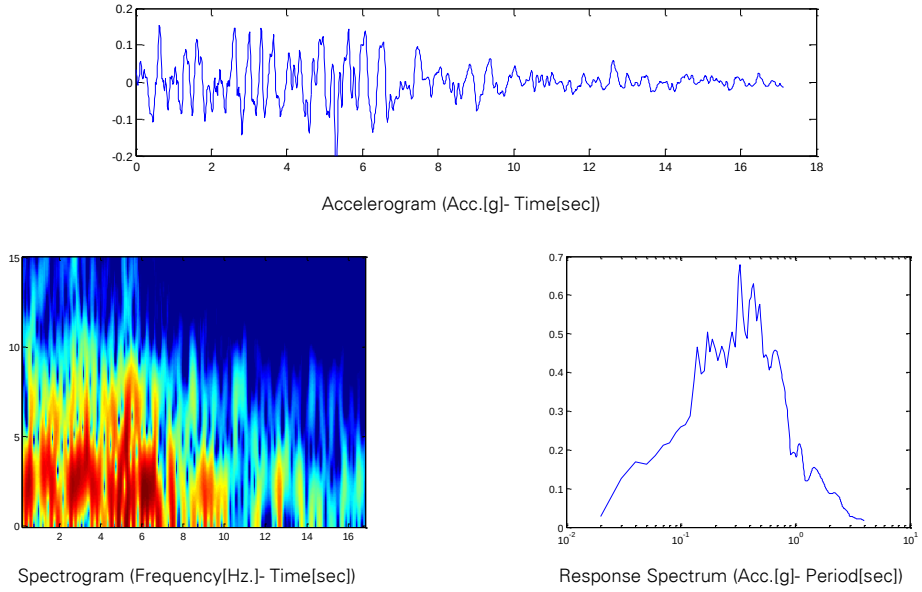

Fig. 6. 26 Prediction #4 strong ground motion accelerogram (top), spectrogram (button left) and response spectrum (button right) of dominant P-wave of Northridge 1994 recorded at LA - Chalon Rd.

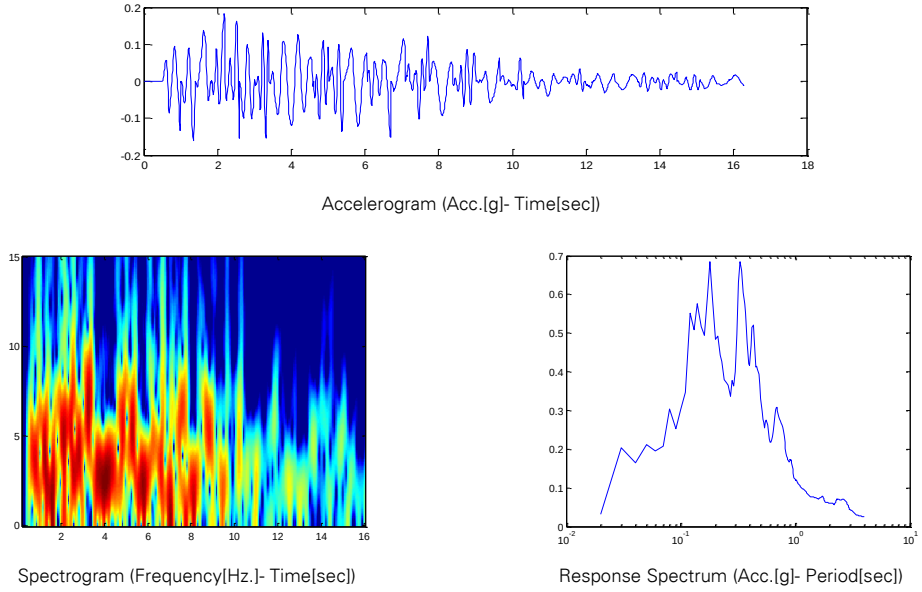

Fig. 6. 27 Prediction #1 strong ground motion accelerogram (top), spectrogram (button left) and response spectrum (button right) of dominant S-Coda wave of Northridge 1994 recorded at LA - Chalon Rd.

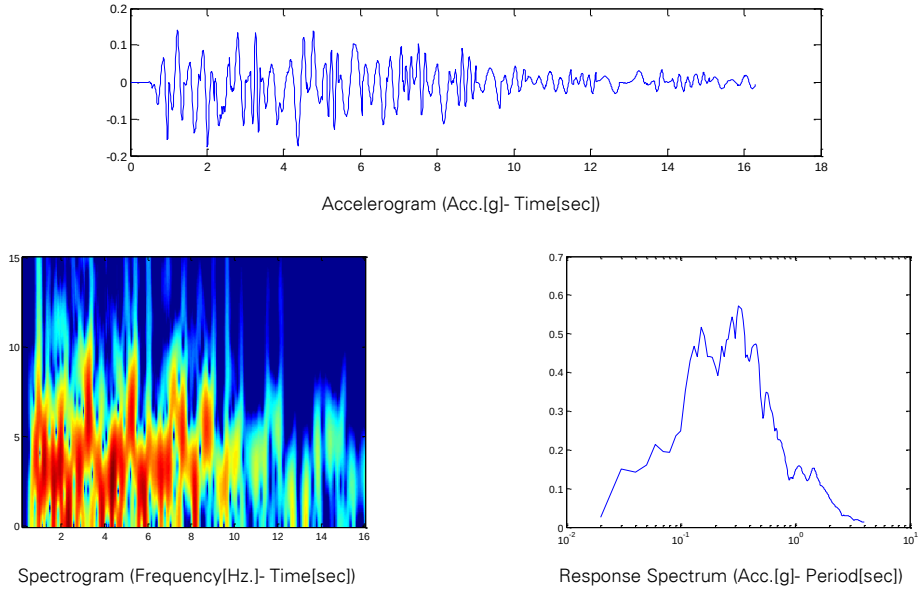

Fig. 6. 28 Prediction #2 strong ground motion accelerogram (top), spectrogram (button left) and response spectrum (button right) of dominant S-Coda wave of Northridge 1994 recorded at LA - Chalon Rd.

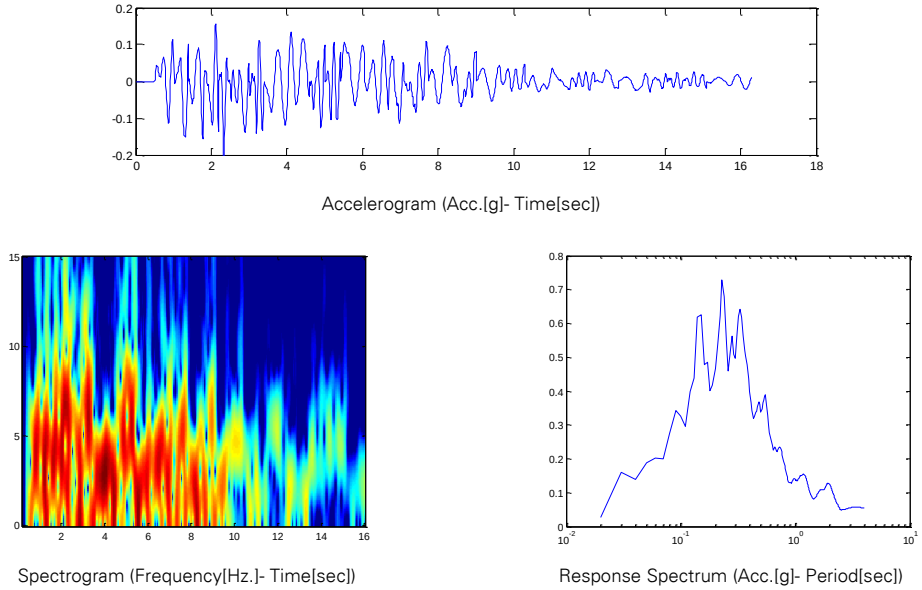

Fig. 6. 29 Prediction #3 strong ground motion accelerogram (top), spectrogram (button left) and response spectrum (button right) of dominant S-Coda wave of Northridge 1994 recorded at LA - Chalon Rd.

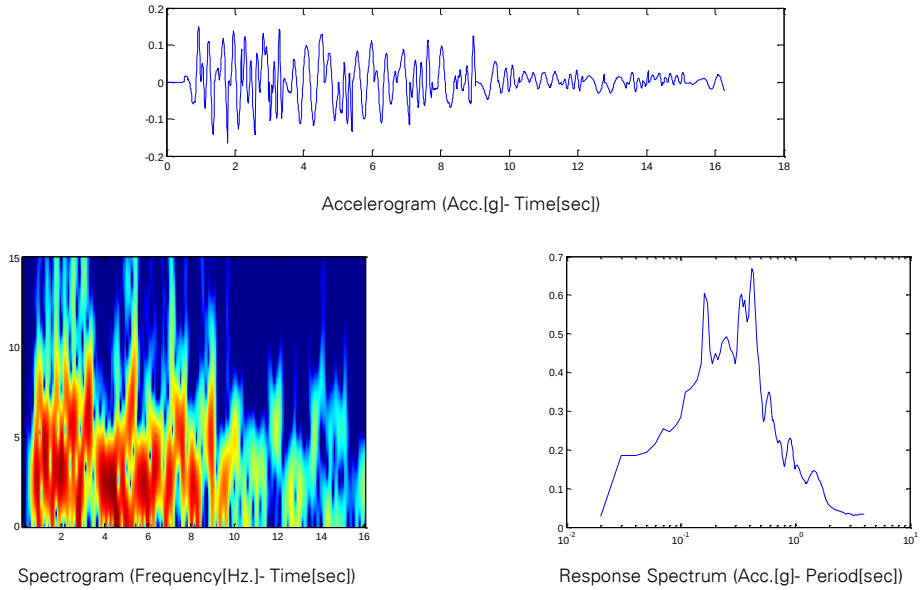

Fig. 6. 30 Prediction #4 strong ground motion accelerogram (top), spectrogram (button left) and response spectrum (button right) of dominant S-Coda wave of Northridge 1994 recorded at LA - Chalon Rd.

Energy content of the predicted strong ground motions

The scaled cumulative Arias intensity (CAI) of the sample SGM as well as the CAI of the predictions are shown in Figure 6.31 and Figure 6.32, respectively for dominant P- and S-Coda waves. Since the energy content of the predicted SGM is scaled by the use of the energy correction factor (equation 5.11), the results show a very well energy distribution during the time. Evaluation of the represented CAIs illustrate that the evolutionary amplitude envelope predictor has estimated the parameters of envelope function very well during the dominant S-Coda waves. The small difference between the CAI of the observed and predicted dominant P-wave is caused during the lower stability of the evolutionary amplitude predictor, especially in the beginning steps.

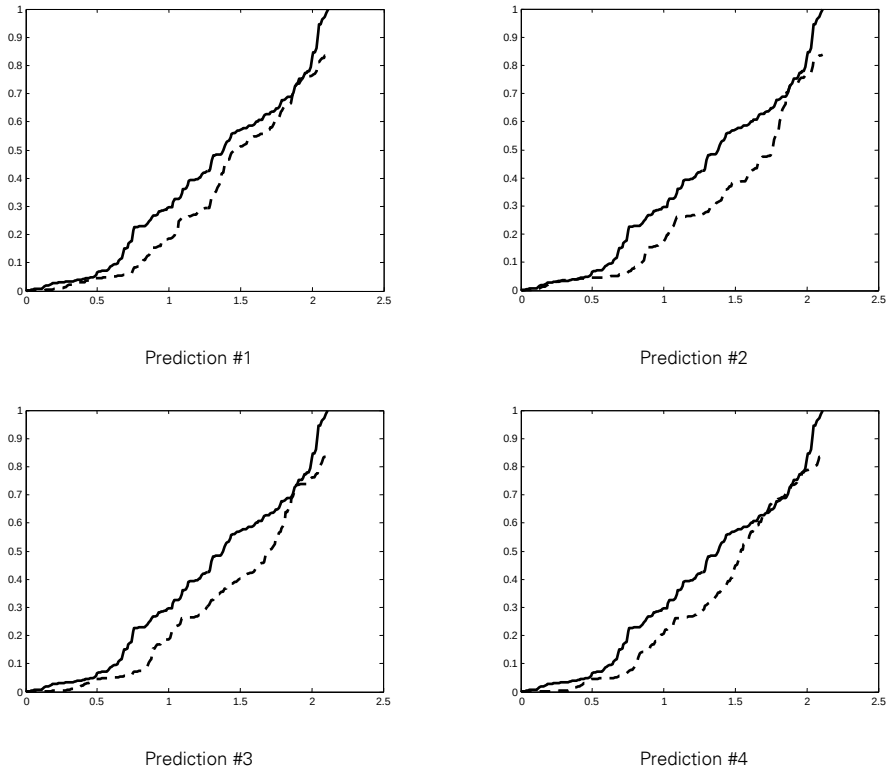

Fig. 6. 31 Scaled cumulative Arias intensity of dominant P-wave. The solid and dotted curves represent the Arias of the observed and predicted signal, respectively.

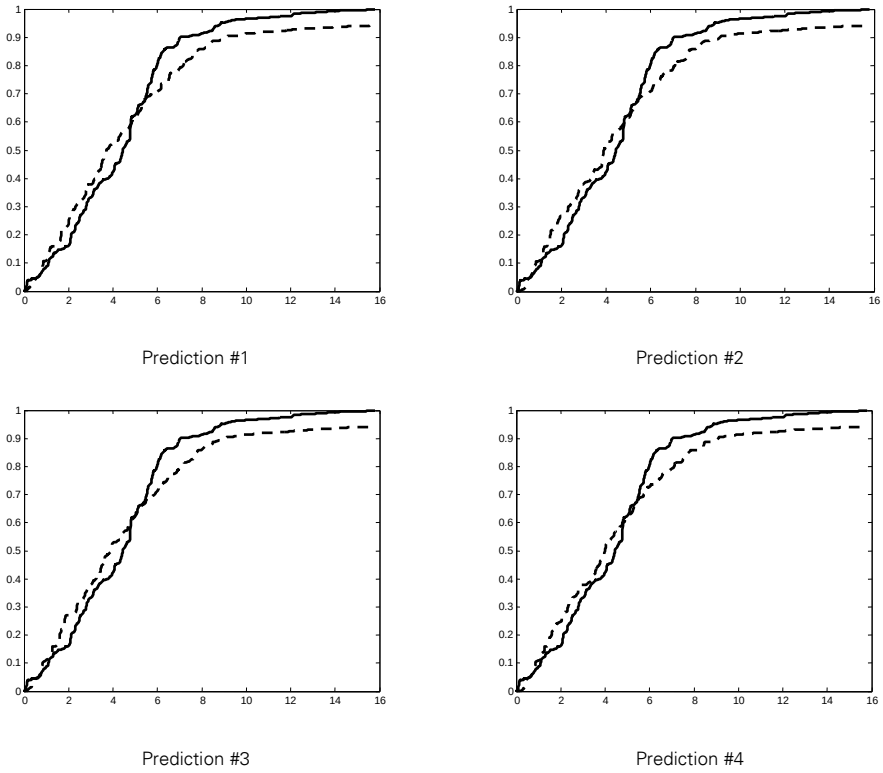

Fig. 6. 32 Scaled cumulative Arias intensity of dominant S-Coda wave. The solid and dotted curves represent the Arias of the observed and predicted signal, respectively.

Chapter 7
Summary and Outlooks

In this thesis we have developed several wave-type based strong ground motion real-time prediction models. The developed models are categorized into the non parametric soft-computing based (NP) and parametric stochastic (SP) models. The soft-computing based models use Artificial Neural Networks for the mapping of seismic observations onto the desired parameters. Two types of the soft-computing based approaches are developed; namely phase-entire (NP1) and evolutionary prediction (NP2) models.

The proposed phase-entire model (NP1) uses the relationship between the beginning signals of P-wave and the entire phase content. This model consists of two parts, one for the estimation of the length of the wave phase and the other one to generate the strong ground motion accelerogram. The advantage of the developed method is that the model take into account the non-homogeneity of the strong ground motion process. The results obtained by the use of the wave phase length estimator show that there is a meaningful relationship between the early signals of the earthquake (less than first 1.0 sec) and the phase duration. In the frequency domain, the generated accelerograms show rather well matching with the target signals almost in all validation datasets. The generated accelerograms can reach the peak value in the same position as the observed signal. The significant drawback of the model is that the energy content which is represented by Cumulative Arias Intensity of the generated accelerogram is lower than the observed

signal. Furthermore, it has been seen that the sudden peaks were not be predicted completely. Using more training datasets may improve the prediction results.

The second developed soft-computing based prediction model, namely the evolutionary model (NP2) is trained by the use of the measured data which recorded more and more during ongoing time. The training process has been conducted using 91 well recorded three orthogonal records based on several categorization aspects, namely based on epicentral distance, focal mechanism and soil type categorizations. The most uniform error distribution and less training epochs were obtained by the use of the categorization based on the focal mechanism. Additionally the training process has performed using three windowing approaches to find out the effect of windowing method, namely constant windowing (NP2.1) (for 0.2, 0.35 and 0.5 sec), semi-adaptive (NP2.2) and adaptive windowing (NP2.3) are deployed. It is shown that the performance of the predictor in the case of the constant windowing (NP2.1) approach is strongly related to the dominant frequency and non-stationary frequency content of the strong ground motion accelerogram. On the other hand the efficiency of constant windowing (NP2.1) is directly related to the windows length. Nevertheless, surveying the average error values shows that the networks which apply the constant windowing approach (NP2.1) in general have the higher average error value than the networks which work with frequency adaptive windowing approach.

The obtained results also show that the networks constructed based on the semi-adaptive approach (NP2.2) could not perform an acceptable prediction compare with the adaptive windowing approach (NP2.3). The predicted accelerogram by the use of the adaptive windowing approach (NP2.3) shows the best compatibility between the observed and predicted accelerogram compare with the windowing approaches. Response spectra of the predicted accelerogram show a very well adaptability in dominant period region. The best frequency distribution along the time is obtained by the use of the adaptive windowing approach (NP2.3) as well.

The predictor shows an acceptable performance in real-time prediction of accelerograms which contain wide range of frequencies like Chi-Chi-05 (75) as well as which are spread in a narrow frequency range like Chi-Chi-06 (86). Nevertheless, the amplitude values of the predicted signal in some cases are less than observed event which noted the use of an amplitude envelope scaling approach. Generally, the acceleration response spectra and the spectrograms of the predicted accelerograms show that the peak values as well as the distribution of the dominant frequencies along the time axes have been caught very well. It can be concluded that using adaptive time windows relevant to the dominant frequency of the signal makes the model capable to catch and predict the frequency non-stationarity of the strong ground motion process.

The proposed stochastic real-time prediction model (SP) uses two separated spectral and temporal models to form the non-stationary strong ground motion accelerogram. The model applies an approach based on the fitting a parameterized stochastic model to real-time recorded strong ground motion in order to model the frequency content of the strong ground motion and a soft-computing based method to model the amplitude envelope function. As it was described in chapter 5, the evolutionary amplitude envelope predictor performs the form estimation by the use of the real-time measured signal in

cumulative order. The results obtained from the dominant P-wave envelope predictor show that the model can estimate the target envelope function properly except the early trails in which the model shows instability during the prediction of the envelope curves. The resulted curves obtained from the dominant S-Coda wave envelope predictor show that the model can find the target envelope function from the early trail steps very well. It is also notable that the developed prediction models were able to find correctly the position of the peak value.

The prediction results of the stochastic real-time model (SP) shows also that the predicted accelerograms could follow very well the amplitude envelope of the sample data as well as the peak values in every seismic phase. The frequency content of the predicted strong ground motion shows in some cases a mismatch to the observed data. Despite of it, the dominant frequency distribution along the time could be predicted well. Since the energy content of the predicted strong ground motion are scaled by the use of the energy correction factor (equation 5.11), the results show a very well energy distribution during the time. Evaluation of the represented cumulative Arias intensity during the dominant S-Coda waves illustrate that the evolutionary amplitude envelope predictor has estimated the parameters of the envelope function very well. The little difference between the CAI of the observed and predicted P-wave is caused by the lower stability of the evolutionary amplitude predictor, especially in the beginning steps.

It can be concluded that the wave type based modeling concept which has the advantage of a conceptual physical modeling of the different seismic phases will lead to the most proper modeling of the process. An important outcome of the performance studies of the developed models is that the frequency non-stationarity of strong ground motion process can be satisfied by the use of the evolutionary soft-computing based model (NP2) and the temporal non-stationary can be very well considered by the use of the evolutionary envelope predictor (SP). Additionally to consider the local soil condition (site effect) using of the multi mode/layer power spectral density function can be recommended.

This study lays a foundation for more effective use of real-time predictive control systems by the use of wave-type based real-time strong ground motion prediction models. The independency of the developed prediction models from the building control equations makes the application of the model in other fields of real-time seismology possible. On the basis of the developed model the parameters of the strong ground motion likes PGA, duration and magnitude can be estimated more precisely according to the physical concept of the strong ground motion process which is considered in the model. Since the soft-computing based methods requires a large training database so that the Artificial Neural Networks (ANNs) can learn the desired input-output relations including, e.g., local ground motion characteristics at the sensor using of the bigger database with the proper data categorization is necessary.

APPENDIX A

Table A. 1 Information about the using data set in Entire-Phase (NP1) prediction model.

No.	Earthquake	YEAR	Mw	Focal Mechanism	EpiD (km)	Vs30 (m/s)	PGA (g)
1	Sarein, Iran	1997	6.10	SS	25	750	0.615
2	Cape Mendocino	1992	7.10	R	10.36	513.7	1.3455
3	Kocaeli, Turkey	1999	7.40	SS	5.31	811.0	0.2037
4	Loma prieta, US	1989	6.90	RO	28.64	1428.0	0.4360
5	Northridge, US	1994	6.00	R	21.55	285.9	0.3848
6	Whittier Narrows, US	1987	6.00	RO	4.77	401.4	0.2384
7	Avaj, Iran	2002	6.50	N	31	600	0.498
8	Duzce, Turkey	1999	7.10	SS	27.74	659.6	0.1445
9	Irpinia, Italy	1980	6.20	N	11.97	600.0	0.1787
10	San fernando, US	1971	6.60	R	24.19	821.7	0.1631

* The abbreviations N, SS, R and RO denote Normal, Strike - Slip, Reverse and Reverse - Oblique faulting respectively

Table A. 2 Information about the using database in non-parametric Evolutionary (NP2) model.

No.	Earthquake	YEAR	Mw	Focal Mech.	EpiD (km)	Vs30 (m/s)	PGA (g)	PGV (cm/sec)	PGD (cm)	Dur. (sec)
1	Northridge-01	1994	6.69	R	31.73	270	0.1412	12.99	3.08	15.7
2	Northridge-01	1994	6.69	R	33.77	309	0.2727	22.86	2.21	24.1
3	Northridge-01	1994	6.69	R	8.48	380	0.8026	74.13	16.32	28.9
4	Northridge-01	1994	6.69	R	32.72	376	0.1647	17.35	3.01	28.5
5	Northridge-01	1994	6.69	R	36.47	376	0.3492	19.39	2.38	27.4
6	Northridge-01	1994	6.69	R	14.41	706	0.3186	32.27	5.02	30.6
7	Northridge-01	1994	6.69	R	40.65	602	0.2153	9.97	4.44	24.9
8	Northridge-01	1994	6.69	R	44.77	671	0.1690	9.02	3.31	26.0
9	Northridge-01	1994	6.69	R	31.45	405	0.2291	22.31	4.13	29.1
10	Northridge-01	1994	6.69	R	44.01	455	0.2337	12.98	1.25	16.9
11	Northridge-01	1994	6.69	R	48.28	376	0.1753	14.52	1.56	23.0
12	Northridge-01	1994	6.69	R	44.32	401	0.2087	10.23	2.27	27.5
13	Northridge-01	1994	6.69	R	40.32	379	0.1340	7.52	0.96	28.6
14	Northridge-01	1994	6.69	R	14.66	715	0.2530	16.06	5.96	30.3
15	Northridge-01	1994	6.69	R	14.41	438	0.3391	30.64	3.90	21.2
16	Northridge-01	1994	6.69	R	13.11	251	0.7123	109.38	52.35	25.8
17	Northridge-01	1994	6.69	R	13.60	371	0.6469	95.07	33.43	24.6
18	Northridge-01	1994	6.69	R	5.41	257	1.6615	96.00	34.36	20.4
19	Northridge-01	1994	6.69	R	14.19	376	0.2591	13.76	3.13	18.4
20	Kobe, Japan	1995	6.90	SS	8.70	609	0.4862	35.73	10.75	24.9
21	Kobe, Japan	1995	6.90	SS	13.12	256	0.6528	117.14	33.06	26.2
22	Chi-Chi, Taiwan	1999	7.62	RO	37.83	553	0.1748	29.54	9.61	46.1
23	Chi-Chi, Taiwan	1999	7.62	RO	44.02	233	0.2595	37.24	25.86	59.6
24	Chi-Chi, Taiwan	1999	7.62	RO	37.83	553	0.2069	26.89	14.88	53.9
25	Chi-Chi, Taiwan	1999	7.62	RO	31.96	259	0.3822	87.47	53.62	53.5
26	Chi-Chi, Taiwan	1999	7.62	RO	36.20	473	0.1956	39.82	31.88	38.6
27	Chi-Chi, Taiwan	1999	7.62	RO	42.05	273	0.1373	34.73	35.79	55.3
28	Chi-Chi, Taiwan	1999	7.62	RO	4.96	443	0.3927	34.71	22.08	42.5
29	Chi-Chi, Taiwan	1999	7.62	RO	7.64	364	0.5290	52.08	12.54	41.8
30	Chi-Chi, Taiwan	1999	7.62	RO	36.20	473	0.2200	52.00	64.34	49.4
31	Chi-Chi, Taiwan	1999	7.62	RO	8.91	553	0.7942	92.65	28.79	43.2
32	Chi-Chi, Taiwan	1999	7.62	RO	7.04	553	0.2878	30.97	24.38	36.4
33	Chi-Chi, Taiwan	1999	7.62	RO	45.56	714	0.2444	93.82	66.49	49.5
34	Chi-Chi, Taiwan	1999	7.62	RO	37.65	474	0.1574	44.33	37.18	53.4
35	Chi-Chi, Taiwan	1999	7.62	RO	37.73	474	0.1429	42.36	33.52	54.4

* The abbreviations SS, R and RO denote Strike - Slip, Reverse and Reverse - Oblique faulting respectively

Table A.2 Information about the using database in non-parametric Evolutionary (NP2) model (Continued).

No.	Earthquake	YEAR	Mw	Focal Mech.	EpiD (km)	Vs30 (m/s)	PGA (g)	PGV (cm/sec)	PGD (cm)	Dur. (sec)
36	Chi-Chi, Taiwan	1999	7.62	RO	36.36	474	0.1612	50.02	38.73	53.9
37	Chi-Chi, Taiwan	1999	7.62	RO	46.32	215	0.0787	37.67	33.62	61.5
38	Chi-Chi, Taiwan	1999	7.62	RO	44.37	230	0.0720	25.86	24.30	60.8
39	Chi-Chi, Taiwan	1999	7.62	RO	33.80	273	0.1492	38.30	30.09	56.0
40	Duzce, Turkey	1999	7.14	SS	41.27	326	0.7662	59.68	17.69	31.9
41	Duzce, Turkey	1999	7.14	SS	1.61	276	0.4273	70.77	47.30	19.6
42	Duzce, Turkey	1999	7.14	SS	31.56	481	0.1174	12.85	8.10	24.9
43	Hector Mine	1999	7.13	SS	47.97	271	0.1935	22.06	17.12	44.2
44	Chi-Chi, Taiwan-	1999	6.20	R	33.66	553	0.0770	8.30	3.37	32.1
45	Chi-Chi, Taiwan-	1999	6.20	R	46.48	455	0.0318	2.91	0.82	44.4
46	Chi-Chi, Taiwan-	1999	6.20	R	42.94	461	0.0353	4.86	1.27	25.8
47	Chi-Chi, Taiwan-	1999	6.20	R	0.51	443	0.4344	27.29	3.49	10.4
48	Chi-Chi, Taiwan-	1999	6.20	R	5.57	364	0.3022	14.30	1.50	10.6
49	Chi-Chi, Taiwan-	1999	6.20	R	10.45	553	0.0865	6.58	1.93	11.2
50	Chi-Chi, Taiwan-	1999	6.20	SS	47.15	226	0.0312	8.94	6.81	57.3
51	Chi-Chi, Taiwan-	1999	6.20	SS	35.44	205	0.0769	15.35	9.94	42.3
52	Chi-Chi, Taiwan-	1999	6.20	SS	49.35	201	0.0525	11.22	8.83	55.6
53	Chi-Chi, Taiwan-	1999	6.20	SS	36.15	553	0.0957	7.21	1.83	30.5
54	Chi-Chi, Taiwan-	1999	6.20	SS	38.91	442	0.1166	9.76	2.93	56.0
55	Chi-Chi, Taiwan-	1999	6.20	SS	10.10	553	0.3240	37.84	10.28	24.3
56	Chi-Chi, Taiwan-	1999	6.20	SS	36.11	553	0.1089	11.08	2.84	38.8
57	Chi-Chi, Taiwan-	1999	6.20	SS	38.97	505	0.0804	5.79	1.89	40.6
58	Chi-Chi, Taiwan-	1999	6.20	SS	37.50	474	0.0795	2.81	0.44	29.3
59	Chi-Chi, Taiwan-	1999	6.20	SS	32.52	553	0.0524	6.84	2.24	36.0
60	Chi-Chi, Taiwan-	1999	6.20	SS	47.70	213	0.0598	10.72	4.74	48.1
61	Chi-Chi, Taiwan-	1999	6.20	SS	47.28	459	0.0297	6.01	2.20	40.3
62	Chi-Chi, Taiwan-	1999	6.20	R	48.60	428	0.2461	10.27	1.18	38.3
63	Chi-Chi, Taiwan-	1999	6.20	R	49.24	273	0.0402	3.18	0.35	34.6
64	Chi-Chi, Taiwan-	1999	6.20	R	35.92	375	0.0568	3.37	0.29	33.3
65	Chi-Chi, Taiwan-	1999	6.20	R	37.65	273	0.0518	3.44	0.52	34.5
66	Chi-Chi, Taiwan-	1999	6.20	R	42.27	474	0.0746	5.10	0.69	38.1
67	Chi-Chi, Taiwan-	1999	6.20	R	42.48	396	0.0819	6.26	1.08	44.0
68	Chi-Chi, Taiwan-	1999	6.20	R	38.90	379	0.0858	5.29	0.68	40.1
69	Chi-Chi, Taiwan-	1999	6.20	R	37.30	474	0.0638	3.54	0.52	33.7
70	Chi-Chi, Taiwan-	1999	6.20	R	45.27	273	0.0495	5.56	1.00	43.5

* The abbreviations SS, R and RO denote Strike - Slip, Reverse and Reverse - Oblique faulting respectively

Table A.2 Information about the using database in non-parametric Evolutionary (NP2) model (Continued).

No.	Earthquake	YEAR	Mw	Focal Mech.	EpiD (km)	Vs30 (m/s)	PGA (g)	PGV (cm/sec)	PGD (cm)	Dur. (sec)
71	Chi-Chi, Taiwan-	1999	6.20	R	47.23	643	0.0493	4.10	0.74	35.8
72	Chi-Chi, Taiwan-	1999	6.20	R	48.17	273	0.0504	2.83	0.31	41.0
73	Chi-Chi, Taiwan-	1999	6.20	R	48.72	474	0.0371	2.04	0.33	37.2
74	Chi-Chi, Taiwan-	1999	6.20	R	48.10	273	0.0639	3.82	0.52	55.0
75	Chi-Chi, Taiwan-	1999	6.20	R	44.67	553	0.0515	2.59	0.26	36.9
76	Chi-Chi, Taiwan-	1999	6.20	R	43.34	474	0.0761	5.26	0.63	37.9
77	Chi-Chi, Taiwan-	1999	6.20	R	48.16	434	0.1014	6.46	1.06	39.2
78	Chi-Chi, Taiwan-	1999	6.30	R	49.00	543	0.1479	15.36	4.09	38.9
79	Chi-Chi, Taiwan-	1999	6.30	R	48.65	379	0.0616	5.75	0.67	40.7
80	Chi-Chi, Taiwan-	1999	6.30	R	46.03	474	0.0295	2.96	0.51	34.1
81	Chi-Chi, Taiwan-	1999	6.30	R	49.41	553	0.0369	2.79	0.42	32.7
82	Chi-Chi, Taiwan-	1999	6.30	R	47.32	487	0.0396	4.44	1.28	39.6
83	Chi-Chi, Taiwan-	1999	6.30	R	48.67	273	0.0492	5.11	1.13	42.9
84	Chi-Chi, Taiwan-	1999	6.30	R	49.98	455	0.0372	4.89	0.81	37.0
85	Chi-Chi, Taiwan-	1999	6.30	R	38.63	306	0.1366	16.43	3.74	49.5
86	Chi-Chi, Taiwan-	1999	6.30	R	38.41	434	0.0505	7.31	1.98	44.3
87	Chi-Chi, Taiwan-	1999	6.30	R	34.27	615	0.1285	8.58	3.72	34.7
88	Chi-Chi, Taiwan-	1999	6.30	R	12.26	364	0.6443	37.98	5.36	11.5
89	Chi-Chi, Taiwan-	1999	6.30	R	45.89	473	0.0400	5.28	1.69	36.8
90	Chi-Chi, Taiwan-	1999	6.30	R	45.97	213	0.0680	10.56	3.59	49.6
91	Chi-Chi, Taiwan-	1999	6.30	R	33.15	664	0.2565	13.59	3.87	36.9

* The abbreviations SS, R and RO denote Strike - Slip, Reverse and Reverse - Oblique faulting respectively

Table A. 3 Information about the using data set in Stochastic prediction (SP) model.

No.	Earthquake	YEAR	Station	Mw	Focal Mech.	EpiD (km)	Vs30 (m/s)	PGA (g)	PGV (cm/sec)	PGD (cm)
1	Northridge-01	1994	Alhambra -	6.69	R	40.1	550	0.08	8.63	1.81
2	Northridge-01	1994	Anaheim - W	6.69	R	70.4	234.88	0.07	5.99	1.37
3	Northridge-01	1994	Anaverde	6.69	R	52.8	445.98	0.05	5.81	1.46
4	Northridge-01	1994	Arcadia -	6.69	R	46.4	308.65	0.10	7.83	1.48
5	Northridge-01	1994	Arcadia -	6.69	R	48.4	367.53	0.11	5.95	1.58
6	Northridge-01	1994	Arleta -	6.69	R	11.1	297.71	0.33	30.90	12.8
7	Northridge-01	1994	Baldwin Park	6.69	R	54.6	308.65	0.11	5.83	1.25
8	Northridge-01	1994	Bell Gardens -	6.69	R	45.2	308.65	0.08	7.92	2.92
9	Northridge-01	1994	Beverly Hills -	6.69	R	16.2	545.66	0.51	32.82	6.67
10	Northridge-01	1994	Beverly Hills -	6.69	R	13.3	355.81	0.46	54.22	12.0
11	Northridge-01	1994	Big Tujunga,	6.69	R	31.5	445.98	0.20	9.64	1.00
12	Northridge-01	1994	Brea - S	6.69	R	68.6	308.65	0.11	8.11	1.12
13	Northridge-01	1994	Buena Park -	6.69	R	63.5	308.65	0.12	7.74	1.42
14	Northridge-01	1994	Burbank -	6.69	R	23.1	821.69	0.14	9.09	2.05
15	Northridge-01	1994	Camarillo	6.69	R	48.3	234.88	0.12	12.11	3.54
16	Northridge-01	1994	Canoga Park -	6.69	R	4.85	267.49	0.38	44.96	14.9
17	Northridge-01	1994	Canyon	6.69	R	26.4	308.65	0.44	43.33	12.3
18	Northridge-01	1994	Carson -	6.69	R	51.0	361.17	0.08	5.87	1.24
19	Northridge-01	1994	Carson -	6.69	R	50.3	160.58	0.09	7.18	1.79
20	Northridge-01	1994	Castaic - Old	6.69	R	40.6	450.28	0.49	46.51	13.5
21	Northridge-01	1994	Compton -	6.69	R	47.4	308.65	0.11	7.18	2.64
22	Northridge-01	1994	Covina - W	6.69	R	60.3	271.44	0.09	6.25	1.36
23	Northridge-01	1994	Downey -	6.69	R	49.8	245.06	0.16	10.04	1.63
24	Northridge-01	1994	Downey - Co	6.69	R	47.4	271.90	0.20	12.11	2.18
25	Northridge-01	1994	Duarte - Mel	6.69	R	56.9	445.98	0.06	3.11	1.17
26	Northridge-01	1994	El Monte -	6.69	R	50.8	308.65	0.14	9.49	3.01
27	Northridge-01	1994	Featherly	6.69	R	86.4	308.65	0.10	6.58	0.66
28	Northridge-01	1994	Glendale - Las	6.69	R	29.7	445.98	0.26	10.83	1.81
29	Northridge-01	1994	Glendora - N	6.69	R	62.2	445.98	0.06	3.77	1.12
30	Northridge-01	1994	Hacienda	6.69	R	61.2	337.00	0.06	3.97	0.86
31	Northridge-01	1994	Hollywood -	6.69	R	21.7	234.88	0.20	22.68	5.30
32	Northridge-01	1994	Huntington	6.69	R	71.0	234.88	0.08	6.07	1.76
33	Northridge-01	1994	Inglewood -	6.69	R	41.9	316.02	0.10	8.41	2.44
34	Northridge-01	1994	LA - 116th St	6.69	R	41.0	301.00	0.17	12.48	2.58
35	Northridge-01	1994	LA - Baldwin	6.69	R	28.2	297.07	0.20	17.19	5.36

* R denotes Reverse faulting

Table A.3 Information about the using data set in Stochastic prediction (SP) model (Countinued).

No.	Earthquake	YEAR	Station	Mw	Focal Mech.	EpiD (km)	Vs30 (m/s)	PGA (g)	PGV (cm/sec)	PGD (cm)
36	Northridge-01	1994	LA -	6.69	R	17.9	416.58	0.18	23.23	5.91
37	Northridge-01	1994	LA - Centinela	6.69	R	25.4	234.88	0.37	21.50	4.73
38	Northridge-01	1994	LA - Century	6.69	R	20.2	277.98	0.22	24.55	6.69
39	Northridge-01	1994	LA - Chalon	6.69	R	14.9	740.05	0.21	23.13	3.95
40	Northridge-01	1994	LA - City	6.69	R	39.1	365.22	0.27	14.07	2.61
41	Northridge-01	1994	LA - Cypress	6.69	R	33.2	445.98	0.21	13.30	2.13
42	Northridge-01	1994	LA - E Vernon	6.69	R	37.3	308.65	0.15	10.03	1.82
43	Northridge-01	1994	LA - Fletcher	6.69	R	30.2	445.98	0.21	16.51	2.93
44	Northridge-01	1994	LA -	6.69	R	23.6	316.46	0.34	23.41	4.25
45	Northridge-01	1994	LA - N Faring	6.69	R	16.9	255.00	0.25	20.72	3.82
46	Northridge-01	1994	LA - N	6.69	R	35.2	405.19	0.15	9.20	1.36
47	Northridge-01	1994	LA - N	6.69	R	27.2	315.06	0.37	22.05	2.97
48	Northridge-01	1994	LA - Obregon	6.69	R	39.3	349.43	0.47	21.79	2.05
49	Northridge-01	1994	LA - Pico &	6.69	R	31.7	270.19	0.14	12.99	3.08
50	Northridge-01	1994	LA - S Grand	6.69	R	33.7	308.65	0.27	22.86	2.21
51	Northridge-01	1994	LA - Saturn St	6.69	R	25.5	308.71	0.45	35.34	5.96
52	Northridge-01	1994	LA -	6.69	R	8.48	380.06	0.80	74.13	16.3
53	Northridge-01	1994	LA - Temple	6.69	R	32.7	376.07	0.16	17.35	3.01
54	Northridge-01	1994	LA - UCLA	6.69	R	18.6	398.42	0.39	22.41	5.11
55	Northridge-01	1994	LA - Univ.	6.69	R	36.4	376.07	0.35	19.39	2.38
56	Northridge-01	1994	LA - W 15th	6.69	R	29.5	405.19	0.13	12.40	4.31
57	Northridge-01	1994	LA -	6.69	R	18.9	401.26	0.13	11.17	2.23
58	Northridge-01	1994	LB - City Hall	6.69	R	58.8	381.23	0.04	4.12	1.48
59	Northridge-01	1994	LB - Rancho	6.69	R	52.5	405.19	0.07	6.28	2.15
60	Northridge-01	1994	La Crescenta	6.69	R	27.8	445.98	0.17	11.52	2.29
61	Northridge-01	1994	La Puente -	6.69	R	61.9	308.65	0.11	8.51	0.74
62	Northridge-01	1994	Lake Hughes	6.69	R	53.3	425.34	0.08	9.64	3.20
63	Northridge-01	1994	Lake Hughes	6.69	R	40.6	602.10	0.22	9.97	4.44
64	Northridge-01	1994	Lake Hughes	6.69	R	49.9	821.69	0.08	5.49	3.02
65	Northridge-01	1994	Lake Hughes	6.69	R	49.9	554.00	0.05	4.27	2.13
66	Northridge-01	1994	Lake Hughes	6.69	R	44.7	670.84	0.17	9.02	3.31
67	Northridge-01	1994	Lakewood -	6.69	R	57.9	234.88	0.13	9.86	2.32
68	Northridge-01	1994	Lancaster -	6.69	R	67.0	271.44	0.07	6.19	1.38
69	Northridge-01	1994	Lawndale -	6.69	R	39.3	361.17	0.11	8.22	2.76
70	Northridge-01	1994	Leona Valley	6.69	R	51.8	684.94	0.08	6.29	1.85

* R denotes Reverse faulting

Table A.3 Information about the using data set in Stochastic prediction (SP) model (Countinued).

No.	Earthquake	YEAR	Station	Mw	Focal Mech.	EpiD (km)	Vs30 (m/s)	PGA (g)	PGV (cm/sec)	PGD (cm)
71	Northridge-01	1994	Leona Valley	6.69	R	51.9	684.94	0.09	7.63	1.93
72	Northridge-01	1994	Leona Valley	6.69	R	52.2	445.98	0.08	10.04	2.07
73	Northridge-01	1994	Leona Valley	6.69	R	52.4	445.98	0.13	15.28	2.61
74	Northridge-01	1994	Leona Valley	6.69	R	52.6	327.44	0.14	11.77	1.70
75	Northridge-01	1994	Littlerock -	6.69	R	61.2	821.69	0.07	4.93	1.13
76	Northridge-01	1994	Malibu - Point	6.69	R	31.2	349.54	0.10	8.63	1.93
77	Northridge-01	1994	Manhattan	6.69	R	38.6	405.19	0.17	16.88	3.44
78	Northridge-01	1994	Montebello -	6.69	R	47.1	405.19	0.15	8.21	1.84
79	Northridge-01	1994	Moorpark -	6.69	R	31.4	405.19	0.23	22.31	4.13
80	Northridge-01	1994	Mt Wilson -	6.69	R	45.7	821.69	0.17	6.41	0.58
81	Northridge-01	1994	Neenach -	6.69	R	71.4	308.65	0.06	12.72	6.10
82	Northridge-01	1994	Newhall - Fire	6.69	R	20.2	269.14	0.70	81.83	26.0
83	Northridge-01	1994	Newhall - W	6.69	R	21.5	285.93	0.38	79.07	30.2
84	Northridge-01	1994	Pacific	6.69	R	18.2	445.98	0.33	22.65	5.99
85	Northridge-01	1994	Pacoima	6.69	R	19.2	508.08	0.35	45.38	11.4
86	Northridge-01	1994	Palmdale -	6.69	R	56.7	551.56	0.07	8.68	1.78
87	Northridge-01	1994	Pasadena - N	6.69	R	44.0	455.38	0.23	12.98	1.25
88	Northridge-01	1994	Rancho Palos	6.69	R	53.1	477.65	0.06	4.55	0.86
89	Northridge-01	1994	Rinaldi	6.69	R	10.9	282.25	0.63	109.24	28.2
90	Northridge-01	1994	San Marino -	6.69	R	40.3	379.43	0.13	7.52	0.96
91	Northridge-01	1994	San Pedro -	6.69	R	58.3	376.07	0.10	5.94	0.73
92	Northridge-01	1994	Sandberg -	6.69	R	61.7	821.69	0.09	10.21	4.78
93	Northridge-01	1994	Santa Fe	6.69	R	51.9	308.65	0.13	7.76	1.06
94	Northridge-01	1994	Santa Monica	6.69	R	22.4	336.20	0.59	31.22	10.5
95	Northridge-01	1994	Santa Susana	6.69	R	14.6	715.12	0.25	16.06	5.96
96	Northridge-01	1994	Seal Beach -	6.69	R	66.1	370.79	0.08	6.10	1.79
97	Northridge-01	1994	Simi Valley -	6.69	R	12.1	557.42	0.75	39.18	5.15
98	Northridge-01	1994	Stone Canyon	6.69	R	14.4	438.34	0.34	30.64	3.90
99	Northridge-01	1994	Sunland - Mt	6.69	R	24.1	445.98	0.14	14.55	4.91
100	Northridge-01	1994	Sylmar -	6.69	R	13.6	370.52	0.65	95.07	33.4
101	Northridge-01	1994	Sylmar - Olive	6.69	R	16.7	440.54	0.70	95.38	21.9
102	Northridge-01	1994	Tarzana -	6.69	R	5.41	257.21	1.66	96.00	34.3
103	Northridge-01	1994	Terminal	6.69	R	58.5	229.79	0.16	13.90	2.24
104	Northridge-01	1994	Tustin - E	6.69	R	85.8	234.88	0.07	3.42	0.61
105	Northridge-01	1994	Vasquez	6.69	R	38.0	996.43	0.14	14.27	2.90
106	Northridge-01	1994	Ventura -	6.69	R	68.4	271.44	0.07	10.89	3.41
107	Northridge-01	1994	West Covina -	6.69	R	57.6	308.65	0.06	5.76	1.96
108	Northridge-01	1994	Wrightwood -	6.69	R	77.5	821.69	0.05	4.15	0.78
109	Northridge-01	1994	Wrightwood -	6.69	R	84.3	338.54	0.06	3.01	0.47

* R denotes Reverse faulting

APPENDIX B

Insert Earthquake Record Data

Every strong ground motion recording organization has its own data recording format, which might be to some extent different from the other organizations. The earthquake record file is an ASCII file, which contains the earthquake time history data (acceleration, velocity or displacement) and other information such as recording sample-rate, epicentral location, station identification code or name, azimuth of the station and etc. Working with different data formats forces us to use either format-depending program, which are able to recognize and read every predefined format or at the first step store the record's data in a configuration file, which seems identical for every earthquake data. `Insertrecord` is a program, which was developed to read and store the earthquake record data from the recording ASCII file to Matlab variables (calls Structure and are saved with the extension .mat) as configuration file. In the following paragraphs, we will take a tour on the graphical user interface (GUI) of the developed program and take a glance at the structure of the code.

Let us to have a look at the program. After the running of `Insertrecord`, appears the main window of the program, which contains the following tabs: File, View and ANN (Figure B.1). File tab has the menus New, Load, Save As and Exit.

Fig. B.1 Main window of `Insertrecord`.

Choosing the New menu leads to appear the window which is shown in Figure B.2. This window was designed to get the essential data of an earthquake record and generate the configuration file. The following steps must be performed to make a configuration file of an earthquake event (the numbers refer to the Figure B.2):

- The desired earthquake record ASCII file can be selected through the current directory list, which is placed at left side of the window. The current directory can be changed and refreshed using the buttons **Change Dir.** & **Update Dir.** respectively.

- **First line** and **Last line** of the earthquake record must be entered in the appropriate fields. If no value is assigned as **last line**, the program will take the last line number of the ACSII file as the last line of the earthquake record (In the record formats, which have the entire three components in a single file the last line number should be entered manually for each components). The number of the active line is appeared above the record box in blue color (to find out the start line of the time history data in the recording format, which have the three orthogonal components in an single file, two indicator have been drown at the right side of the record box in positions one and two thirds).

- **Scale factor**, **Sample rate** and **Unit** should be inputted to the specified input fields.

- **Azimuth**, **Pick start** and **Pick end** are optional fields and can left empty.

- Using the **Select Component** popup menu, the earthquake component should be selected before making preview.

Now we can make a preview of the inserted ground motion component using button **Preview**. If it is necessary to modify the beginning or end of the earthquake record, that can be done using the buttons **Pick start** and **Pick end** and make a new preview of the modified record. By using the empty input fields for start or end of the record, program will use the original length of the record. The **Preview** button also handles confirmation process of the selected file to selected component. This process should be repeated for the other components of the earthquake record in the same manner.

- After assigning the whole components of an earthquake record, to generate the appropriate configuration file either the **Save** button will be engaged or Save option from the File tab will be selected.

- To make a new configuration variable of an earthquake either the **New** button should be engaged or New menu from the File tab must be selected.

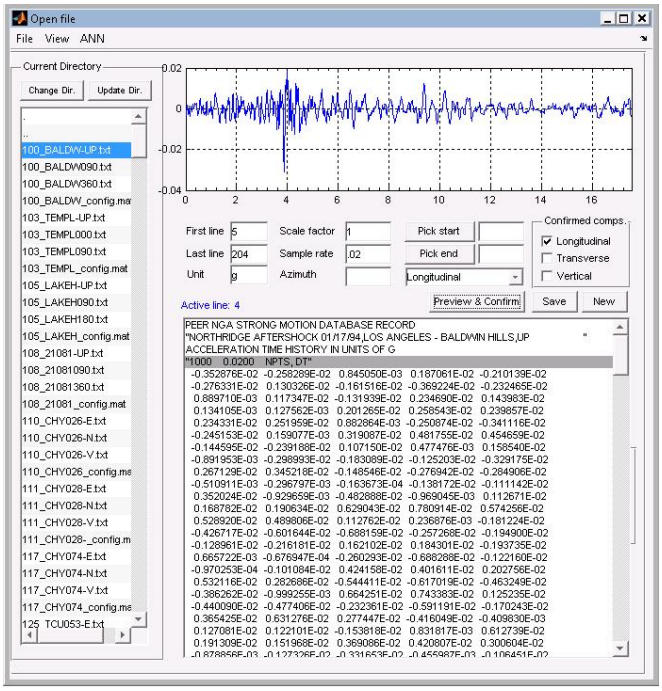

Fig. B.2 The components of the New window.

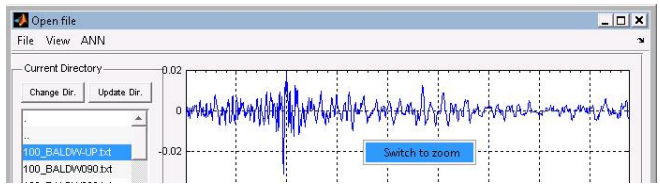

Fig. B.3 Zooming tool.

The curve at the top of the window (Figure B.2) shows the time history of the inserted earthquake, which can be refreshed after each modification using **Preview** button. By right click on the area of the curve, zooming tools can be activated, which is able to make zoom in, zoom out and reset to original view.

Take a glance at the `Insertrecord` code

The program Insertrecord consists of two parts; `Insertrecord.m` and `Insertrecord.fig`. The file with extension `*.fig` comes from the Matlab graphical user interface (GUI) structure, which stores the GUI data in the separate file. The core functions and connections between the GUI elements were be defined and controlled during Matlab code (file with extension `*.m`). The earthquake data are collected in the Matlab structure variable data, which has the following fields:

`data.comp_index`

`data.first_line_no.comp1, comp2, comp3`

`data.last_line_no.comp1, comp2, comp3`

`data.scale_factor`

`data.sample_rate`

`data.station_azimuth`

`data.acc_unit`

`data.wave_begin`

`data.wave_end`

`data.filename`

`data.filenameandpath.comp1, comp2, comp3`

`data.record_file.comp1, comp2, comp3`

`data.time_axe.comp1, comp2, comp3`

`data.acc_axe.comp1, comp2, comp3`

And the other fields, which are initialized in this step with empty value and will be get values just after performing principal component analysis in the next steps:

`data.p_length`

`data.pca_samplerate`

`data.phi`

`data.rms`

`data.tzr`

The definition of significant duration, D (sec), used was the time needed to build up between onset of P-wave and 95 per cent of the total Arias intensity of the record and the minimum value of the three components is assigned to the `data.wave_end`

variable. The variable `data` is saved in a MAT-file format (which writes the arrays currently in memory to a file as a continuous byte stream).

View the Earthquake Record Data and Perform PCA Transformation

View tab was developed to plot the three orthogonal components and principal component transformation of an earthquake record in a unique window the non-stationary frequency alteration is shown in this window. View window can be accessed via the View tab if an earthquake configuration has been loaded from the File tab (Figure B.1). The view window contains three diagrams at the right side top, which show the time history of the longitudinal, transverse and vertical components of the earthquake record respectively. The appropriate spectrograms of the earthquake components are plotted at the left side of the time history diagrams; maximum frequency domain, length of the frequency step, time windowing length and overlapping percentage are adjustable parameters, which can be modified before plotting the spectrograms (Figure B.4).

Note: MATLAB has a built-in function `spectrogram()` calculate spectrogram. This function divides a long signal into windows and performs a Fourier transform on each window, storing complex amplitudes in a table in which the columns represent time and the rows represent frequency.

Root mean square (RMS) can be shown as a red curve on the time history diagrams and the first principal component optionally (With selecting checkbox RMS). The parameters of principal component analysis (PCA) are adjusted using the windows length and sliding rate fields. Later than the performance of PCA, the second of deterioration of P-wave and starting of the S-wave dominant phase can be picked up using the **Pick P-phase** button and stored via pushing the **Store** button. First principal component (T_1) of three earthquake orthogonal components is shown at the left hand bottom diagram above the vertical angle of this principal component (Phi). In a similar manner, the spectrogram of the first principal component is illustrated at the right side bottom. To save the diagram as an image file (JPEG format), the desired diagrams must be selected and engaged the **Save diagrams** button. Right click on the diagrams and choose the **New** option makes the possibility to duplicate the diagram in extra window.

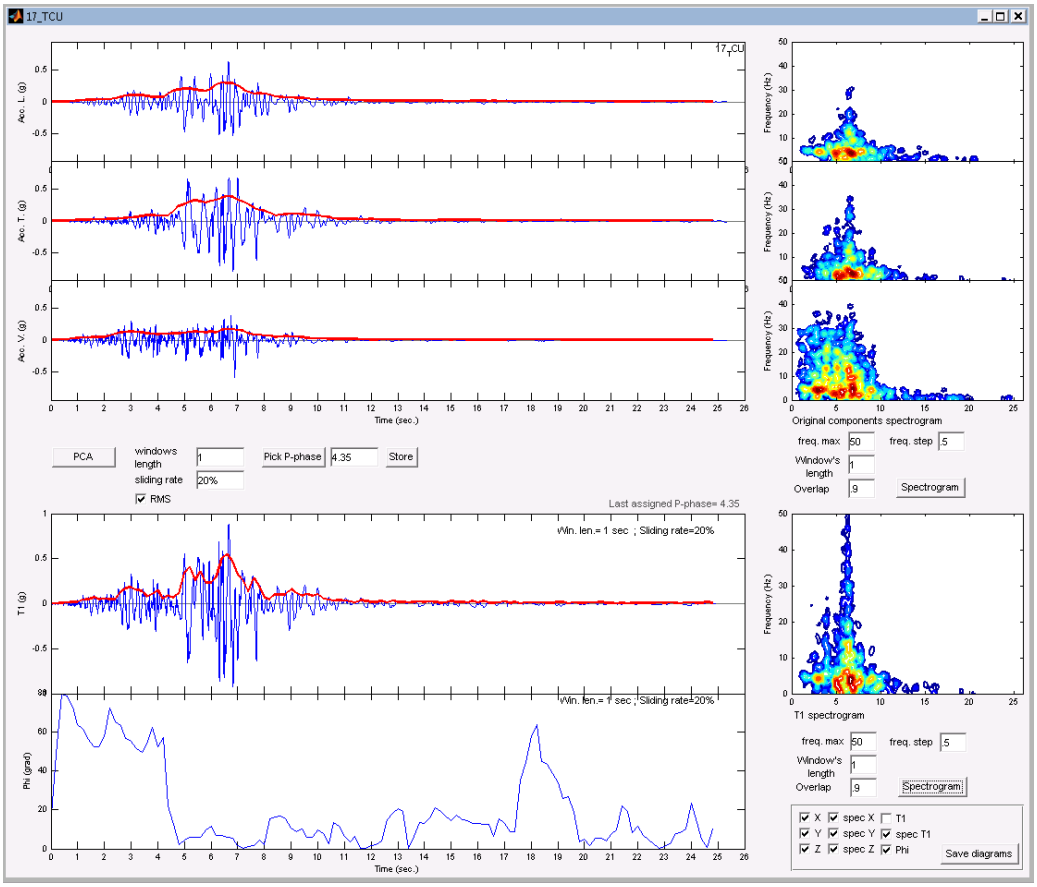

Fig. B.4 Time history, non-stationary frequency domain, first principal component and vertical angle are illustrated in the view window.

Take a Glance at the pca Code

Matlab function `spectrogram()` has been used to illustrate the frequency contain of the earthquake signal via the time axes. The part of `pca` code, which holds the principal component analysis in sliding window manner uses the stochastic principal axes paradigm. The stochastic principal axes are defined as those axes, where the cross-correlation between the three components of the acceleration vector are zero and the stochastic vector process is completely described by five values; three covariances and two rotation angles instead of nine covariances. However, this method originally suggested by Penzien and Watanabe and extended to non-stationary process approach by Kubo and Penzien and improved by Scherer and Zsohar to a stable and expressive analytical methods by improving the algorithm of the horizontal rotation angle θ and the choice of the moving time windows. (Note, the plotted spectrograms have been scaled to the maximum value)

Perform the Artificial Neural Networks analysis

To perform the Artificial Neural Networks (ANNs) analysis, ANN code has been developed. The final goal of this program is doing real-time prediction of earthquake signal, which will be done for the earthquake main phases separately; P- and S- dominate phase. The ANN code can be called either via the main window of `Insertrecord` (Figure B.1) or direct by Matlab command window (ANN window is shown in Figure B.5).

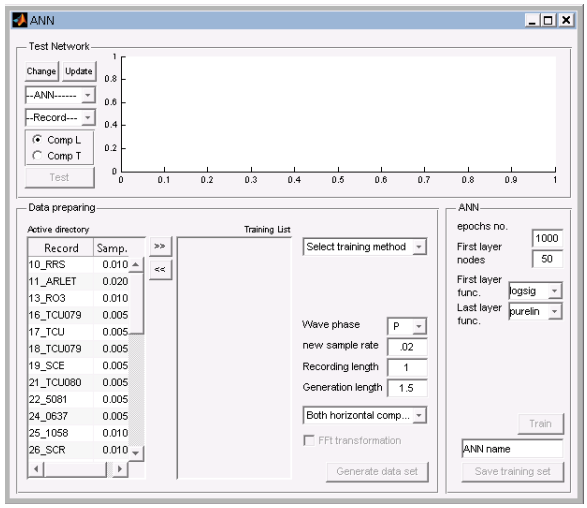

Fig. B.5 ANN window containing Data preparing, ANN and Test Network panels.

The ANN window consists of Data preparing, ANN and Test Network panels, which are designed to preparing the training data set, training the ANNs and testing the network respectively. Let begin with the Data preparing panel (Figure B.6).

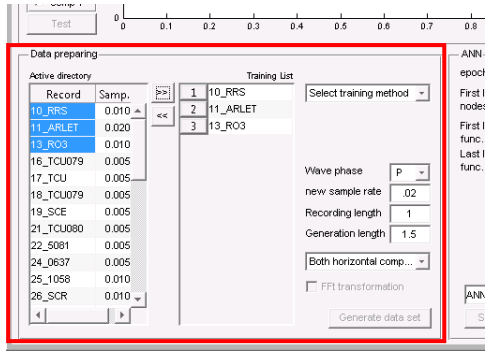

Fig. B.6 Data preparing panel in ANN window.

In **Active directory** table at the left side bottom of the ANN window, the earthquake configuration files (the files with `*.config` extension, which have been produced using `Insertrecord` program) in the current directory are shown. The configuration file name and sampling rate are listed in the first and second columns respectively. Right click on the configuration file will call the `pca` program, to view the time history and stochastic

principal components of the desired earthquake event. Because of the unequal sampling rate in different earthquake records, this is necessary to synchronize the sampling rate before performing any analysis. To build up the ANNs training list, the training earthquake records must be selected from the Active directory and inserted to the Training List table (using button **>>**), if a file or a group of files should be removed from the training list that can be done via the remove button (using button **<<**). Now it is time to **select the training method**, which must be one of the following choices:

- Signal: If we want to train the ANNs, who be able to predict the earthquake signal, this option must be selected.
- RMS-curve: Selection of this option leads to perform training of the shape function (RMS) of the earthquake signal. A polynomial degree three of RMS has been developed to model the shape function.
- RMS-curve parameters: Selection of this option leads to perform training of the configurations of the shape function (RMS) of the earthquake signal. The coefficients of the polynomial degree three of RMS have been used to model the shape function.

Dominant **Wave phase** of training data (P- or S- wave) and **new sample rate** must be adjusted before the generation of the training data set.

Fig. B.7 To generate the training data set the recording length (R) and generation length (G) must be assigned.

Recording length is the period of data feeding to the prediction system and **Generation length** is the length of the predicted signal in second (Figure B.7). It is possible to select either only longitudinal or only transverse or both horizontal components to train the ANNs using the specified pop-up menu. To perform fast Fourier transformation (FFT) before training the ANNs, **FFT** box should be selected. Now we can generate the data variable using the **Generate data set** button.

In ANN pnael (at the right side bottom of the ANN window in Figure B.5) the parameter of the neural networks are adjusted; Number of epochs, the number of the first layer's nodes, transfer function of the first and last layer. After the training of the ANNs, the structure and weights of the trained networks can be saved in the Matlab file with extension `*.ann` with the pre-assigned file name. Atfer the training of ANNs it is time to test the results (Figure B.8a). This panel contains a diagram and some buttons and pop-up menus. **Change** button changes the active directory of the program and **Upadate** button refreshes the active directory contents. To test the trained ANNs, any desiered ANNs must be selectected from the ANN (**--ANN------**) menu (Figure B.8b) . After the selectinon of the trained neural networks, a testing earthquake record should be selected using Record (**--Record---**) menu(Figure B.8c).

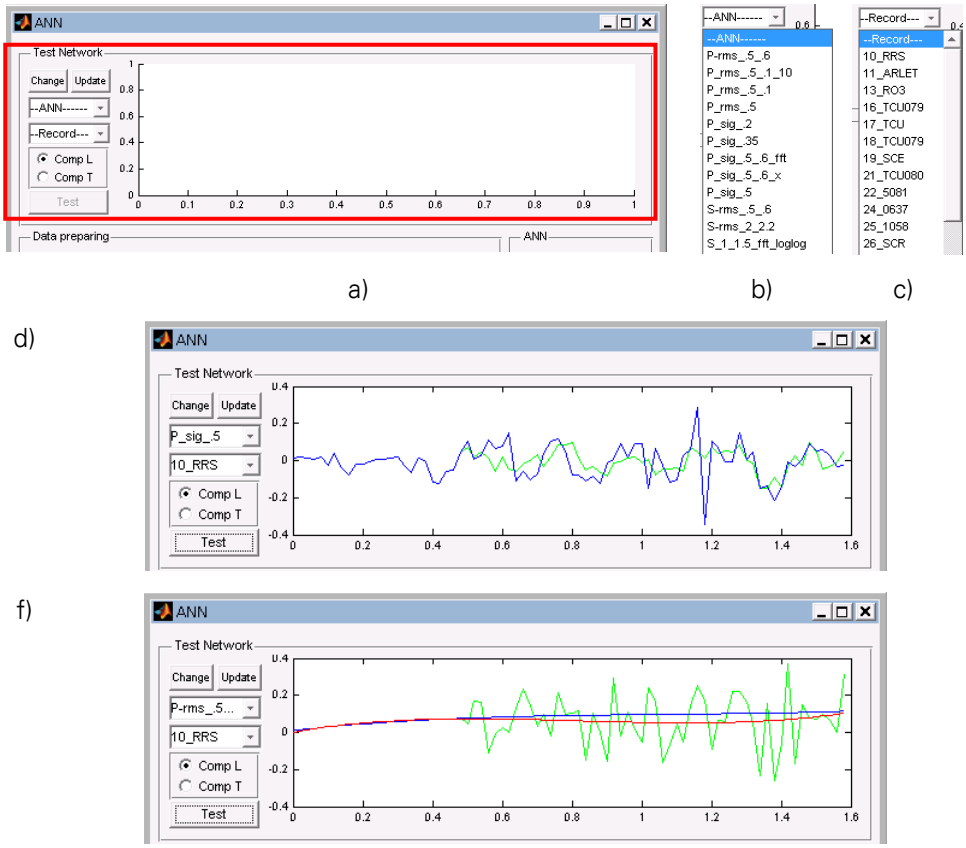

Fig. B.8 Test-Network panel in ANN window.

Before testing the trained ANNs, one of the horizontal components of the earthquake record must be selected (**Comp L** for Longitudinal and **Comp T** for Transverse component). Figure B.8d shows the predicted signal and observed one in the same diagram (observed signal is plotted with blue and predicted with green curves). In the Figure B.8f the polynomial degree three of the RMS of observed signal is shown as blue curve, the predicted RMS as green and the polynomial degree three of the predicted RMS as red curves.

REFERENCES

Aghababaii Mobarakeh, A., Rofooei, F.R. and Ahmadi, G. (2002). Simulation of earthquake records using time-varying ARMA (2, 1) model. *Probabilistic Engineering Mechanics*. **17**: 15-34.

Ahmadi, G. (1979). Generation of artificial time-histories compatible with given response spectra. *Solid Mechanics Archives*. **4**: 207-239.

Akinori, T., Kenji, T., Yuichiro, Y. and Hiroshi, K. (2008). Intelligent Fuzzy Optimal Active and Combinatorial Control System of Building Structures: Investigation on Optimization Method of Control. *Journal of Computational Science and Technology*. **2**, 3: 381-392.

Aki, K. (1967). Scaling law of seismic spectrum. *Journal of Geophysical Research*. **72-4**: 1217.

Aki, K. (1988). Local site effects on strong ground motion. *Proceeding . of Earthquake engineering and soil dynamics II*. 103-155.

Allen, R. M. (2006). Probabilistic Warning Time for Earthquake Ground Shaking in the San Francisco Bay Area. *Seismological Research Letter.* **77-3**: 371-376.

Ambraseys, N., Simpson, K. and Bommer, J. (1996). Prediction of horizontal response spectra in Europe. *Earthquake Engineering Structural Dynamics*. **25**: 371-400

Ambraseys N. & Douglas J. (2003). Near-field horizontal and vertical earthquake ground-motions. *Soil Dynamics and Earthquake Engineering*. **23**: 1-18.

Amin, M. and Ang, A.H.S. (1966). A nonstationary stochastic model for strong motion earthquakes. *Structural Research Series, University of Illinois, Urbana, IL*. No. **306**.

Amin, M and Ang, A.H.S. (1968). Nonstationary stochastic model of earthquake motions. *Journal of Engineering Mechanics Division*. **94**: 559-583.

Ansary, M. A., Noor, M. A. and Seraj, S. M. (2000). Response spectra based on simulated earthquakes and its application and assessment. *Journal of the Civil Engineering, IEB*. **27-1**: 1-20.

Arata, L. K. and Dhawan, A. P. (1992). Iterative principal axes registration: A new algorithm for retrospective correlation of MR-PET brain images. *Proc. Ann. Int. Conf. IEEE Eng. Med. Biol. Soc.* **14**: 2776-2778.

Arias, A. (1970). A Measure of Earthquake Intensity. *R.J. Hansen, ed. Seismic Design for Nuclear Power Plants, MIT Press, Cambridge, Massachusetts*. 438- 483.

Basharkhah, M.A. and Yao, J.T.P. (1984). Reliablity Aspects of Strucutral Control. *Civil Engineering Seystems*. **1**: 244-249

Benjamin, J.R. and Associates (1988). A criterion for determining exceedance of the operating basis earthquake. *Technical report, Electric Power Research Institute, Palo Alto, California*. EPRI Report NP-5930.

Bishop, C. M. (2003). Neural Networks for Pattern Recognition. *Oxford University Press, Oxford, U.K.*

Bogdanoff, J.L., Goldberg, J.E. and Bernard, M.C. (1961). Response of a simple structure to a random earthquake-type disturbance. *Bulletin of the Seismological Society of America*. **51**: 293-310.

Bolotin, V.V. (1960). Statistical theory of the aseismic design of structures. *Proceedings of the 2nd World Conference on Earthquake Engineering, Tokyo and Kyoto, Japan*. **II**: 1365–1374.

Bolt, B. (1969). Duration of strong motion. *Proceedings of the 4th World Conference on Earthquake Engineering*, *Santiago, Chile*. 1304-1315.

Bolt, B. (1976). Nuclear Explosions and Earthquakes: The Parted Veil. *W. H. Freeman and Company.* ISBN-10: 0716702762.

Bommer, J.J. and Acevedo, A.B. (2004). The use of real earthquake accelerograms as input to dynamic analysis. *Journal of Earthquake Engineering*. **8**: 43-91.

Bond, W.E. (1980). A study of the engineering characteristics of the 1971 San Fernando Earthquake records using time-domain techniques. *Ph.D. Thesis, Rensselaer Polytechnical Institute, New York.*

Boore, D.M., Seekins, L. and Joyner, W.B. (1989). Peak acceleration from the 17 October 1989 Loma Prieta earthquake. *Seismological Research Letters*. **60-4**: 151- 166.

Borcherdt, R.D. (1970). Effects of local geology on ground motion near San Francisco Bay*. Bulletin of the Seismological Society of America (BSSA).* **60**: 29–61.

Böse, M., Wenzel, F. and Erdik, M. (2008). PreSEIS: A Neural Network-Based Approach to Earthquake Early Warning for Finite Faults. *Bulletin of the Seismological Society of America (BSSA).* **98**-**1**: 366-382.

Bouckovalas, G. D. and Kouretzis, G. P. (2001). Stiff soil amplification effects in the 7 September 1999 Athens (Greece) earthquake. *Soil Dynamics and Earthquake Engineering*. **21-8**: 671-687.

Bretschneider, J. and Scherer, R. J. (2004). Multi-wave, non-stationary, parametric load model for seismic hazard assessment and prediction. *13th World Conference on Earthquake Engineering (WCEE), Vancouver, B.C., Canada*. Paper No. 2587.

Bretschneider, J. (2006). Ein wellenbasiertes, stochastisches Modell zur Vorhersage der Erdbebenlast., *Ph.D. thesis, Technical University of Dresden, Dep. Civil Eng., Germany*. ISBN: 978-3-86005-557-1.

Bycroft, G.N. (1960). White noise representation of earthquake. *Journal of the Engineering Mechanics Division*. **86**:1-16.

Chang, C. C. and Yang Y., H. T. (1994). Instantaneous optimal control of building frames. *Journal of Structural Engineering.* **120-4**: 1307-1326.

Chang, M.K., Kwiatkwoski, J.W., Nau, R.F., Oliver, R.M. and Pister, K.S. (1982). ARMA models for earthquake ground motions. *Earthquake Engineering and Structural Dynamics*. **10**: 651-662.

Chouet, B., Aki, K. and Tsujiura, M. (1978). Regional variation of the scaling law of earthquake source spectra. *Bulletin of the Seismological Society of America (BSSA)*. **68-1**: 49-79.

Chung, L.L., Reinhorn, A.M. and Soong, T.T. (1988). Experiments on active control of seismic structures. *Journal of engineering mechanics*. **114-2**: 241–56.

Chung, L.L., Lin, C.C. and Lu, K.H. (1995). Time-delay control of structures. *Journal of Earthquake Engineering and Structural Dynamics*. **24**: 687–701.

Clough, R.W. and Penzien, J. (1975). Dynamics of Structures. *Mcgraw-Hill College*. ISBN-13: 978-0070113923.

Coleman, T.F. and Li, Y. (1994). On the Convergence of Reflective Newton Methods for Large-Scale Nonlinear Minimization Subject to Bounds. *Mathematical Programming*. **67-2**: 189-224.

Coleman, T.F. and Li, Y. (1996). An Interior, Trust Region Approach for Nonlinear Minimization Subject to Bounds. *SIAM Journal on Optimization*. **6**: 418-445.

Collins, K. R., Foutch, D. A. and Wen, Y. K. (1995). Investigation of alternative seismic design procedures for standard buildings. *Civil Engineering Studies, Structural Research Series No. 600, University of Illinois, Urbana*. 122-132.

Conte, J.P. and Peng, B.F. (1997). Fully nonstationary analytical earthquake ground-motion model. *Journal of Engineering Mechanics (ASCE)*. **12**: 15–24.

Conte, J.P., Pister, K.S. and Mahin, S.A. (1992). Nonstationary ARMA modeling of seismic motions. *Soil Dynamics and Earthquake Engineering*. **11**: 411-426.

Datta, T.K. (2003). A state-of-the-art review on active control of structures. *ISET Journal of Earthquake Technology*. Paper No. 430, **40-1**: 1-17.

Douglas, J. and Aochi, H. (2008). A survey of techniques for predicting earthquake ground motions for engineering purposes. *Surveys in Geophysics*. **29**: 187-220.

Eshghi, S. and Zaré, M. (2003). Bam (SE Iran) earthquake of 26 December 2003, Mw 6.5: A preliminary reconnaissance report. http://www.iiees.ac.ir/English/bank/eng_databank.html

Finno, G., Hergert, F. and Zimmermann, H.G. (1993). Improving model selection by nonconvergent methods. *Neural Networks*. **6**: 771-783.

Geman, S., Bienenstock, E., and Doursat, R. (1992). Neural networks and the bias/variance dilemma. *Neural Computation*. **4**: 1-58.

Ghaboussi, J. and Lin, C.C.J. (1998). New Method of Generating Spectrum Compatible Accelerograms using Neural Networks. *Earthquake engineering and Structural Dynamices*. **27**: 377-396.

Ghaffarzadeh, H., and Izadi, M. M. (2008). Artificial Generation of Spatially varying Seismic Ground Motion Using ANNs. *14 WCEE, Beijing, China*.

Goldberg, J.E., Bogdanoff, J.L. and Sharpe, D.R. (1964). The response of simple nonlinear structure to a random disturbance of earthquake type. *Bulletin of the Seismological Society of America (BSSA)*. **54**: 263-276.

Haddon, R.A.W. (1996). Use of empirical green's function, spectral ratios, and kinematic source models for simulating strong ground motion. *Bulletin of the Seismological Society of America (BSSA)*. **86-3**: 597-615.

Hammerstrom, L.G., and Gros, K.S. (1980). Adoption of Optimal Control Theory to Systems with Time-Delays. *International Journal of Control*. **32**: 302-357.

Hancock, J., Watson-Lamprey, J.A., Abrahamson, N.A., Bommer, J.J., Markatis, A., McCoy, E. and Mendis, R. (2006). An improved method of matching response spectra of recorded earthquake ground motion using wavelets. *Journal of Earthquake Engineering*. **10**: 67-89.

Hrat, G.C. and Wong, K. (2000). Structural dynamics for structural engineers. *John Wiley & Sons*. ISBN: 0-471-36169-0.

Hoshiya, M., Hasgur, Z. (1978). AR and MA models of nonstationary ground motion. *Bulletin of the International Institute of Seismology and Earthquake Engineering*. **16**: 55-68.

Housner, G.W. (1947). Characteristics of strong-motion earthquakes. *Bulletin of the Seismological Society of America (BSSA)*. **37**: 19-31.

Housner, G. W. (1955). Properties of Strong Ground Motion Earthquakes. *Bulletin of the Seismological Society of America (BSSA)*. **45-3**: 197-218.

Housner, G.W. and Jennings, P.C. (1964). Generation of artificial earthquakes. *Journal of the Engineering Mechanics Division*. **90-1**: 113-150.

Hwang, H., Low, Y. K. and Chang, T. S. (1989). Seismic response study of two Memphis sites. *In Foundation Engineering: Current Principles and Practices, Editor, Fred H. Kullawy, ASCE,* **1**: 786-798.

Idriss, IM (1990). Response of soft soil sites during earthquakes. *Proceedings of the Symposium to Honor Professor H.B. Seed, Berkeley.* 273–89.

Iio, Y. (1995). Observations of the slow initial phase generated by micro earthquakes: implications for earthquake nucleation and propagation. *Journal of Geophysical Research*. **100-B8**: 15333-15349.

Iyengar, R.N. and Iyengar, K.T.S. (1969). A nonstationary random process model for earthquake accelerograms. *Bulletin of the Seismological Society of America (BSSA)*. **59**: 1163-1188.

Jackson, J., Bouchon, M. (2006). Seismotectonic, rupture process, and earthquake-hazard aspects of the 2003 December 26 Bam, Iran, Earthquake. *Geophysical Journal International.* **166**: 1270-1292.

Jennings, P.C., Housner, G.W. and Tsai, N.C. (1968). Simulated earthquake motions. *Earthquake Engineering Research Laboratory, California Institute of Technology, Pasadena, CA.*

Joghataie, A. and Mohebbi, M. (2008). Vibration controller design for confined masonry walls by distributed genetic algorithms. *Journal of Structural Engineering* (*ASCE*). **134-2**: 300-309.

Jurkevics, A. and Ulrych, T.J. (1978). Representing and simulating strong ground motion. *Bulletin of the Seismological Society of America (BSSA)*. **68**: 781-801.

Kameda, H. (1975). Evolutionary spectra of seismogram by multifilter. *Journal of the Engineering Mechanics Division*. **101-6**: 787-801.

Kameda, H. and Sugito, M. (1984). Prediction of Strong Earthquake Motions on Rock Surface Using Evolutionary Process Models. *Proc. Int. Conf Struct. Analysis & Design of Nuclear Power Plants, Porto Alegre.* 161-186.

Kanai, K. (1957). Some empirical formulas for the seismic characteristics of the ground. *Bulletin of the earthquake research institute, university of Tokyo*. **35**: 309-25.

Kanamori, H. (2005). Real-time seismology and earthquake damage mitigation. *Annu. Rev. Earth Planet. Sci.* **33**:195-214.

Katayama, T. (1982). An engineering prediction model of acceleration response spectra and its application to seismic hazard mapping. *Earthquake Eng Struct. Dyn*. **10**: 149-63.

Kaul, M. K. (1978). Spectrum-consistent time-history generation. *Journal of the Engineering Mechanics Division*. **104-4**: 781-788.

Kawakami, H., and Sharma, S. (1999). Statistical study of spatial variation of response spectrum using free field records of dense strong ground motion arrays. *Earthquake Eng. Struct. Dyn.* **28**: 1273-1294.

Kawamura, H., Tani, A., Yamada, M. and Tsunoda, K. (1990). Real Time Prediction of Earthquake Ground Motions and Structural Response by Statistic and Fuzzy Logic. *IEEE.* 534-538.

Kawamura, H., Tani, A., and Yamada, M. (1992). Real Time Prediction of Earthquake Ground Motions and Structural Response by Statistics and Fuzzy Logic, in Ayyub, B. M., Gupta, M. M. and Kanal, L. N. eds.: Analysis and Management of Uncertainty: Theory and Application, 263-275.

Kawamura, H., and Yao, J. T. P. (1990). Application of fuzzy Logic to Structural Control Motion of Civil Engineering Structure, *Proc. Of NAFIPS'90 Quarter Century of Fuzzyness.* **I**: 67-70.

Khan, M. R. (1987). Improved method of generation of artificial time-history, rich in all frequencies, from floor spectra. *Earthquake Engng. Struct. Dyn.* **15**: 985-992.

Kimura, M. and Izumi, M. (1989). A method of artificial generation of earthquake ground motion. *Earthquake Engng. Struct. Dyn.* **18**: 867-874.

Kiureghian A.D. and Crempien, J. (1989). An evolutionary model for earthquake ground motion. *Structural Safety*. **6**: 235-246.

Kozin, F. (1988). Autoregressive moving average models of earthquake records. *Probabilistic Engineering Mechanics*. **3**: 58-63.

Kubo, T. (1987). The importance of phase properties in generation of synthetic earthquake strong motions. *Transactions of the 9th International Conference on Str. Mech. Reactor Tech*. **K1**: 49-64.

Kubo, T., and Penzien, J. (1979). Analysis of Three-dimensional Strong Ground Motions along Principal Axes, San Fernando Earthquake. *Earthquake Engineering and Structural Dynamics*. **7**: 265-278.

Lee, S.C. and Han, S.W. (2002). Neural-network-based models for generating artificial earthquakes and response spectra. *Computers and Structures*. **80**: 1627–1638.

Levy, S. and Wilkinson, J.P. D. (1976). Generation of artificial time histories, rich in all frequencies, from given response spectra. *Nuclear Engng. Des*. **38**: 241-251.

Lin, C. J., and Ghaboussi, J. (2001). Generating Multiple Spectrum Compatible Accelerograms using Stochastic Neural Networks. *Earthquake Engineering and Structural Dynamics*. **30**: 1021-1042.

Lin, C. J. and Ghaboussi, J. (2002). Neural-Network-Based Model for Generating Artificial Earthquake and Response Spectra. *Computers And Structures*. **80**: 1627-1638.

Lin, Y.K. and Yong, Y. (1987). Evolutionary Kanai-Tajimi earthquake models. *J. Eng. Mech., ASCE*. **113-8**: 1119-1137.

Liu, S.C. (1968). Statistical Analysis and Stochastic Simulation of Ground Motion Data. *Bell System Technical Journal*. **47**: 2273-2298.

Liu, S.C. (1970). Synthesis of stochastic representations of ground motions. *The Bell Systems Technical Journal*. **49**:521-541.

Luco, N. and Bazzurro, P. (2007). Does amplitude scaling of ground motion records result in biased nonlinear structural drift responses? *Earthquake Engineering and Structural Dynamics*. **36**: 1813-1835.

Magotra, N., Jiang, J., Hush, D., and Tan, L. (1991). Seismic phase detection and discrimination using adaptive filter coefficients. *In Proceedings of the 25th Asilomar Conference on Signals, Systems and Computers, November*. 659-662.

McGreevy, S., Soong, T.T., and Reinhorn, A.M. (1988). An experimental study of time delay compensation in active structural control. *In: Proc SEM 6th Int Modal Analysis Conf, Orlando, Fla.*, 733–8.

Mei, G., Kareem, A., and Kantor, J. C. (2001). Real-time model predictive control of structures under earthquake, *Earthquake Engineering and Structural Dynamics*, **30**: 995-1019.

Mohanty, W.K., Routray, A., and Nath, S.K. (2007). A new strategy for phase detection in seismic signals using an adaptive Markov amplitude model. *Current Science*, **93-1**: 54.

Naeim, F. and Lew, M. (1995). On the use of design spectrum compatible time histories. *Earthquake Spectra*. **11**: 111-127.

Nakamura, T. et al. (2005). Source fault structure of the 2003 Bam earthquake, southeastern Iran, inferred from the aftershock distribution and its relation to the heavily damaged area: Existence of the Arg-e-Bam fault proposed. *Geophys. Res. Lett.* **32- 9**: 389-398.

National Earthquake Hazards Reduction Program, NEHRP (1997). Recommended provisions for seismic regulations for new buildings. *Federal Emergency Management Agency Report FEMA 302. Washington, DC.* 337.

Okal, E. A., and Synolakis, C. E. (2004). Source discriminants for nearfield tsunamis. *Geophys. J. Int.*, **158**: 899-912.

Oonincx, P. J. (1998). Automatic phase detection in seismic data using the discrete wavelet transform. *CWI-Report*, PNA-9811, ISSN 1386-3711.

Oppenheim, A. V., Schafer, A. W. and Buck, J. R. (1998). Discrete-time signal processing. Prentice Hall, New Jersey.

Palit, A.K., and Popovic, D. (2005). Computational Intelligence in Time Series Forecasting, *Springer*, ISBN-10: 1-85233-948-9.

Penzien J. & Watabe, M. (1975). Characteristics of Three-Dimensional Earthquake Ground Motion. *J. Earthq. Eng. And Struct. Design.* **3**: 365-373.

Pezzo, E.D., Esposito, A., Giudicepietro, F., Marinaro, M., Martini, M., and Scarpetta, S. (2003). Discrimination of Earthquake and Underwater Explorations using Neural Networks. *Bulletin of the Seismological Society of America (BSSA).* **93-1**: 215-223.

Polhemus, N.W. and Cakmak, A.S. (1981). Simulation of earthquake ground motion using autoregressive moving average (ARMA) models. *Earthquake Engineering and Structural Dynamics*. **9-4**: 343-354.

Pousse, G. , Bonilla, L. a. , Cotton, F., and Margerin, L. (2006). Nonstationary Stochastic Simulation of Strong Ground Motion time Histories Including Natural Variability: Application to the K-Net Japanese Database. *Bulletin of the Seismological Society of America (BSSA).* **96**: 2103-2117.

Prechelt, L. (1998). Early Stopping -- but when?. *Neural Networks: Tricks of the trade*, Lecture Notes in Computer Science 1524, Springer, Heidelberg. 55-69.

Priestley, M. B. (1965). Evolutionary spectra and non-stationary stochastic processes. *Journal of the Royal Statistical Society.* **27-2**: 204-237.

Pu, J.P. (1989). Frequency Response Design of Controlled Structure. *Computer Utilization in Structural Engineering ASCE, NY*. 131-141.

Quek, S.T., Teo, Y.P. and Balenda, T. (1990). Non-stationary structural response with evolutionary spectra using seismological input. *Earthquake engineering and structural dynamics*. **19**: 275-288.

Radeva, S., Radev, D. and Yakov, V. (2004b). Vector quantization algorithms for one-dimensional and two-dimensional time series. *In: Proceedings of the CompSysyTech'2004. Rousse. IIIA.17- 1–IIIA.17-6.*

Radeva, S., Scherer, R.J. and Radev, D. (2004a). Strong motion waves classification and prognoses with neural networks. *In: Proceedings of the 13th World Conference on Earthquake Engineering, Vancouver, Canada*. paper No.: **2780**.

Radeva, S.T., Scherer, R.J. and Radev, D. (2005). Strong motion waves estimation for seismic control of nuclear power plant. *Nuclear Engineering and Design*. **235**: 1977-1988.

Radeva, S., Scherer R. J., Radev, D., Yakov, V.(2004). Real-time estimation of strong motion seismic waves, *Acta Geodaetica et Geophysica Hungarica,* **39, 2-3**:297-308.

Rezaeian, S., and Kiureghian, A. D. (2008). A stochastic ground motion model with separable temporal and spectral nonstationarities. *Earthquake Engineering and Structural Dynamics.* **37**: 1565-1584.

Rezaeian, S. and Kiureghian, A.D. (2010). Simulation of synthetic ground motions for specified earthquake and site characteristics. *Earthquake Engineering and Structural Dynamics*. **39**: 1155-1180.

Rodellar, J., Barbat, A. H. and Matin-Sanchez, J. M. (1987). Predictive control of structures. *Jouran of Engineering Mechanics Division ASCE.* **113**, 6:797–812.

Rofooei, F.R., Aghababaii Mobarake, A. and Ahmadi, G. (2001). Generation of artificial earthquake records with a nonstationary Kanai–Tajimi model. *Engineering Structures*. **23**: 827-837.

Rosenblueth, E. and Bustamante, J. (1962). Duration of structural response to earthquakes. *Journal of the Engineering Mechanics Division*. **88**: 75-106.

Sabetta, F. and Pugliese, A. (1996). Estimation of response spectra and simulation of nonstationary earthquake ground motions. *Bulletin of the Seismological Society of America (BSSA)*. **86-2**: 337-352.

Sadeghi, H., Fatemi Aghda, S.M., Suzuki, S & Nakamura, T. (2006). 3-D velocity structure of the 2003 Bam earthquake area (SE Iran): Existence of a low-Poisson's ratio layer and its relation to heavy damage. *Tectonophysics.* **417, 3-4**: 269-283.

Safak, E. (1997). Models and methods to characterize site amplification from a pair of records. *Earthquake Spectra.* **13**: 97–129.

Samaras, E., Shinozuka, M. and Tsurui, A. (1985). ARMA representation of random processes. *Journal of the Engineering Mechanics Division.* **111-3**: 449-461.

Saragoni, G.R. and Hart, G.C. (1974). Simulation of artificial earthquakes, Earthquake. *Eng. Struct. Dyn*. **2**, **3**: 249-267.

Sato, T., and Kanamori, H. (1999). Beginning of earthquakes modeled with the Griffith's fracture criterion. *Bulletin of the Seismological Society of America (BSSA)*. **89**: 80-93

Scherer, R.J. (1993). Advancement in Strong Motion Analysis by the Use of Evolutionary Power Spectra. *Tectonophysics*. **218, 1-3**: 83 – 91.

Scherer, R.J., and Bretschneider, J. (2000). Stochastic Identification of Earthquake wave entities. *Proceedings of the 12th WCEE*. **Paper No:** 2436/4/A.

Scherer, R.J., Riera, J.D. and Schueller, G.I. (1982). Estimation of the time-dependent frequency content of earthquake accelerations. *J. Nucl. Eng. Design.* **71**: 301-310.

Scherer, R.J., Schuëller, G.I. (1988). Quantification of Local Site and Regional Effects on the Nonstationarity of Earthquake Accelerations. *9th World Conference on Earthquake Engineering, Tokyo - Kyoto, Japan.*

Scherer, R. J., Zahedi Khameneh, A. and Bretschneider, J. (2008). Non-stationary analysis of BAM 2003 earthquake record. *The 14th World Conference on Earthquake Engineering October 12-17, Beijing, China.*

Scrivner, C.W. and Helmberger, D.V. (1995). Preliminary Work on an Early Warning and Rapid Response Program for Moderate Earthquakes. *Bulletin of the Seismological Society of America (BSSA).* **85**: 1257-1265.

Seed, H. B., Romo, M. P., Sun, J., Jaime A. and Lymser, J. (1987). Relationships between soil conditions and earthquake ground motions in Mexico City in the earthquake of September 19, 1985. *Report No. UBD/EERC–87/15, Earthquake Engineering Research Center, University of California, Berkeley, California.* October 1987.

Shama, A. (2007). Simplified procedure for simulating spatially correlated earthquake ground motions. *Engineering Structures*. **29**: 248-258.

Shinozuka, M. and Deodatis, G. (1988). Stochastic process models for earthquake ground motion. *Probabilistic Engineering Mechanics*. **3**:114-123.

Shinozuka, M. and Sato, Y. (1967). Simulation of non-stationary random process. *Journal of Engineering Mechanics (ASCE)*. **93**:11-40.

Soliman, M.A., and Roy, W.H. (1992). Optimal Feedback Control for Linear Quadratic System Having Time-Delay. *International Journal of Control*, **15**: 609-615.

Soong, T. T. (1990). *Active structural control: theory and practice. Longman Scientific & Technical.* ISBN 0-582-01782-3.

Stafford, P.J., Sgobba, S. and Marano, G.C. (2009). An energy-based envelope function for the stochastic simulation of earthquake accelerograms. *Soil Dynamics and Earthquake Engineering*. **29**: 1123-1133.

Tajimi, H. (1960). A statistical method of determining the maximum response of a building structure during an earthquake. *Proceeding of the second world conference on earthquake engineering. Tokyo and Kyoto*. **II**:781-797.

Talebian, M. & Jackson, J.A. (2002). Offset on the main recent fault of NW Iran and implications for the late Cenozoic tectonics of the Arabia–Eurasia collision zone. *Geophys. J. Int.* **150**: 422-439.

Talebian, M. (2004). The 2003 Bam (Iran) earthquake: rupture of a blind strike-slip fault. *Geophys. Res. Lett.* **31**, L11611.

Thomson, W. T. (1959). Spectral aspect of earthquakes. *Bulletin of the Seismological Society of America (BSSA).* **49**: 91-98.

Thrainsson, H. and Kiremidjian, A. S. (2002). Simulation of digital earthquake accelerograms using the inverse discrete Fourier transform. *Earthquake Engineering and Structural Dynamics.* **31**: 2023-2048.

Trifunac, M.D. and Brady, A.G. (1975). A study on the duration of strong earthquake ground motion. *Bulletin of the Seismological Society of America (BSSA).* **65**: 581-626.

Umeda, Y. (1990). High-amplitude seismic waves radiated from the bright spot of an earthquake. *Tectonophysics.* **141**: 335-43.

Walker, R., Jackson, J.A. (2002). Offset and evolution of the Gowk fault, S.E. Iran: a major intra-continental strike-slip system. *J.Struct. Geol.* **24**: 1677-1698.

Wang, J., and Teng, T.-L. (1995). Artificial neural network-based seismic detector. *Bulletin of the Seismological Society of America (BSSA).* **85-1**: 308-319.

Wang, J., and Teng, T.-L. (1997). Identification and Picking of s Phase Using an Artificial Neural Network. *Bulletin of the Seismological Society of America (BSSA).* **87-5**: 1140-1149.

Wasserman, P. D. (1993). Advanced methods in neural computing (First edition). *John Wiley & Sons, Inc. New York, NY, USA*, ISBN: 0442004613.

Watson-Lamprey, J.A. (2007). Selection and scaling of ground motion time series. *Ph.D. Thesis (in Engineering—Civil and Environmental Engineering), University of California, Berkeley, CA.*

Wong, H. L. and Trifunac, M. D. (1979). Generation of artificial strong motion accelerograms. *Earthquake Engng. Struct. Dyn.* **7**: 509-527.

Yang, J.N., Akbarpour, A., and Askar G. (1990). Effect of time delay on control of seismic-excited buildings. *Journal of Structural Engineering.* **116**: 2801–14.

Yeh, C.-H., and Wen, Y. K. (1990). Modeling of nonstationary ground motion and analysis of inelastic structural response. *Structural Safety.* **8**, **1–4**: 281–298.

Zahedi Khameneh, A. and Scherer, R. J. (2008). Generating the Strong Ground Motion Based on the First Oncoming Signals Using Artificial Neural Networks. *5th European Congress on Computational Methods in Applied Sciences and Engineering, June 30-July 4, Venice, Italy.*

Zaré, M. & Hamzehloo, H. (2005). Strong Ground-Motion Measurements during the 2003 Bam, Iran, Earthquake. *Earthquake Spectra.* **21**: 165-179.

Zerva, A. (1988). Seismic source mechanisms and ground motion models. *Probabilistic Engineering Mechanics*. **3**: 64-74.

Zerva, A., and Zervas, V. (2002). Spatial variation of seismic ground motions: An overview. *Appl. Mech. Rev*. **55-3**: 271-297.

Zhao, Y., and Takano, K. (1999). An Artificial Neural Network approach for Broadband Seismic Phase Picking. *Bulletin of the Seismological Society of America (BSSA)*. **89-3**: 670-680.

Bisher erschienene Dissertationen, Habilitationen und Hefte des Instituts für Bauinformatik[1]

Christoph Meinecke	Ein objektorientiertes Konstruktions-expertensystem mit Regelmethoden	Selbstverlag Karlsruhe, 07/1995
Markus Hauser	Eine kognitive Architektur für die wissensbasierte Unterstützung der frühen Phasen des Entwurfs von Tragwerken	logos Verlag Berlin, 06/1998
Martin Zsohar	Stochastische Größen der Resonanzfrequenzen und der Verstärkung seismischer Wellen im horizontal geschichteten zufälligen Medium	Shaker Verlag Aachen, 07/1998
Christian Steurer	Modellierung und Berechnung des Ermüdungsrißfortschritts mit stochastischen Differential-gleichungen	Selbstverlag, 02/1999
Peter Katranuschkov	A Mapping Language for Concurrent Engineering Processes	Heft 1, 02/2001
Karsten Menzel	Methodik zur nachhaltigen, rechnergestützten Ressourcenverwaltung im Bauwesen	Heft 2, 11/2003
Michael Eisfeld	Assistance in Conceptual Design of Concrete Structures by a Description Logic Planner	Heft 3, 11/2004
Matthias Weise	Ein Ansatz zur Abbildung von Änderungen in der modellbasierten Objektplanung	Heft 4, 11/2006
Jörg Bretschneider	Ein wellenbasiertes stochastisches Modell zur Vorhersage der Erdbebenlast	Heft 5, 12/2006
Martin Keller	Informationstechnisch unterstützte Kooperation bei Bauprojekten	Heft 6, 06/2007
Kamil Umut Gökce	IT Supported Construction Management	Heft 7, 06/2008
Gerald Faschingbauer	Simulationsbasierte Systemidentifikation im Rahmen der baubegleitenden geotechnischen Überwachung	Heft 8, 01/2011
Wael Sharmak	Dynamic Network Planning in Construction Projects using Configurable Reference Process Models	Heft 9, 05/2011

[1] Bis September 2003 Lehrstuhl für Computeranwendung im Bauwesen